Solid-state lasers with tunable output properties enabled by MEMS mirrors

Alan Paterson

Department of Electronic and Electrical Engineering

Centre for Microsystems & Photonics

A thesis submitted to the Department of Electronic and Electrical Engineering at the University of Strathclyde for the degree of Doctor of Philosophy

September 2019

Declaration of Authenticity & Author’s rights

This thesis is the result of the author’s original research. It has been composed by the author and has not been previously submitted for examination which has led to the award of a degree.

The copyright of this thesis belongs to the author under the terms of the United Kingdom Copyright Acts as qualified by University of Strathclyde Regulation 3.50. Due acknowledgement must always be made of the use of any material contained in, or derived from, this thesis.

Signed:

Date: 13/09/2019

Acknowledgements

I want to thank a number of people / parties for their contributions towards the work described in this thesis. First and foremost are Dr. Walter Lubeigt and Prof. Deepak Uttamchandani who instigated this project and gave me the opportunity to complete this PhD. Their continued efforts and support throughout the project were invaluable. I also want to thank the EPSRC for funding the project and the University of Strathclyde, where I spent over 8 years as an engineering student. This was a thoroughly enjoyable experience and I am grateful for the opportunities I have been provided with. A special thanks goes to Dr. Ralf Bauer, who provided knowledge and support for my work, even during my write-up phase when I moved to the Netherlands. He was an inspiration for me to complete this work and I am very grateful for his contribution. Thanks also goes to Helia Photonics and John Mackersie (Strathclyde) who implemented optical coatings for my MEMS devices, without which much of this work could not have been completed.

As well as those directly involved in my project, I want to thank the CMP as a whole for providing an enjoyable and interactive place of work. The staff always had an open door to offer their advice & knowledge when called upon, and the students were always up for a blether. The work ethic at the CMP is second-to-none and I will cherish my time there for years to come. Besides the serious stuff, lunch was always entertaining with some wild stories. Those lunchtime stories will be missed, as will Steak Pie Wednesday at Madison's. Thanks again to everyone and best of luck in your future endeavors.

A final thank you goes to my friends, family and colleagues at Sencio B.V. who always believed in me and showed interest in my work. Sencio supported me by allowing me to write-up at the office during & after work hours, which was a massive help in completing this thesis. This is something that not many companies would do, and I am grateful for that.

Abstract

The use of micro-electro-mechanical systems (MEMS) as intracavity elements in lasers has grown in interest in recent decades. A variety of MEMS mirrors have recently been shown to provide miniaturized alternatives to conventional Q-switch devices. They have the potential to reduce system cost through batch fabrication and reduce the electrical power demand of such systems. The aim of this thesis was to investigate the novel use of MEMS mirrors within solid-state lasers as intracavity tuning elements.

The MEMS mirrors used for this work were fabricated using a commercial multi-user process that has been used and characterized extensively by the Centre for Microsystems and Photonics. Two MEMS mirror designs were investigated: one with four electrothermal (ET) actuators and one with an electrostatic (ES) comb-drive actuator. Both mirrors could be driven at their mechanical resonance to result in resonant scanning, while the ET mirror could also be tilted to a fixed angle. The ES mirror movement occurred on one axis while the tilt angle of the ET mirror could be controlled on two axes due to the radial positioning of the four ET actuators. Both mirrors were optically coated after fabrication to enhance their reflectance in the near infrared.

The fabricated MEMS mirrors were investigated as intracavity tuning elements for three solid-state laser concepts. The first was a Q-switched Nd: YAG laser with tunable temporal characteristics enabled by separate actuation of two MEMS mirrors. The second was an Yb: KGW laser with tunable output wavelength enabled by a prism and an ET mirror in the Littman configuration. The third was a Q-switched Yb: KGW laser with tunable output wavelength and pulse duration enabled by dual-axis actuation of a single ET mirror combined with a prism in the Littman configuration.

To my knowledge, the above-mentioned investigations are the first of their kind and show clear potential for the advancement of MEMS in solid-state laser technology. Such lasers could be appealing for biomedical and automotive applications such as photoacoustic imaging and lidar. Development of a reliable method to deposit a high-reflectance coating on the surface of the MEMS mirrors would also enable power-scaling of the laser output, making the concepts compatible with defence and manufacturing applications such as range finding and laser processing.

Publications

Journal publications

R. Bauer, A. Paterson, C. Clark, D. Uttamchandani & W. Lubeigt, “Output Characteristics of Q-switched Solid-State Lasers Using Intracavity MEMS Micromirrors”, IEEE Journal of Selected Topics in Quantum Electronics, Vol. 21 (1), pp. 356-363, January 2015.

A. Paterson, R. Bauer, L. Li, W. Lubeigt & D. Uttamchandani, “Range extension of a bimorph varifocal micromirror through actuation by a Peltier element”, IEEE Journal of Selected Topics in Quantum Electronics, Vol. 21 (4), pp. 72-78, July 2015.

A. Paterson, R. Bauer, W. Lubeigt & D. Uttamchandani, “Tunable Yb:KGW laser, CW or Q-switched, enabled by dual-axis tilt of a MOEMS mirror”, IEEE Journal of Selected Topics in Quantum Electronics, Vol. 24 (5), pp. 1-9, September 2018.

Conference publications

A. Paterson, L. Li, R. Bauer, W. Lubeigt & D. Uttamchandani, “Comparison of modelled and experimental behaviour of a thermoelectrically actuated varifocal micromirror”, 2014 International conference on Optical MEMS and Nanophotonics (OMN), Glasgow, UK, 2014, pp. 157-158.

A. Paterson, R. Bauer, C. Clark, D. Uttamchandani & W. Lubeigt, “Intracavity control of solid-state lasers using MEMS micromirrors”, 2014 International conference on Optical MEMS and Nanophotonics (OMN), Glasgow, UK, 2014, pp. 219-220.

A. Paterson, R. Bauer, C. Clark, D. Uttamchandani & W. Lubeigt, “MEMS-controlled solid-state lasers”, Advanced Solid-State Lasers, OSA technical digest (online), 2014.

A. Paterson, R. Bauer, R. Li, W. Lubeigt & D. Uttamchandani, “Wavelength tuning of a solid-state laser with a tilting MEMS micromirror”, 2016 International conference on Optical MEMS and Nanophotonics (OMN), Singapore, 2016, pp. 1-2.

A. Paterson, R. Bauer, R. Li, C. Clark, W. Lubeigt & D. Uttamchandani, “Spectral and temporal control of Q-switched solid-state lasers using intracavity MEMS”, SPIE Photonics West, Solid-state laser XXV: technology and devices, San Francisco, USA, March 2016.

A. Paterson, R. Bauer, W. Lubeigt & D. Uttamchandani, “Q-switched tunable solid-state laser using a MOEMS mirror”, 2017 International Conference on Optical MEMS and Nanophotonics (OMN), Santa Fe, USA, 2017, pp. 1-2.

Acronym definitions

The acronyms listed below are those used continuously throughout this thesis. Localized acronyms are not included.

AR:	Anti-reflectance
CCD camera:	Charge-coupled device camera
CMP:	Centre for Microsystems and Photonics (at the University of Strathclyde)
CTE:	Coefficient of thermal expansion
CW:	Continuous wave
DC:	Direct current
ES:	Electrostatic
ES mirror:	Electrostatically actuated mirror
ET:	Electrothermal
ET mirror:	Electrothermally actuated mirror
FEM:	Finite element model
FWHM:	Full-width half maximum
HeNe laser:	Helium-neon laser
HR:	High reflectance
MEMS:	Micro-electro-mechanical systems
Nd: YAG:	Neodymium-doped yttrium aluminium garnet (Nd: $Y_3Al_5O_{12}$)
OSA:	Optical spectrum analyser
PCB:	Printed circuit board
ROC:	Radius of curvature
SCS:	Single crystal silicon
SOIMUMP's:	Silicon-on-insulator multi-user MEMS process
TEM:	Transverse electromagnetic mode
TOSA:	Total optical scan angle
VCSEL:	Vertical-cavity surface-emitting laser
Yb: KGW:	Ytterbium-doped potassium gadolinium tungstate (Yb^{3+}: $KGd(WO_4)_2$)

Table of Contents

1. Introduction

Micro-electro-mechanical Systems, also known as Microsystems Technology or MEMS, have been developed for sensing and actuating in a myriad of diverse application areas, contributing to over 30 % of the total sensor and actuator market as of 2016 [1]. The compatibility of silicon MEMS with the manufacturing of silicon integrated circuits has provided an ideal platform for the miniaturisation of modern technology. The use of optical MEMS in the form of mirrors for light manipulation was first demonstrated by IBM in 1980, where a torsional scanning mirror was fabricated using batch photolithography and thin film techniques [2]. Alongside miniaturisation and the capability of volume manufacturing, the MEMS mirror (micromirror) exhibited comparable performance characteristics and reduced electrical demand in comparison to commercial bulk scanners that were available at the time. The potential was therefore obvious to improve existing technology, investigate application areas with stringent spatial limitations and even generate novel concepts.

The research of optical MEMS has since grown exponentially, expanding to create new technology areas such as digital micromirror devices [3], diffractive MEMS [4] and optofluidic devices [5]. Optical MEMS have been researched and commercialised in applications such as biomedical imaging and sensing [6, 7], spectroscopy [8, 9], laser projection systems [10, 11], telecommunications [12] and automotive sensing [7, 11]. MEMS mirrors themselves have also received a lot of research attention due to their capabilities of rapid scanning, large angular deflection and deformable surfaces with little energy demand.

In recent decades, MEMS mirrors have been investigated as functional elements within lasers as opposed to being external light modulators. The lasers themselves could therefore exploit the inherent benefits of using MEMS technology to replace bulk optical components. So-called ‘MEMS lasers’ which have been successful are vertical-cavity surface-emitting lasers (VCSEL’s) with tunable output wavelength enabled by integrated MEMS technology. Batch fabrication and their ease of integration with optical fibre systems provide a favourable mechanism for wavelength division multiplexing in optical communication systems [12]. A variety of tunable MEMS lasers have also been reported in the form of external-cavity semiconductor lasers [13]. In fibre lasers, membrane and cantilever type

MEMS mirrors have been used to enable a pulsed laser output in the form of Q-switching [14, 15] and mode-locking [16]. These techniques are discussed further in the coming sections.

Research at the Centre for Microsystems & Photonics (CMP) has previously focused on solid-state lasers with MEMS mirrors as active Q-switches [17, 18] and adaptive optics [19]. The term 'solid-state laser' defines a bulk laser using a solid-state gain medium, usually a glass or crystal slab doped with rare earth ions or transition metal ions. The term can also be loosely applied to fibre lasers and semiconductor lasers, however in the context of this thesis these will be defined separately to avoid ambiguity. The motivation behind this thesis is to further investigate the use of MEMS in solid-state lasers as active tuning elements, with a view towards novel concepts and multi-functionality enabled by MEMS technology.

The remainder of this chapter will introduce the theory behind solid-state lasers, the fabrication & operation of MEMS mirrors and the state-of-the-art regarding MEMS lasers. Chapter 2 introduces and characterizes the MEMS mirrors used for this thesis. The solid-state lasers utilizing these MEMS mirrors as tuning elements are then introduced and characterized in the following three chapters. The first laser concept expands on the MEMS Q-switched Nd: YAG laser reported in [18] to include tunable temporal output characteristics enabled by separate actuation of two intracavity MEMS mirrors. The second concept investigates wavelength tuning of an Yb: KGW laser enabled by the combination of a prism and a MEMS mirror in the Littman configuration. Finally, the third concept demonstrates a Q-switched Yb: KGW laser with independently tunable output wavelength and pulse duration enabled by dual-axis tilt control of a single MEMS mirror combined with a prism in the Littman configuration. The thesis is then rounded off with a conclusion and suggested future work to advance the research reported in this thesis.

To the best of my knowledge, the concepts in the above-described thesis outline are the first of their kind to be reported and show the potential that MEMS offer towards solid-state laser technology. Laser wavelength tuning using MEMS is prevalent in the form of MEMS VCSEL's and external-cavity diode lasers but has never been demonstrated in intracavity solid-state lasers. Furthermore, the use of multiple intracavity MEMS mirrors and even the use of a single intracavity MEMS mirror to tune several properties of the output beam from a solid-state laser paves the way towards a miniaturised, multi-functional solid-sate laser.

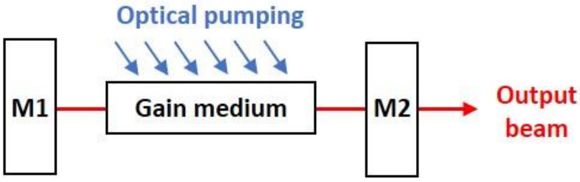

Figure 1-1: Diagram showing the fundamental components of a solid-state laser: the gain medium, optical pumping and a resonator constructed using mirrors. Mirror M1 is HR and mirror M2 is partially transmissive to facilitate an output beam.

1.1. Solid-state laser theory

The fundamental operation of a solid-state laser is reliant on a gain medium, optical pumping and a resonator. A diagram of the conventional two-mirror laser is shown in Figure 1-1, where mirror M1 is high-reflectance (HR) and mirror M2 (the output coupler) is partially transmissive to facilitate a laser output beam. An overview of the fundamental theory behind the three above-mentioned laser components is given in this subsection. In-depth analyses of laser theory and concepts can be found in literature, e.g. [20, 21].

1.1.1. The gain medium

The purpose of the gain medium is to provide a robust platform upon which laser operation can occur. To achieve this, the medium must yield: (a) favourable optical properties such as transparency and homogeneous refractive index, (b) favourable mechanical and thermal properties such as hardness and thermal conductivity, and (c) favourable intrinsic properties to enable the efficient absorption & emission of radiation. Solid-state materials that exhibit these properties are typically glasses or crystals doped with either transition metal or rare-earth metal ions.

Absorption and emission are the core mechanisms by which lasers operate and can be analysed using the energy level structure of the gain medium. Most laser gain media can be estimated using a three-level, four-level or quasi-three-level structure (see Figure 1-2). Among each of these structures are a ground level, an absorption (pump) band and a fluorescent (laser) line. At thermal equilibrium, the proportion of ions existing in each energy level is defined by the Boltzmann distribution. The ions can transition between these energy levels through fast transitions, absorption, spontaneous emission and stimulated

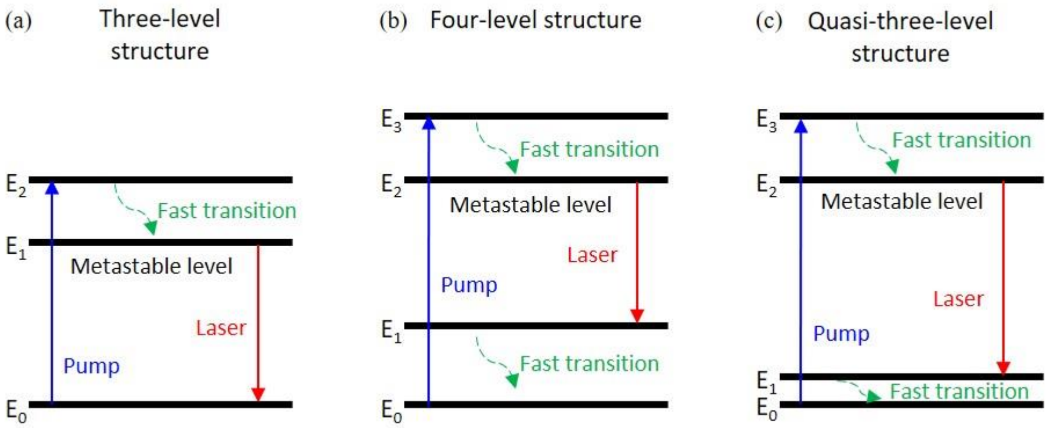

Figure 1-2: Diagrams of the energy level structures of common laser gain media: (a) the three-level structure, (b) the four-level structure, and (c) the quasi-three-level structure.

emission. The energy E required for an ion to transition between states is defined by Equation 1-1, where h is Planck's constant, λ is wavelength and c is the speed of light.

$$\mathrm{E} = \frac{\mathrm{hc}}{\lambda} \qquad \text{(Equation 1-1)}$$

A condition that is required for lasing to occur is that the population of ions existing in the upper laser level exceeds that of the lower laser level, known as population inversion. To achieve this, the Boltzmann distribution must be overcome by injecting photons at the wavelength of the absorption band. Photon injection is known as optical pumping and is described later in Section 1.1.2. The ions existing in elevated states can transition back to the ground state through the emission of a photon or fast transitions where energy is transmitted to the lattice structure. The emission of a photon can be spontaneous or stimulated. Spontaneous emission is bound by the state lifetime and results in the emission of a photon with random phase and direction. Stimulated emission is induced by impinging photons and results in the emission of a photon with identical properties to that of the impinging photon. Stimulated emission is therefore the only emission mechanism which can result in optical amplification and a coherent beam of light. To sustain a population inversion, the upper (metastable) laser level must yield a long enough lifetime for stimulated emission to become the dominant transition over spontaneous emission.

An example of a three-level laser is the ruby laser (Cr^{3+}: Al_2O_3). Ruby has strong absorption bands at $\lambda = 400$ nm and $\lambda = 550$ nm and fluorescent lines at $\lambda = 594$ nm and $\lambda = 693$ nm. When optically pumped at the wavelength of the absorption band, a proportion of the ions is induced to transition from state E_0 to E_2 (Figure 1-2a). The ions then transition quickly from state E_2 to the metastable level E_1 with the lost energy transferred to the lattice structure. The laser line then exists between levels E_1 and E_0. A notable factor in the performance of a three-level laser is that the lower laser level is the heavily populated ground level E_0. A strong pumping intensity is therefore required to achieve a population inversion and reabsorption can occur efficiently at the laser wavelength.

In four-level lasers such as Nd: YAG, the laser line exists between the two elevated states E_2 and E_1 (Figure 1-2b). The lower laser line is therefore higher than the ground state and has a lower ion population in thermal equilibrium. The optical pumping required to achieve population inversion is therefore less than the case of three-level lasers and results in more efficient laser operation. The absorption band exists between levels E_0 and E_3 and fast transitions occur between levels E_3 and E_2 & levels E_1 and E_0. Nd: YAG is the most commonly used laser gain medium to date with a strong absorption band at $\lambda = 808$ nm and a laser wavelength of $\lambda = 1064$ nm. Nd: YAG lasers are commonly frequency doubled or trebled to produce an output beam in the visible spectrum. Other laser wavelengths can also be stimulated at $\lambda = 946$ nm, 1123 nm, 1319 nm, 1338 nm, 1415 nm and 1444 nm, but with lower emission cross-sections. In the case of $\lambda = 946$ nm, the laser operates as a quasi-three level system.

Quasi-three-level lasers yield an intermediate characteristic between the three-level and four-level lasers. The structure is similar to the four-level laser, but the lower laser level is so close to the ground level that a significant proportion of ions exist within it in thermal equilibrium, resulting in reabsorption and a larger pump intensity to achieve population inversion. A prominent quasi-three-level laser is the Yb: YAG laser which has an absorption band at $\lambda = 941$ nm and a laser line at around $\lambda = 1030$ nm. Advantages of Yb: YAG are the small quantum defect and the large spectral width of the absorption band. These result in less thermal constraints on the crystal and the pump source, enabling high laser output power with good beam quality.

Solid-state lasers have been created based on a vast number of gain media with absorption and emission characteristics varying across the optical spectrum. Examples of other Nd: doped crystals include YLF (yttrium-lithium-fluoride), YVO_4 (yttrium-vanadate) and glass, all emitting at a wavelength around 1 µm. Competition in the same spectral region is brought by Yb: doped gain media such as Yb: YAG, Yb: KGW (potassium-gadolinium-tungstate) and Yb: KYW (potassium-yttrium-tungstate). Yb lasers typically have a broader gain bandwidth than Nd lasers (up to 50 nm), which can be exploited to achieve tunable laser wavelength and ultrashort pulses (mode-locking). Another prominent gain medium used for tunable lasers and ultrashort pulses, particularly in biomedical applications, is the titanium-sapphire laser (Ti: Al_2O_3) which has a gain bandwidth spanning 650 nm to 1180 nm.

Erbium (Er) and thulium (Tm) doped lasers can emit at longer wavelengths in the 1.5 µm and 2 µm regions respectively and are commonly used in fibre lasers. Emission at these wavelengths is deemed somewhat eye-safe since the light is absorbed mostly within the cornea and avoids the sensitive retina. Emitting at wavelengths longer than 3 µm can result in significant damage to the cornea because of the short absorption length. This must be considered in some chromium (Cr) doped lasers, such as Cr: ZnSe (zinc selenide) which has a gain bandwidth ranging from 1.9 µm to 3.5 µm. The extremely large gain bandwidth of Cr doped lasers is of interest in optical sensing because it overlaps the rotational and vibrational states of many different gas molecules.

1.1.2. Optical pumping

The second component required to achieve laser operation is optical pumping, i.e. injecting the gain medium with photons at the wavelength of the absorption band to induce population inversion. Optical pumping can be done using two methods: end-pumping which occurs on the same longitudinal axis as the laser beam, or side-pumping which happens perpendicularly to the axis of the laser beam. The pump source must have a sufficiently narrow linewidth at the absorption band to maintain laser efficiency. Common pump sources for solid-state lasers include flash lamps, arc lamps and laser diodes.

When end-pumping, the pump light is shaped and focused within the gain medium to closely match the spatial properties of the laser beam. The conversion efficiency can therefore be high because the pump light is confined to the region in which the laser beam will oscillate. End-pumping of solid-state lasers is commonly performed using laser diodes. Limitations on end-pumping are imposed by (a) only being able to pump from two sides at most, and (b) the beam quality of the pump source. In comparison to solid-state lasers, the beam emitted from laser diodes is often multi-modal and highly divergent, especially at high intensity. This leads to a variation in the intensity distribution over the length of the gain medium and affects the beam quality of the solid-state laser.

Side-pumping is performed perpendicularly to the laser beam across the length of the gain medium, meaning injection can occur from multiple directions. This can significantly reduce the spatial footprint & complexity of the laser and allow simpler alignment of the laser components. The conversion efficiency of side-pumped lasers is usually less than that of end-pumped lasers because the pump light is incident on the entire crystal and not confined to the region in which the laser beam will oscillate. This does however lead to a more homogeneous intensity distribution over the length of the gain medium. Flash lamps, arc lamps and radially positioned diode bars are commonly used for side-pumping of solid-state lasers.

1.1.3. The resonator

The final solid-state laser component to be discussed is the optical resonator. The simplest form of resonator consists of a mirror on either side of the optically pumped gain medium, as was shown in Figure 1-1. An oscillating electromagnetic wave is then formed as the emitted radiation is reflected back and forth between the mirrors, one of which is partially transmissive to facilitate an output beam. Optical feedback is provided as the radiation is amplified during each roundtrip through the pumped gain medium. To sustain lasing, the resulting amplification must be coherent and in-phase, meaning the oscillating wave front must replicate itself over multiple roundtrips of the resonator to form a standing wave. The number of longitudinal modes which can oscillate depends on the optical length of the resonator, which must be an integer multiple of the mode wavelength.

If a standing wave is formed and the net optical gain replenishes the net losses of the laser system, the laser threshold condition will be met, and a sustainable laser beam can be realised. The threshold condition for lasing is partly dependent on the reflectance of the mirrors. The condition is given in Equation 1-2, where R_1 and R_2 are the reflectance of the mirrors, l is the length of the gain medium, G_0 is the gain coefficient of the medium per unit length and α is the absorption coefficient.

$$R_1 R_2 e^{(\mathrm{G}_0-\alpha)2l} = 1 \qquad \text{(Equation 1-2)}$$

The resonator design is highly adaptable and is dependent on the laser being constructed. To simplify the design of resonators for solid-state lasers, it is common to neglect longitudinal modes and assume a Gaussian transverse mode profile (TEM_{00}). Gaussian beams have a spherical wave front with a radius of curvature (ROC) that varies with distance z from the beam waist radius, ω_0. This is defined by Equation 1-3 [20]. A mirror positioned at distance z from the beam waist with a ROC equal to the wave front will reflect the beam without modifying the shape of the wave front. If both resonator mirrors satisfy this condition, a stable resonator is formed.

Table 1-1: ABCD matrix definitions for common optical interactions.

Optical interaction	ABCD matrix	Description
Propagation within a medium	$\begin{bmatrix}1 & d\\ 0 & 1\end{bmatrix}$	Distance, *d* Constant refractive index
Refraction at a flat surface	$\begin{bmatrix}1 & 0\\ 0 & {n_1}/{n_2}\end{bmatrix}$	Refractive index before, n_1 Refractive index after, n_2
Thin lens	$\begin{bmatrix}1 & 0\\ -{1}/{f} & 1\end{bmatrix}$	Focal length, *f* *f* >> lens thickness
Reflection at a flat surface	$\begin{bmatrix}1 & 0\\ 0 & 1\end{bmatrix}$	Surface perpendicular to beam
Reflection at a curved surface	$\begin{bmatrix}1 & 0\\ -{2}/{R_e} & 1\end{bmatrix}$	R_e = ROC cos(θ) on horizontal plane R_e = ROC / cos(θ) on vertical plane θ = angle of incidence on horizontal plane

$$ROC(z) = z\left[1 + \left(\frac{\pi\,\omega_0^2}{\lambda\, z}\right)^2\right] \qquad \text{(Equation 1-3)}$$

To analyse more complex resonators, the ABCD-matrix method can be used to calculate the spatial characteristics of a Gaussian beam as it interacts with each resonator element [22]. The beam radius *r’* and the beam divergence angle *θ’* after an optical interaction can be calculated using Equation 1-4, where *r* and *θ* are the beam radius and divergence angle at the input respectively.

$$\begin{bmatrix}r'\\ \theta'\end{bmatrix} = \begin{bmatrix}A & B\\ C & D\end{bmatrix} \cdot \begin{bmatrix}r\\ \theta\end{bmatrix} \qquad \text{(Equation 1-4)}$$

$$-1 < \frac{A+D}{2} < 1 \qquad \text{(Equation 1-5)}$$

The terms *A*, *B*, *C* and *D* quantify the optical interaction. A list of ABCD matrix definitions for common optical interactions is given in Table 1-1. The matrices can be applied collectively to simulate an entire resonator through matrix multiplication in the reverse order in which the optical interactions occur. The condition for a stable resonator is that the resulting ABCD matrix solution satisfies the condition in Equation 1-5 [22]. The ABCD matrix method is a useful tool that can be used to design complex resonators. The method is implemented in several software packages to accelerate the design process.

The ABCD simulator tool WinLase was used to design the resonators investigated in this thesis. Inputs to the tool include the laser wavelength, the resonator components, the distance between each component and the properties of each component (refractive index, angle of incidence, focal length etc.). Parametric sweeps of the simulation inputs can be used to determine the optimum value of each input. The software computes the ABCD matrices and outputs the stability coefficient of the resonator and the 1/e^2 beam radius of a Gaussian beam as it propagates through the resonator. The stability coefficient used by WinLase is derived from the g-parameters of the resonator mirrors, which is an alternative quantification of resonator stability to that in Equation 1-5.

$$0 < g_1 g_2 < 1 \quad , \quad g_i = 1 - \frac{L}{ROC_i} \qquad \text{(Equation 1-6)}$$

As an example, the two-mirror laser shown in Figure 1-1 has two g-parameters defined by Equation 1-6 [21]. The variable L is the optical roundtrip length of the resonator and ROC is the radius of curvature of the resonator mirror. To form a stable resonator, the product of the g-parameters must be a value between 0 and 1. More theory on resonator stability can be found in literature, e.g. [21]. When designing resonators with more than two mirrors, as was the case for this thesis, the theory & calculations become more complex and thus the use of a tool such as WinLase becomes invaluable. Use of the WinLase tool is further described in later chapters in accordance with the designed lasers.

1.1.4. The rate equations

Following the design of a solid-state laser, its dynamic time-dependent behaviour, known as the laser dynamics, can be characterised using a pair of coupled rate equations. Under the assumption that longitudinal and radial variations within the gain medium are ignored, and only one transverse cavity mode is present, the simplified differential rate equations can quantify the population inversion density N (1/cm^3) and the radiation density of a laser ϕ (J/cm^3) at any given time using Equation 1-7 & Equation 1-8 respectively.

$$\frac{dN}{dt} = -\gamma N \phi \sigma c - \frac{N + N_t(\gamma - 1)}{\tau_f} + W_p(N_t - N) \qquad \text{(Equation 1-7)}$$

$$\frac{d\phi}{dt} = \frac{l_a}{l_c} c \phi \sigma N - \frac{\phi}{\tau_c} + S \qquad \text{(Equation 1-8)}$$

An in-depth analysis of the rate equations can be found in [20], where calculations of aspects such as the laser threshold, laser output power and temporal characteristics are described.

Equation 1-7 describes the rate of change of the population inversion density in three subparts: decay due to stimulated emission, decay due to spontaneous emission and gain due to optical pumping. The influence of stimulated emission is dependent on the photon density ϕ, the stimulated emission cross section σ, the speed of light c and an inversion reduction factor γ. Spontaneous emission is dependent on γ and introduces the total population density n_t and the fluorescent lifetime of the metastable level τ_f. Optical pumping is dependent on n_t and includes the pump rate W_p. The inversion reduction factor γ quantifies the change in population inversion density due to the emission of a single photon. In three-level lasers the function $\gamma=1+g_1/g_0$ is yielded, where g_1 and g_0 are the degeneracies of the upper laser level and the ground level respectively. In four-level lasers, $\gamma=1$ is yielded.

Equation 1-8 describes the rate of change of the photon density within the resonator as three subparts: increase due to stimulated emission, decay due to resonator losses and noise. The length of the gain medium, l_a, and the length of the resonator, l_c, contribute to the stimulated emission occurring within the gain medium. Resonator losses are dependent on the photon density, ϕ, and the cavity lifetime of the photons, τ_c. The term S defines the noise accumulated by spontaneous emission at the laser wavelength.

1.1.5. Q-switching

Rapidly switching the losses of a resonator, and inherently the quality factor Q, is known as Q-switching and is a technique used to generate laser pulses. The generated pulses exhibit peak powers several orders of magnitude greater than the laser output power that can be achieved in continuous wave (CW) mode. A diagram illustrating the temporal behaviour of a Q-switched solid-state laser is shown in Figure 1-3.

The population inversion density within the gain medium is first increased through optical pumping to n_i. By enforcing high losses (ε_{max}), the population inversion density is increased to a very high level, far exceeding that of the laser threshold condition achievable under low loss operation (n_t). Switching to low losses (ε_{min}) then causes the population inversion density to deplete rapidly to n_f through stimulated emission. This results in a rapid build-up of photon density within the resonator to ϕ_{max}. The pulse is then terminated through gain saturation and the resonator losses are returned to high to complete the cycle.

In the case that the switching speed is near instantaneous, the term ‘fast Q-switching’ can be assumed since the duration of the emitted pulse is considerably shorter than the time constants of optical pumping and spontaneous emission. This is the case for the diagram in

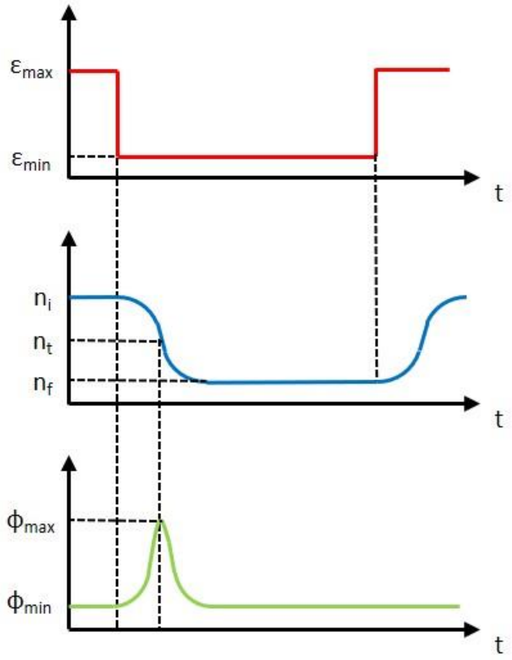

Figure 1-3: Diagrams showing the temporal characteristics of a Q-switched solid-state laser, where ε is the resonator losses, n is the population inversion density, and ϕ is the photon density.

Figure 1-3. Fast Q-switching is commonly achieved actively using an electro-optic modulator (EOM) or an acousto-optic modulator (AOM). A passive method of fast Q-switching can also be realised by using a saturable absorber, e.g. a semiconductor saturable absorber mirror (SESAM). The alternative term ‘slow Q-switching’ is assumed when the switching speed can only be accurately expressed as a time dependent function of the resonator losses. Rotating prisms and rotating mirrors are examples of slow Q-switch devices, where the formation of multiple low-amplitude pulses may be observed when the switching speed becomes too slow.

The rate equations can be used to predict the temporal output properties of a Q-switched solid-state laser. In most cases, the pulse duration is short enough to neglect the optical pumping and spontaneous emission terms. The resulting rate equations are defined by Equation 1-9 and Equation 1-10 [20], where $\varepsilon(t)$ is a time-dependent function of the losses per roundtrip of the resonator and τ_r is the time taken to complete a roundtrip of the resonator.

$$\frac{dN}{dt} = -\gamma N \phi \sigma c \qquad \text{(Equation 1-9)}$$

$$\frac{d\phi}{dt} = \phi\left(\frac{l_a}{l_c}c\sigma N - \frac{\varepsilon(t)}{\tau_r}\right) \qquad \text{(Equation 1-10)}$$

The term $\varepsilon(t)$ is defined by Equation 1-11 [20], where δ_{oc} is the loss from the output coupler, δ_0 is the loss from scattering & absorption and $\delta_t(t)$ is the loss introduced by the Q-switch mechanism. In fast Q-switching, the term $\delta_t(t)$ can be accurately defined by a step function. A more complex loss function is required for slow Q-switching. For example, the loss function introduced by a scanning MEMS mirror is reported in [18], where the calculated temporal output properties of the Q-switched laser yielded a close comparison to those measured experimentally.

$$\varepsilon(t) = -\ln(\delta_{OC}) + \delta_0 + \delta_t(t) \qquad \text{(Equation 1-11)}$$

Q-switching can be performed under either continuous or switched optical pumping. Under continuous optical pumping, a continuous train of laser pulses is obtained with a pulse rate defined by the Q-switch device. The pulse repetition rate of such lasers is typically in the kHz range and optical pumping is done using diode bars or CW laser sources. Under switched optical pumping, the pulse rate of the laser is synchronised to the frequency of the optical pump emission. Optical pumping in this case is done using a flash lamp, which enables convenient pulse-on-demand functionality.

1.1.6. Wavelength tuning

The absorption band and the fluorescent line of a gain medium have a spectral linewidth which is broadened by state lifetime, dipolar fields, thermal vibrations and lattice inhomogeneities. Solid-state gain media with large spectral linewidths can be exploited through tunable output wavelength enabled by optical filters such as dispersing prisms, diffraction gratings, etalons and birefringent filters.

Wavelength tuning using a prism is governed by Equation 1-12 (Snell's Law), where n_1 is the refractive index of the input medium, θ_i is the angle of incidence, n_2 is the refractive index of the output medium, and θ_t is the angle of transmittance. The wavelength tuning mechanism itself relies on the wavelength dependence of the refractive index. Tuning in this case can be achieved by combining a prism with a mirror [23-25] or by combining a prism-pair with a movable aperture. Rotating the mirror or moving the aperture then selects the laser wavelength with minimum losses within the resonator.

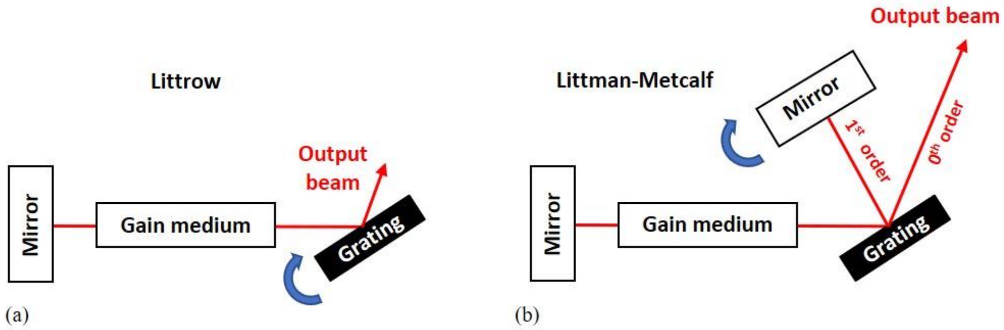

Figure 1-4: Diagrams showing methods of laser wavelength tuning based on (a) the Littrow configuration, and (b) the Littman configuration.

Wavelength tuning using a diffraction grating is defined by the grating equation given in Equation 1-13, where d is the slit spacing, θ_i is the angle of incidence, m is the diffraction order and λ is wavelength. Tunable laser configurations using diffraction gratings are based on either the Littrow or the Littman configuration, shown in Figure 1-4. In the Littrow configuration the first-order diffraction mode of the grating is used as a reflective end-mirror and the zero-order diffraction mode is used as the laser output beam. Rotating the grating then selects the laser wavelength with minimum losses within the resonator. The method is simple but comes with the disadvantage of the output beam changing direction as the wavelength is tuned. This disadvantage can be eliminated by using the Littman configuration which uses the grating combined with an end mirror. Rotating the end mirror then determines the laser wavelength and a unidirectional output beam is achieved.

$$n_1 \sin\theta_i = n_2 \sin\theta_t \qquad \text{(Equation 1-12)}$$

$$d(\sin\theta_i + \sin\theta_m) = m\,\lambda \qquad \text{(Equation 1-13)}$$

Wavelength tuning using an etalon relies on interference between the light reflected off two planar surfaces. Maximum transmission is achieved when constructive interference occurs, which is influenced by the tilt angle of the etalon. Alternatively, birefringent filters rely on the extremely high transmittance of p-polarised light when tilted at the Brewster angle. The birefringence then results in wavelength dependent losses, which can be tuned via the tilt angle of the filter.

Alternative techniques for laser wavelength tuning are based on temperature and resonator length. Temperature influences the refractive index of the gain medium which shifts the gain spectrum, an effect which is exploited in semiconductor lasers, e.g. [26]. Tuning of the length of the resonator shifts the relative wavelengths of the resonator modes and has been widely reported using MEMS mirrors in VCSEL's [12] and semiconductor lasers [13]. The effects of temperature and resonator length are not generally exploited in solid-state lasers and are therefore out with the scope of this thesis.

1.1.7. Summary

The fundamental theory behind the operation of solid-state lasers was introduced in this section. Different laser gain media, methods of optical pumping and the design of the laser resonator were described. The rate equations used to compute the dynamic time-dependent behaviour of the laser output were also introduced. The concepts of Q-switching and laser wavelength tuning were described along with the different techniques used to achieve them. Other laser tuning concepts such as adaptive optics and mode-locking were not included because they are out with the scope of this thesis. The above-described theory was used in the design of the lasers reported in later chapters.

1.2. MEMS mirrors

The extensive research of MEMS mirrors and associated actuators has led to many novel devices fabricated using different materials. As well as the standard silicon and metallic elements which are typically used in optics, a non-exhaustive list of other investigated materials includes: polysilicon [27], silicon nitride - SiN [28, 29], SU-8 photoresist [30], polydimethylsiloxane - PDMS [31], lead zirconate titanate - PZT [32], black silicon [33] and vanadium dioxide - VO_2 [34]. Nevertheless, while the choice of material can be application specific, by far the most common material used in the fabrication of MEMS mirrors is single crystal silicon (SCS). The properties of SCS are well-defined and characterised in literature [35-37] and already established manufacturing processes that align with integrated circuit technology are common. In addition to pure research, SCS MEMS scanner modules have also been commercialised [7, 11, 38]. This section provides an overview of the fabrication processes associated with MEMS mirrors, the fabrication process chosen for the MEMS mirrors used in this thesis, and the different methods of MEMS actuation.

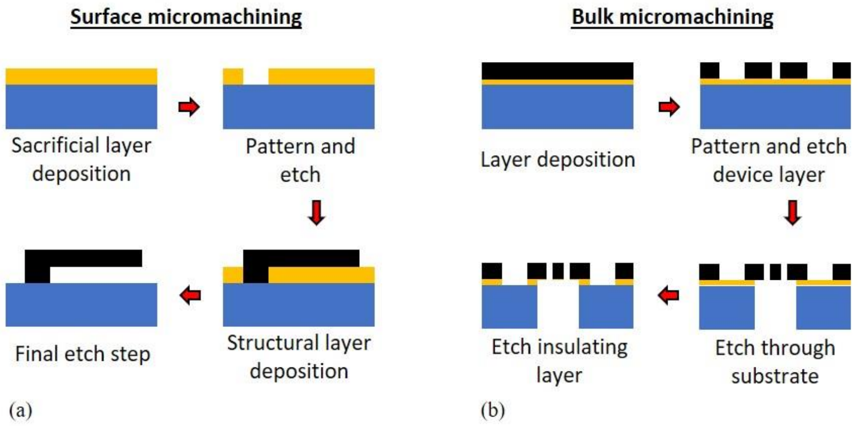

Figure 1-5: Diagrams illustrating typical processes for (a) surface micromachining and (b) bulk micromachining of silicon MEMS mirrors.

1.2.1. Fabrication

Two fabrication processes are most commonly used for MEMS mirrors: surface micromachining and bulk micromachining. Both techniques use a series of deposition, masking, patterning and etching steps to produce a functional device comprising movable mechanical structures, optical materials and electrical interconnects.

Surface micromachining uses etching of a sacrificial layer to release a functional micro-structure from a substrate, as shown in Figure 1-5a. The substrate then acts as a base support and mechanical movement of the device is enabled through a thin airgap. In bulk micromachining, shown in Figure 1-5b, the substrate can be an integral part of the device functionality as well as providing a base support. The top layer is patterned and etched then the wafer is flipped, and the substrate is etched. The resulting cavity releases the patterned top layer, enabling flexible movement capabilities and optical pathways. Both techniques provide their own benefits and choosing the most suitable process is dependent on the application.

1.2.2. Multi-user MEMS process

The MEMS mirrors used for the work described in this thesis were fabricated using a commercially available bulk micromachining process offered by the foundry Memscap Inc. The process known as SOIMUMP's is a silicon-on-insulator multi-user MEMS process which was specifically designed for fabricating optical MEMS. Multi-project wafers are supported, making the process cost-efficient and highly suitable for scientific research. SOIMUMP’s has been well-characterised in literature [36, 39] and by Memscap themselves [40]. The process has also been used extensively by the CMP for many years to investigate MEMS mirrors, actuators and sensors. The CMP orders its designs according to the rules provided by Memscap, who then fabricate a defined number of devices according to the given specifications. The submitted designs typically have multiple MEMS devices integrated into a single 1 x 1 cm^2 die.

The fabrication steps of SOIMUMP’s follow the previously described bulk micromachining process shown in Figure 1-5b. A 400 µm thick layer of n-doped silicon is used as the substrate, a 1 µm or 2 µm thick buried oxide layer is used for insulation, and either a 10 µm or 25 µm thick SCS layer is used as the device layer. The SCS layer is doped with phosphorous to enhance its electrical conductivity, but at the expense of surface flatness due to the resulting intrinsic stress. Layers of gold are also possible to provide electrical interconnects, bimorph mechanisms and broadband reflectance. An in-depth description of the process flow can be found in the SOIMUMP’s design handbook [40]. SOIMUMP’s will be further discussed and characterised in Chapter 2 in accordance with the MEMS mirrors designed for the work described in this thesis.

1.2.3. Principles of mirror actuation

Actuation of MEMS mirrors can be summarised in four categories: electrostatic, magnetic, thermal and piezoelectric. These actuation techniques can be used independently or as hybrids to generate movement of a mirror. The resulting mirror movement can be dynamic in the form of scanning or static in the form of fixed displacement or tilt angle. Dynamic movement can be achieved by synchronising the frequency of the electrical driving signal with the mechanical resonance of the mirror structure. Static movement can be achieved using a fixed voltage or current to induce a force or stress on the mirror, resulting in fixed mirror deflection or deformation.

Electrostatic actuation

Electrostatic actuation was the principle used for the first MEMS mirror device [2] and is one of the most commonly used since. The principle relies on the attraction of electrodes with an applied potential difference to induce movement of the mirror structure. The resulting force applied to the mirror, F, is defined by Equation 1-14, where ε and A are the dielectric constant and the surface area of the electrodes respectively, d is the distance separating the

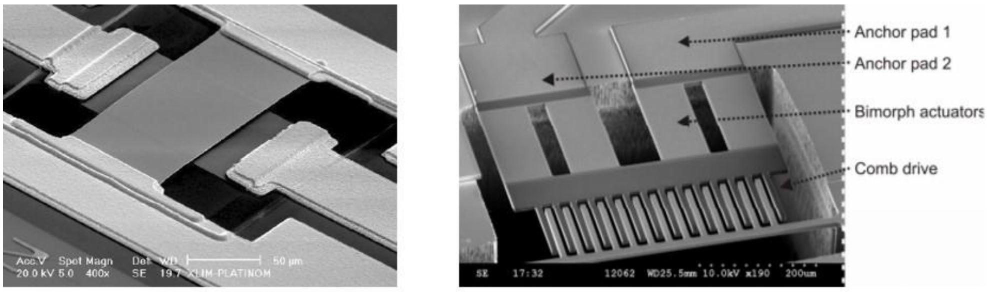

(a) (b)

Figure 1-6: Examples of electrostatic actuators for MEMS mirrors using (a) the parallel plate method [41, © 2006 IOP] and (b) the comb-drive method [43, © 2014 IEEE].

electrodes and V is the potential difference between the electrodes. The potential difference can either be constant to induce a defined force or a dynamic time-dependent term to induce resonant scanning.

$$F = \varepsilon \frac{A}{2\, d^2} V^2 \qquad \text{(Equation 1-14)}$$

Electrostatic actuation of MEMS mirrors has been reported using two methods: parallel plates and comb-drives. An example of a parallel plate actuated mirror is shown in Figure 1-6a [41]. The layered structure of the parallel plate method allows simple facilitation of static mirror movement, where the upper electrode is usually pulled towards the lower electrode. A prevalent example of the parallel plate method is the digital micromirror device by Texas Instruments, where two discrete mirror tilt angles define the on/off status of the device [42]. The parallel plate method can also be used for resonant actuation of MEMS mirrors, as was the case with the first reported MEMS mirror device [2]. The device yielded a maximum mechanical tilt angle of 0.5° in either direction with a resonant frequency of 15 kHz, resulting in a total optical scan angle (TOSA) of 2°.

To achieve larger scan angles with the parallel plate method, the distance separating the electrodes must be increased resulting in a large increase in the required driving voltage. For this reason, comb-drive actuators overshadow parallel plate actuators in relation to resonant scanners. An example of a comb-drive actuated mirror is shown in Figure 1-6b [43]. Comb-drives operate by means of interleaving sets of fixed combs and moving combs with a potential difference between them. The condensed design of the interleaving comb electrodes provides an ideal platform to generate large force with low driving voltage. Resonant scanning with a large TOSA is thereby feasible, even exceeding 80° [18], while

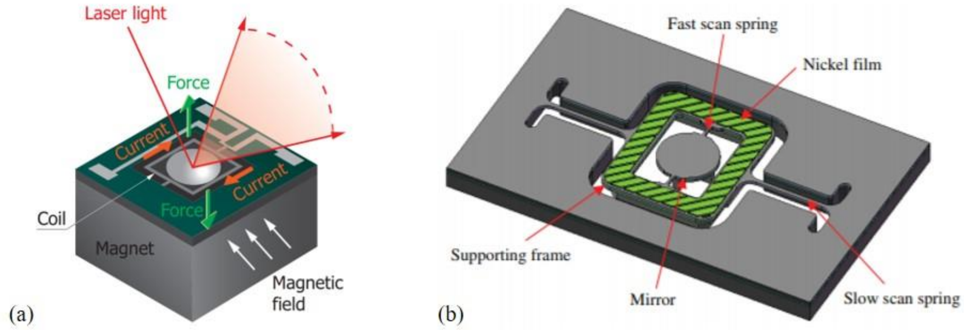

Figure 1-7: MEMS mirrors using magnetic actuation: (a) Hamamatsu MEMS mirror module using Lorentz force [46, © Hamamatsu Photonics K.K.], and (b) MEMS mirror with a ferromagnetic actuator mechanism [48, © 2002 IEEE].

static movement is mostly prohibited due to little or no vertical displacement between the fixed combs and the moving combs.

Resonant scanning has been achieved using three comb-drive configurations: in-plane comb-drives, staggered vertical comb-drives (SVC's) and angular vertical comb-drives (AVC's). In-plane comb-drives enable out-of-plane movement via spring structures applied to the moving comb section, e.g. [44]. The resulting flexure allows the moving combs to oscillate around the fixed combs. Of the three configurations, in-plane comb-drives often yield the lowest scan angle due to the miniscule vertical offset between the fixed and moving combs. SVC's and AVC's purposely use an initial offset between the fixed and moving combs to amplify the scan angle. In the case of SVC's, the offset is created using a multi-layered fabrication process [45]. The offset in AVC's can be generated by stressing the fixed combs so that they bend on the out-of-plane axis of the moving combs. This can be achieved by e.g. heating of a bimorph structure (two materials with different thermal expansion coefficients).

Magnetic actuation

Magnetic actuation of MEMS mirrors has been reported using two principles: the Lorentz force and ferromagnetism. The former uses one or more permanent magnets and current flow through a coil of wire fabricated on the MEMS structure. The net force incident on the wire is then defined by Equation 1-15, where B, I and L are vectors defining the magnitude and orientation of the magnetic field, the current flow and the length of the wire respectively. The magnetic force acting on the coil then induces movement of the mirror.

$$F = B\ I\ L \qquad \text{(Equation 1-15)}$$

An example of a commercialised MEMS mirror module by Hamamatsu that uses the Lorentz force method is shown in Figure 1-7a [46]. The Lorentz force principle was also used for the first reported magnetically driven MEMS mirror [47]. A maximum mirror tilt angle of 8° was achieved in either direction from the mirror rest position by applying a current of ± 325 mA. The Hamamatsu device yields a similar performance characteristic but with as little as 20 mA driving current, achieved through rigorous optimisation.

Using ferromagnetism to actuate a MEMS mirror involves a ferromagnetic layer deposited on the mirror structure. The strength and orientation of an externally applied magnetic field then exerts a magnetic force on the MEMS mirror. An example of such a mirror is shown in Figure 1-7b, where a Nickel film was deposited on the actuator surface [48]. A solenoid positioned underneath the die generated a magnetic field orientated at an angle to the surface of the actuator. The actuator then aligned with the magnetic field and tilted the mirror. A TOSA of up to 13° was achieved with 2D scanning capability.

The main advantage of using magnetic actuation for MEMS mirrors is the scaling of force with mirror size, which enables efficient operation of larger devices. The linearity of magnetic actuation also makes it attractive for applications requiring low frequency scanners. However, disadvantages also arise from the power consumption and the spatial requirements, which are larger than those of other actuation methods.

Thermal actuation

Thermal MEMS actuators most commonly involve thermal expansion through Joule heating, i.e. heat induced by current flow. The temperature (T) distribution along the length x of a beam over time t can be derived from the one-dimensional heat equation given in Equation 1-16 [49], where k is thermal conductivity, ρ is density, C is heat capacity, V is the applied potential difference, A is cross-sectional area of the beam and R is the electrical resistance of the beam. The equation considers both heat conduction and heat generated by electrical power, whereas convection and radiation effects are neglected [50].

$$\frac{\delta T(x,t)}{\delta t} = \frac{k}{\rho\, C}\frac{\delta^2 T(x,t)}{\delta x^2} + \frac{V(t)^2}{R\,\rho\, A\, C} \qquad \text{(Equation 1-16)}$$

Thermal expansion and Joule heating of MEMS are usually exploited in one of two ways: the bimorph effect or the hot & cold method. The bimorph effect relies on a layered structure where the bottom layer (silicon) has a different thermal expansion coefficient to that of the top material, which is often metallic. The materials therefore expand at different rates when heated and the mismatch causes the structure to bend. An example of a bimorph-actuated

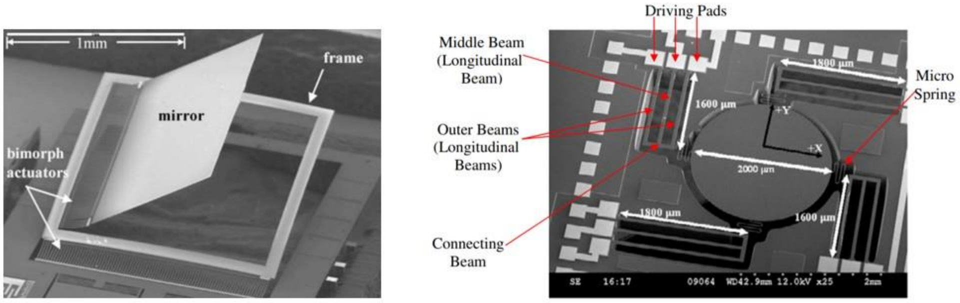

(a) (b)

Figure 1-8: Diagrams showing thermal MEMS actuators using: (a) the bimorph effect [51, © 2004 IEEE], and (b) the hot & cold arm method [52, © 2011 IOP].

MEMS mirror is shown in Figure 1-8a, where two perpendicular aluminium layers deposited regionally on a silicon mirror enabled 2D mirror tilt with a mechanical tilt angle up to 64° [51]. The hot & cold method uses a single material layer, an example of which is shown in Figure 1-8b [52]. In this case, current flow was supplied to the outermost ‘hot’ beams while no current flowed through the ‘cold’ middle beam. The hot beams therefore expanded more than the cold beam and the mismatch caused structural bending, resulting in 2D mirror tilt with a mechanical tilt angle up to 1.3°. A resonant scanning mirror with a TOSA of 10° was also reported using the same actuator mechanism [49].

The selling point of thermal actuators is their capability of large static displacement using a voltage in the single digits. Using the bimorph effect, MEMS mirrors with optical tilt angles exceeding 60° have been reported using a voltage of only 5.5 V [53]. A MEMS mirror with mechanical tilt of 124° was even achieved at a voltage of 12.5 V [54]. As well as mirror tilt, the bimorph effect has also been reported for deformable mirrors, e.g. where a silicon-gold bimorph device was used in an imaging system [55]. The drawbacks of thermal actuators are their slow response time and their large power consumption when compared to other actuation methods. Nevertheless, their capability of large static deflection renders them highly useful for beam steering and imaging applications.

Piezoelectric actuation

The use of piezoelectric thin films such as Lead Zirconate Titanate (PZT) has drawn a lot of recent interest for MEMS mirror actuation. Piezoelectric actuation of MEMS mirrors has been shown to be capable of rapid scanning with significantly lower voltage demand than electrostatic actuation. Furthermore, the shielding and additional spatial requirements required for magnetic scanners are avoided. The main drawback of PZT is the difficulty in

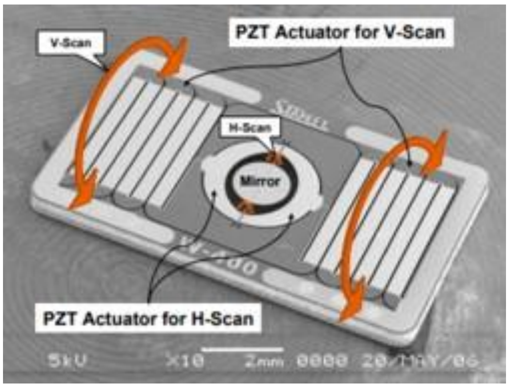

Figure 1-9: An example MEMS scanner using integrated piezoelectric actuators [58, © 2006 IEEE].

its integration into the fabrication process of optical MEMS mirrors. However, recent advancements in fabrication technology have enabled simpler integration, e.g. [56].

The operating principle involves the stress created in a piezoelectric thin film under the influence of an applied electric field. This strain then leads to actuator bending in a similar manner to that of thermal actuation. An in-depth analysis of the mechanism can be found in [57]. An example of a PZT actuated MEMS mirror is shown in Figure 1-9 [58]. The mirror was used for raster scanning, with one slow axis of 60 Hz and one fast axis of 11.2 kHz. Optical scan angles of 39° and 29° were measured on the fast and slow axes respectively.

1.3. MEMS lasers

The most common application of MEMS in laser systems is beam steering, which is the functional base of projectors, barcode readers and biomedical imaging systems. The rapid scanning capability, small footprint and low energy demand of MEMS mirrors are exploited to produce highly efficient and compact systems. The MEMS mirrors are not a physical part of the laser source itself but rather an external spatial light modulator to re-direct the output beam. The focus of this thesis is on MEMS mirrors which are an integral part of a laser source to tune the intrinsic properties of the output beam. This subsection provides an overview of the reported usage of MEMS mirrors as active tuning elements for the temporal, spectral and spatial characteristics of laser output beams.

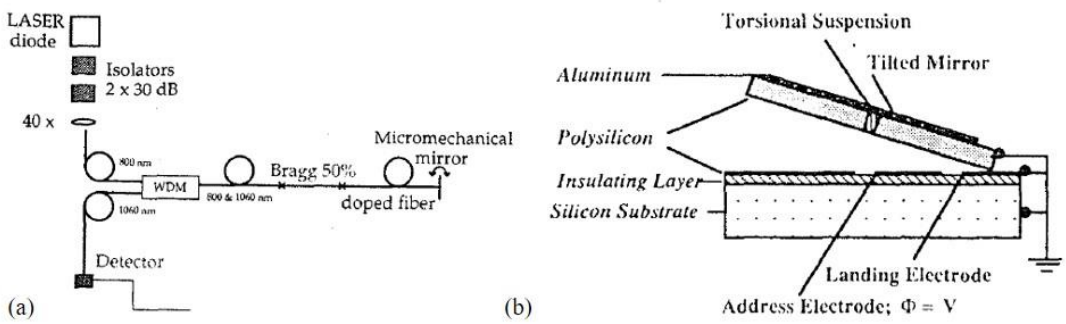

Figure 1-10: Fibre laser with Q-switching enabled by a MEMS mirror: (a) laser schematic, (b) MEMS mirror design [14, © 1996 IEEE].

1.3.1. Q-switching and mode-locking

Tuning the temporal output characteristics of solid-state lasers using MEMS mirrors has been reported in two forms: Q-switching and mode-locking. The concept of laser Q-switching was introduced previously in Section 1.1.5. Mode-locking involves interference between the longitudinal modes oscillating within a laser cavity. Synchronisation of these modes results in periodic occurrences of cumulative constructive interference, leading to an ultrafast switching mechanism capable of producing femtosecond pulses. The conventional laser Q-switching and mode-locking techniques are bulky, tend to have demanding electrical requirements, and introduce losses into the laser system. The prospect of replacing them with a MEMS mirror which also functions as a resonator mirror is therefore an appealing possibility.

Mode-locking enabled by a MEMS mirror has been previously demonstrated in an Erbium doped fibre laser, or EDFL [16]. A section of the deformable membrane mirror was vibrating at 5 MHz to induce a small change in the quality factor of the resonator. Laser output pulses of 1 ns were measured with peak powers of 20 W. To this date, this is the only report of a MEMS mirror being used to enable laser mode-locking.

The first reported use of a MEMS mirror for laser Q-switching was in a Nd: doped fibre laser, shown in Figure 1-10a [14]. The MEMS mirror, shown in Figure 1-10b, was positioned near the end of the fibre, and its scan angle controlled the losses within the resonator. The MEMS mirror was bulk micromachined and consisted of a 50 x 70 µm polysilicon base with an optical coating of aluminium. Electrostatic parallel plate actuation was used where applying a potential difference of 35 V pulled the mirror to a landing electrode at an angle of 2.6°. The resulting mirror tilt was used as the Q-switch mechanism.

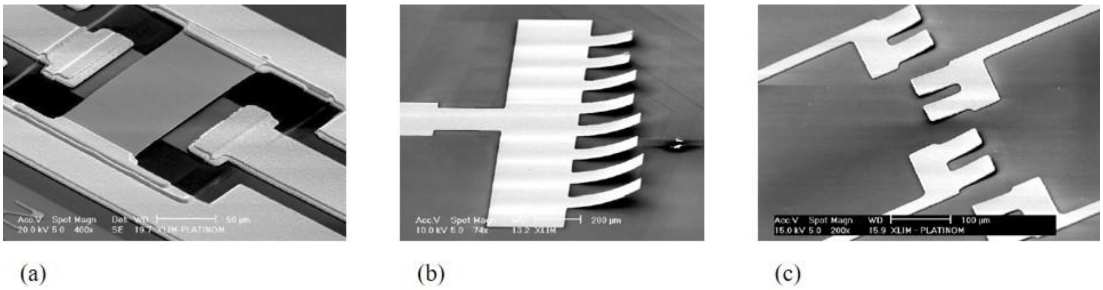

Figure 1-11: SEM images of MEMS mirrors used as Q-switch mechanisms in fibre lasers: (a) membrane bridge mirror used in an EDFL [41, © 2006 IOP], (b) cantilever mirror used in an Yb: doped fibre laser [15, Reprinted with permission from the OSA], (c) cantilever mirror array used in multiple EDFL's with a combined laser output [63, reprinted with permission from the OSA].

The Q-switched laser yielded an average output power of 3 mW for an absorbed pump power of 16 mW, with peak pulse powers of up to 300 mW and full-width half maximum (FWHM) pulse durations of 2 μs. Q-switch pulse rates from 1 kHz to 30 kHz were investigated, where only the faster pulse rates (> 20 kHz) yielded Q-switching due to the slow switching speed. This report was followed up by a report of the same laser with a MEMS mirror driven by an electrostatic comb-drive [59]. Similar performance characteristics were measured at Q-switch rates of up to 60 kHz.

A similar Q-switch concept was reported for an EDFL in [41]. The MEMS mirror in this case was a gold membrane suspended over a silicon electrode, shown in Figure 1-11a. Electrostatic parallel plate actuation enabled deformation of the mirror surface, deflecting the beam away from resonator alignment. Pulse durations of 320 ns and 1 µs were achieved at repetition rates of 30 kHz and 120 kHz respectively, with peak pulse powers of up to 3 W. The same MEMS mirror was also used in a synchronised tunable fibre laser [60]. In this case, the MEMS mirror was used to simultaneously Q-switch two fibre lasers, which were then synchronised at the output to produce a laser output in the visible spectrum. Digital micromirror devices have also been used to actively Q-switch an EDFL, with pulse durations of 3.2 µs at a repetition rate of 66 Hz [61].

To obtain shorter Q-switch pulse durations, a cantilever type MEMS mirror (see Figure 1-11b) was designed and reported in [15]. The cantilever was an Au/Cr/Au layered structure, where thermal stresses from the fabrication process resulted in an upwards tilt of the cantilever. Electrostatic parallel plate actuation was then used to pull the cantilever towards the silicon substrate. The MEMS mirror was demonstrated in an Yb: doped fibre laser, achieving pulse durations as short as 20 ns at repetition rates of up to 200 kHz, with peak

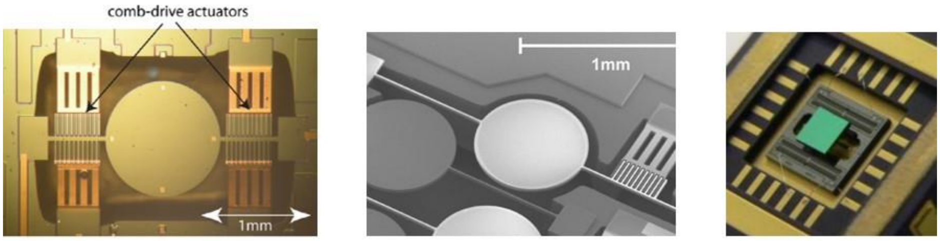

(a) (b) (c)

Figure 1-12: Microscope images of MEMS mirrors used as Q-switch mechanisms in solid-state lasers: (a) gold-coated MEMS mirror used in a Nd: YLF laser [17, reprinted with permission from the OSA], (b) dielectric-coated MEMS mirror used in a Nd: YAG laser [18, © 2015 IEEE], (c) dielectric-coated mirror assembled on top of a micro-actuator and used in an Er/Yb: glass laser [67, © 2015 SPIE].

pulse powers of 19 W. Further optimisation of the laser cavity then led to pulse durations as short as 8 ns [62].

An array of similar cantilever type MEMS mirrors (Figure 1-11c) was reported in [63] for use in four separate EDFL's, where the laser outputs were spectrally combined to form a single laser output. In doing so, higher Q-switch repetition rates could be achieved without degrading the pulse duration. The final laser output yielded cumulative output power and pulse durations of 400 ns at a repetition rate of 80 kHz. Another cantilever type MEMS mirror was reported to enable Q-switch pulse durations of 564 ps in a microchip-fibre hybrid laser [64]. A Q-switched microchip laser has also been reported, enabled by a piezoelectric deformable MEMS mirror vibrating at a frequency of 670 Hz. Q-switch pulse durations of 16 ns were achieved at a repetition rate of 1.4 kHz, with peak pulse powers of 52 W.

Scanning MEMS mirrors have been reported as active Q-switch elements in solid-state lasers. The investigations used MEMS mirrors scanning at their mechanical resonance to tune the resonator losses. In [17], a 3-mirror Nd: YLF laser was Q-switched by a MEMS mirror driven by a set of double-sided comb-drives, shown in Figure 1-12a. The mirror was coated with a layer of gold and could be driven at 6 kHz, 10 kHz, 30 kHz or 41 kHz. A Q-switch repetition rate of double the driving frequency was yielded due to a double-pass of the cavity alignment during a single movement cycle of the mirror. Pulse durations between 430 ns and 2 µs were measured with a peak pulse power of up to 6.5 W.

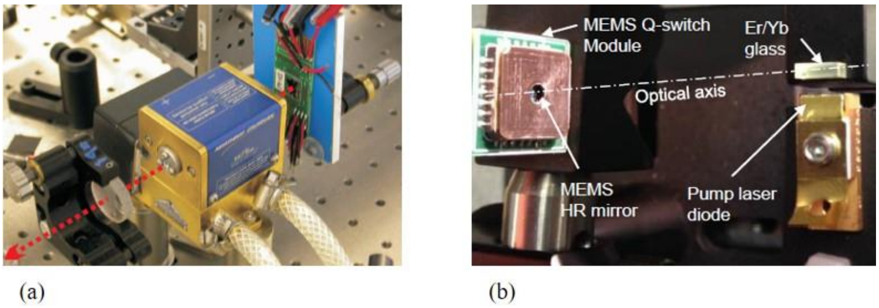

Figure 1-13: Solid-state lasers incorporating MEMS mirrors as active Q-switch elements: (a) Nd: YAG laser using the MEMS mirror from Figure 1-12b [18, © 2015 IEEE], and (b) Er/Yb: glass laser using the MEMS mirror from Figure 1-12c [67, © 2015 SPIE].

Another report investigated similar use of a MEMS mirror with a single-sided comb-drive (see Figure 1-12b) in a 3-mirror Nd: YAG laser [18]. A high-reflectance dielectric coating was deposited on the mirror surface to enable power-scaling of the laser output. Pulse durations of 110 ns were measured at a repetition rate of 16 kHz, with a peak pulse power of 350 W. The same mirror with a gold-coating was also used in a two-mirror Nd: YAG laser, shown in Figure 1-13a [65]. Pulse durations as short as 30 ns were measured at a repetition rate of 16 kHz, with a peak pulse power of 30 W. The same gold-coated MEMS mirror design was also used in a compact array to generate multiple laser beams originating from a single Nd: YAG medium [66]. Two output beams with respective Q-switch repetition rates of 8 kHz and 8.7 kHz were achieved.

The above described lasers were limited in output power by (a) the laser damage threshold of the optical coating, and (b) electrostatic pull-in of the comb-drive actuators induced by laser heating. Increasing this limit ultimately comes down to optimising the optical coating deposited on the MEMS mirror in terms of reflectance and flatness, which has proven difficult due to the comparable thickness of the optical coating to that of the MEMS mirror. Masking of the electrical interconnects during coating deposition has also proved to be a challenge due to the compact nature of MEMS chips, since the mask results in shadowing.

A method of overcoming the power-scaling challenges was developed in [67] by using additional process steps during fabrication. A standard 8” silicon wafer with 200 µm thickness was dielectric-coated on both sides to yield a reflectance exceeding 99%, then diced into 1.6 x 1.6 mm squares. The dies were then bonded on top of a MEMS actuator using a pick & place machine. The mirror device, shown in Figure 1-12c, was optically flat

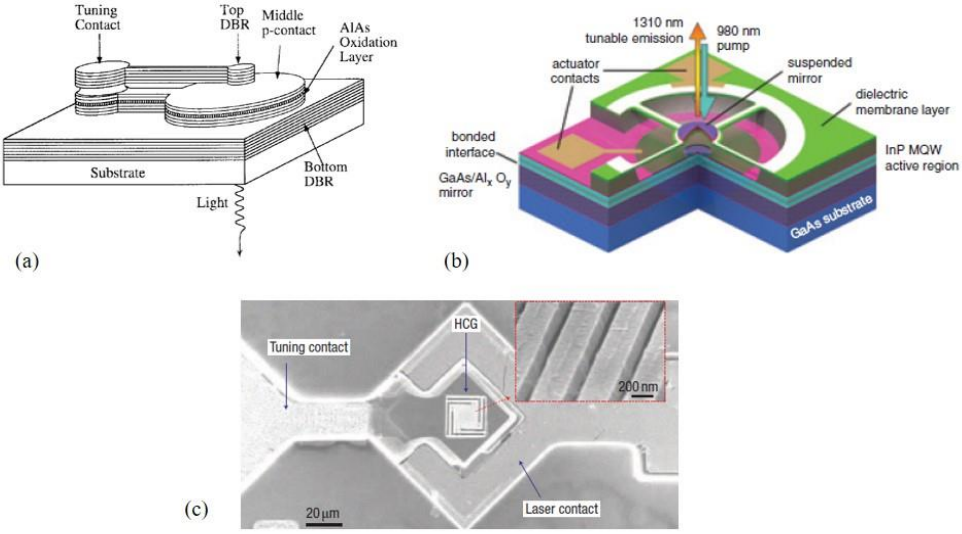

Figure 1-14: MEMS-tunable VCSEL’s: (a) VCSEL with a cantilever type DBR [69, © 1997 IEEE], (b) VCSEL with a suspended membrane type DBR [71, © 2012 IEEE], and (c) nanoscale VCSEL with a high-contrast grating (HCG) [75, © 2008 Nature Photonics].

(ROC > 5 m) and was used in a flash-lamp pumped Er/Yb: glass laser shown in Figure 1-13b. Pulse durations of 20 ns were measured at a repetition rate of 1 Hz, with peak pulse powers exceeding 150 kW. While the method was not based solely on MEMS technology, the achieved laser output power was impressively large and thus compatible with military-grade laser range finding.

1.3.2. Spectral tuning

To this date, spectral tuning of solid-state lasers using MEMS devices is yet to be reported. Wavelength tuning of lasers enabled by MEMS devices has however been reported in VCSEL’s, external-cavity semiconductor lasers, fibre lasers and a distributed feedback laser (DFB). In MEMS-tunable VCSEL’s, extremely short resonator lengths enable a well-defined distribution of resonator modes. Fine tuning of the resonator length then results in a shift in the mode wavelength. A review of MEMS tunable VCSEL’s can be found in [12], detailing a range of VCSEL’s emitting at selected wavelengths from 750 nm up to 1550 nm at laser output powers of up to 5 mW.

Tuning of the resonator length in VCSEL’s is achieved through displacement of the top distributed Bragg reflector (DBR), which is essentially a MEMS mirror. This is mostly

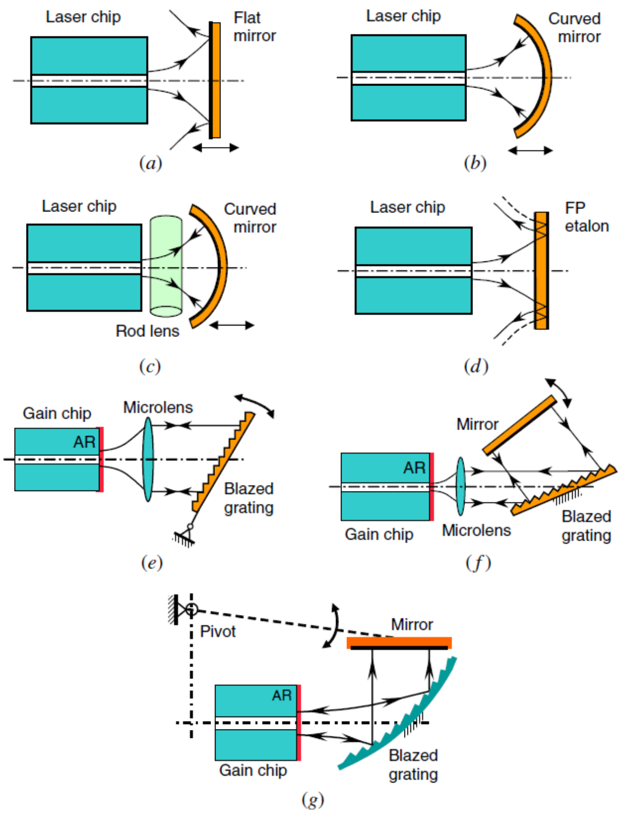

Figure 1-15: Diagrams summarising the wavelength tuning techniques used in MEMS tunable external-cavity semiconductor lasers [13, © 2007 IOP]: (a) lens-less, (b) curved mirror, (c) 3D coupling, (d) etalon, (e) Littrow configuration, (f) Littman configuration, and (g) curved grating.

achieved using electrostatic parallel plate actuation to pull a cantilever or membrane DBR towards the device substrate [68-73]. Static movement results in one-directional tuning of the laser wavelength, whereas resonant movement results in bi-directional wavelength scanning. Examples of devices incorporating electrostatic actuation are shown in Figure 1-14a and Figure 1-14b [68, 71], where the latter achieved an ultra-wide wavelength tuning range of 150 nm. An alternative actuation method for VCSEL's is electrothermal, which exploits the bimorph effect and Joule heating to displace one of the DBR's [74].

A further investigation of miniaturised VCSEL's has even led to a nanoscale actuator [75]. In this case the top DBR was in the form of a high contrast grating with features smaller than 200 nm. Several gratings with varied methods of suspension over an air-gap were investigated, with an example shown in Figure 1-14c. Electrostatic parallel plate actuation was used to achieve a wavelength tuning range of 18 nm. The mass and the electrical power consumption of the grating + actuators were 1000 times smaller than that of MEMS-based

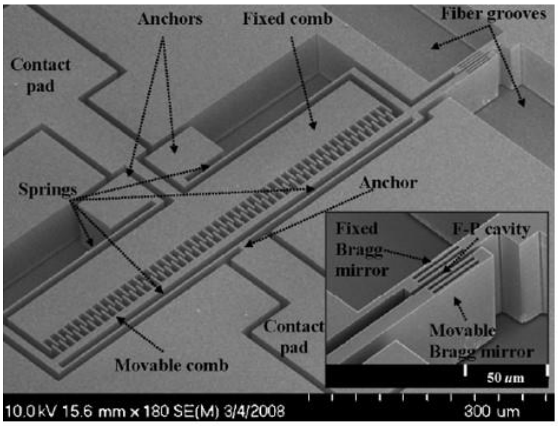

Figure 1-16: MEMS Fabry-Pérot filter used to tune the output wavelength of an EDFL [87, © 2002 IEEE].

DBR’s. The response time was also in the nanosecond regime, 50x faster than that of MEMS-based DBR’s.

In external-cavity semiconductor lasers, tuning of the resonator length and use of grating configurations have been reported based on MEMS techniques. Such lasers have been reviewed in literature and a summary of the tuning techniques is shown in Figure 1-15 [13]. Tuning of the resonator length has been reported using MEMS mirrors driven by electrostatic comb-drives [76-79]. The tunable range of such lasers is typically around 15 nm which can be continuous or with the inclusion of mode hopping. MEMS mirrors in combination with an etalon have also been reported with similar tuning capabilities e.g. [80, 81]. The Littrow and Littman-Metcalf configurations previously described in Section 1.1.6 have also been used in such lasers, e.g. [82-86]. Larger tuning ranges exceeding 100 nm have been demonstrated, with continuous single-mode tuning made possible through accurately positioned pivots.

A distributed feedback laser (DFB) module with the output wavelength selected using a MEMS mirror has also been reported [87]. The device consisted of an array of 12 DFB’s with a pitch of 10 µm and a wavelength spacing of 2.8 nm. Tilting the MEMS mirror using electrostatic actuation then selected which DFB laser was oscillating.

In fibre lasers, wavelength tuning has been reported using MEMS-based Fabry-Pérot resonators. A wavelength tunable EDFL was reported where the length of the MEMS Fabry-Pérot resonator was tuned using an electrostatic comb-drive, shown in Figure 1-16 [88]. A tuning range of 35 nm was achieved at an output power of 1.8 mW and a scanning rate of 14.4 kHz, defined by the mechanical resonance of the MEMS device. A similar technique using an electrothermally actuated Fabry-Pérot resonator was reported in a semiconductor fibre ring laser [89]. In this case a tuning range of 103 nm was achieved at an output power of 1.3 mW. In another report, a similar configuration to the Littman-Metcalf configuration was used to wavelength tune a linear-cavity EDFL and a ring-cavity EDFL [90]. An array of DMD’s was used in combination with a Bragg plate, achieving a tuning range of over 30 nm.

1.3.3. Adaptive optics

Adaptive optics mirrors have been reported in solid-state lasers for intracavity control of the transverse mode profile. In high-power lasers, adaptive optics is used to correct for thermally induced aberrations which reduce the optical quality of the beam and limit the laser output power. The first demonstration of an adaptive optics mirror with an array of micromachined actuators for this purpose was reported for a Nd: YVO_4 laser [91]. A TEM_{00} profile was produced and an increase in laser output power from 20 mW to 120 mW was achieved. Similar mirrors have since been used in a 6 W Nd: YAlO laser and a 15 W Nd: $GdVO_4$ laser to alter the transverse mode shape of the output from highly multi-modal to TEM_{00} [92]. One was also used in a Nd: YVO_4 self-Raman laser to produce a TEM_{00} laser output, where the Raman output power was also increased by 18% to 650 mW [19].

The above-described adaptive optics mirrors had a diameter of 15 mm, which can ultimately be defined as a bulk mirror. The use of a MEMS mirror of 700 µm diameter was recently reported to alter the transverse mode profile of a 200 mW Nd: YAG laser [93]. The mirror was a gold-coated silicon mirror, where the bimorph effect was exploited through heating using a small Peltier device attached to the MEMS substrate. Tuning in this case was limited by the actuation mechanism which could only deform the mirror surface in one frame of reference.

1.4. Summary

Optical MEMS devices have been demonstrated as integrated parts of fibre lasers, semiconductor lasers and solid-state lasers to tune the temporal, spectral and spatial laser output properties. The fundamental operation of such lasers was reviewed, and an overview of the fabrication and actuation techniques of MEMS mirrors was given. The commercial SOIMUMP’s fabrication process for optical MEMS was introduced, which was the process used to fabricate the MEMS mirrors described in later chapters of this thesis.

Temporal tuning using MEMS mirrors has been shown in fibre lasers in the form of Q-switching and mode-locking. Q-switching with MEMS mirrors has also been reported in solid-state lasers and a microchip laser. Adaptive optics has been demonstrated in solid-state lasers using a MEMS mirror and using a bulk mirror with micro-machined actuators. Spectral tuning is widely used in MEMS VCSEL's and external-cavity semiconductor lasers. It has also been demonstrated in fibre lasers but has yet to be demonstrated in solid-state lasers.

The concept of spectral tuning using an intracavity MEMS mirror in a solid-sate laser is demonstrated for the first time in this thesis. The first use of a single intracavity MEMS mirror to simultaneously tune the spectral and temporal output properties of a solid-state laser is also reported. Furthermore, the use of multiple intracavity MEMS mirrors in a single solid-state laser to enable tunable Q-switch parameters is demonstrated.

2. MEMS mirror designs

The MEMS mirrors employed in the laser systems developed in this thesis used two different types of actuation mechanism: electrothermal and electrostatic. They were fabricated using the commercial SOIMUMP’s process by the foundry Memscap Inc., which was introduced in Section 1.2.2. The process was used because it has been used extensively by the CMP for many years to fabricate MEMS devices with reliable results and cost efficiency. The two fabricated mirror types had different mechanical movement capabilities which were each aimed towards enabling different laser functionalities. The underlying SOIMUMP’s process is described in more detail in Section 2.1. The MEMS mirror with electrothermal actuation, referred to as the ET mirror, is then introduced and characterized in Section 2.2. Finally, in Section 2.3, the design of an array of MEMS mirrors with electrostatic comb-drive actuation, known as ES mirrors, is presented and characterized.

2.1. Fabrication using SOIMUMP’s

2.1.1. Process

The SOIMUMP’s process is a commercial bulk micromachining process which is illustrated in Figure 2-1. The process starts with the bonding of two silicon wafers with an insulating oxide layer between. The back-side wafer is grinded to a thickness of 400 µm and the front-side wafer is grinded to a thickness of either 10 µm or 25 µm depending on the demands of the customer. The resulting 400 µm thick substrate is used as the base support of the MEMS device which is formed on the 10 µm or 25 µm thick device layer. The oxide layer provides electrical and thermal insulation and is either 1 µm or 2 µm thick depending on the chosen thickness of the device layer. The in-plane layout of the device layer is designed by the customer to form the functional parts of the MEMS device after the fabrication process is complete.

The device layer is doped with phosphorus via diffusion to enhance the electrical conductivity of the layer. A 500 nm thick layer of gold is then deposited on the device layer via shadow masking and electron beam deposition to form the electrical interconnects and bond pads, with a 20 nm thick layer of chrome between to strengthen the adhesion. The device layer is then lithographically patterned, and plasma etched down to the oxide layer.

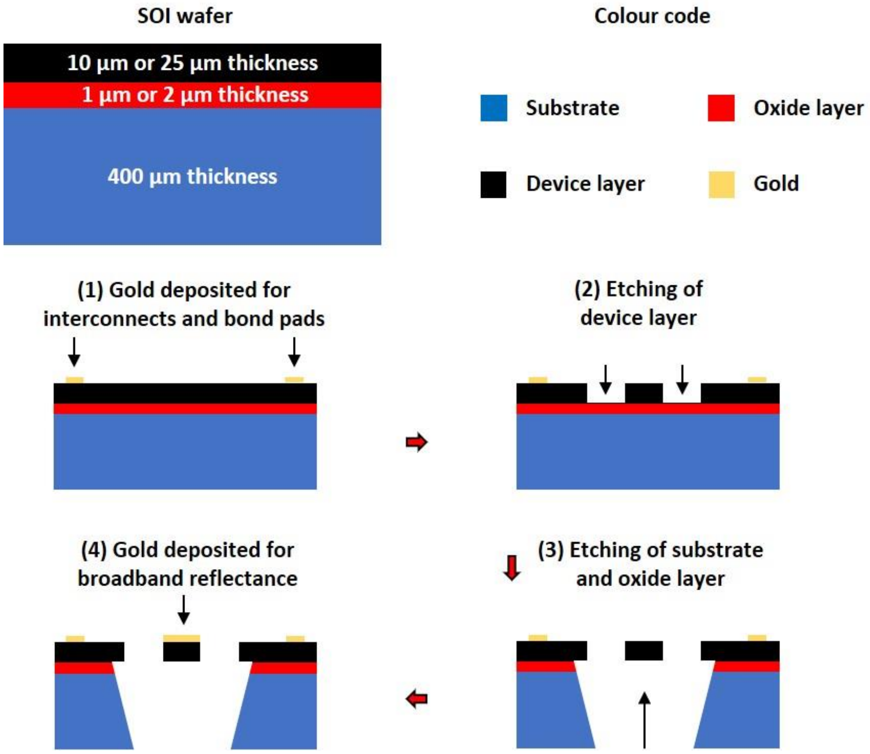

Figure 2-1: Diagram of the SOIMUMP’s process by the foundry Memscap Inc.

The wafer is flipped, and the substrate is lithographically patterned and etched down to the oxide layer. The oxide layer is then wet oxide etched with the same lithographic pattern as the previous step. Any mechanical structures become fully released, forming the completed MEMS device. If desired, a 600 nm thick layer of gold with a 50 nm thick layer of chrome can be deposited on the device layer via shadow masking and electron-beam deposition to provide broadband reflectance. The finished wafer is then laser diced, sorted and shipped to the customer.

2.1.2. Material properties

The device layer resulting from the SOIMUMP’s process yields certain properties that are unique to the process and must be considered during MEMS design. Doping the device layer with phosphorus enhances its electrical conductivity but also causes an intrinsic stress. The electrical conductivity of heavily doped silicon and its dependence on device temperature was previously reported in [94]. It was also modelled and experimentally verified for the SOIMUMP’s process in [95], which showed that the thermal dependence of the electrical conductivity cannot be neglected during the design process. The intrinsic stress generated

Table 2-1: SOIMUMP’s device layer properties (doped [1 0 0] single crystal silicon).

Material property	Unit	Value	Reference
Electrical conductivity	S m^{-1}	24390 (at 300 K) 21276 (at 400 K) 18867 (at 500 K) 16129 (at 600 K) 14705 (at 700 K) 13400 (at 800 K)	[94]
Density	Kg m^{-3}	2330	[35]
Surface emissivity	-	0.6	[96]
Specific heat capacity	J K^{-1} kg^{-1}	700 (at 300 K) 755 (at 345 K) 789 (at 400 K) 831 (at 493 K) 856 (at 595 K) 856 (at 1600 K)	[95]
Thermal conductivity	W m^{-1} K^{-1}	150 (at 300 K) 111 (at 345 K) 100 (at 402 K) 73.4 (at 493 K) 59.0 (at 595 K) 42.3 (at 800 K) 32.1 (at 1000 K) 24.3 (at 1200 K) 23.0 (at 1413 K) 20.5 (at 1606 K)	[95]
CTE	K^{-1}	2.616×10^{-6} (at 300 K) 3.253×10^{-6} (at 400 K) 3.614×10^{-6} (at 500 K) 3.842×10^{-6} (at 600 K) 4.016×10^{-6} (at 700 K) 4.151×10^{-6} (at 800 K) 4.185×10^{-6} (at 900 K) 4.258×10^{-6} (at 1000 K)	[97]
Through-thickness stress gradient	MPa µm^{-1}	2.4 (for 10 µm thickness) 0.42 (for 25 µm thickness)	[39]
Residual stress	MPa	-3.9 (for 10 µm thickness) -1.9 (for 25 µm thickness)	[39]
Young's modulus	GPa	$E_x = E_y = 169$ GPa $E_z = 130$ GPa	[35]
Poisson ratio	-	$\nu_{yz} = 0.36$ $\nu_{zx} = 0.28$ $\nu_{xy} = 0.064$	[35]
Bulk modulus	GPa	$G_{yz} = G_{zx} = 79.6$ $G_{xy} = 50.9$	[35]

during doping consists of (a) a through-thickness stress gradient, and (b) an in-plane residual stress. An in-depth analysis of the intrinsic stress for SOIMUMP's using a series of test structures was reported in [39]. The intrinsic stress resulted in a residual curvature of the device surface which was measured to be $\kappa = 16.7\ \mathrm{m}^{-1}$ for a 10 µm thick device layer and $\kappa = 2.5\ \mathrm{m}^{-1}$ for a 25 µm thick device layer, where κ is the reciprocal of the radius of curvature. Similar results were achieved in studies where SOIMUMP's was used to fabricate MEMS cantilevers and mirrors at the CMP [43, 55]. In these cases, the curvature of the device surface was measured to be $\kappa = 14.2\ \mathrm{m}^{-1}$ for a 10 µm thick device layer and $\kappa = 2.2\ \mathrm{m}^{-1}$ for a 25 µm thick device layer. When adding the 600 µm thick gold coating, the difference in thermal expansion coefficients resulted in further stressing of the devices. This led to a surface curvature of approximately 60 m^{-1} for a 10 µm thick device reported in [55].

$$\begin{bmatrix}\sigma_1\\\sigma_2\\\sigma_3\\\sigma_4\\\sigma_5\\\sigma_6\end{bmatrix} = \begin{bmatrix}194.5 & 35.7 & 64.1 & 0 & 0 & 0\\ 35.7 & 194.5 & 64.1 & 0 & 0 & 0\\ 64.1 & 64.1 & 165.7 & 0 & 0 & 0\\ 0 & 0 & 0 & 79.6 & 0 & 0\\ 0 & 0 & 0 & 0 & 79.6 & 0\\ 0 & 0 & 0 & 0 & 0 & 50.9\end{bmatrix} \cdot \begin{bmatrix}\varepsilon_1\\\varepsilon_2\\\varepsilon_3\\\varepsilon_4\\\varepsilon_5\\\varepsilon_6\end{bmatrix} \qquad \text{(Equation 2-1)}$$

(In GPa)

An overview of the SOIMUMP's device layer properties is given in Table 2-1. Besides the process-specific material properties, the mechanical and thermal properties of single crystal silicon have been reviewed comprehensively in literature, e.g. [35, 37, 97]. It has a density of 2330 kg m^{-3} and the crystal structure is anisotropic with an elasticity matrix given in Equation 2-1 for a standard [1 0 0] wafer. An in-depth description of the elasticity matrix and how it relates to the growth axes can be found in [35]. The anisotropy is an important consideration during MEMS design because it has a significant impact on the device performance. The Young's modulus varies by over 20 % between axes, with a value of 169 GPa on the [1 1 0] axis and a value of 130 GPa on the [0 0 1] axis. These values were verified for the SOIMUMP's process in [36]. Further material properties that must be considered during MEMS design include the thermal conductivity, thermal expansion coefficient (CTE) and specific heat capacity, all of which are dependent on the device temperature.

2.2. MEMS mirror with electrothermal actuators

The design of the first MEMS mirror used in this work was based around the electrothermal actuator reported in [95]. The actuator could be tilted to a fixed angle or it could scan at its

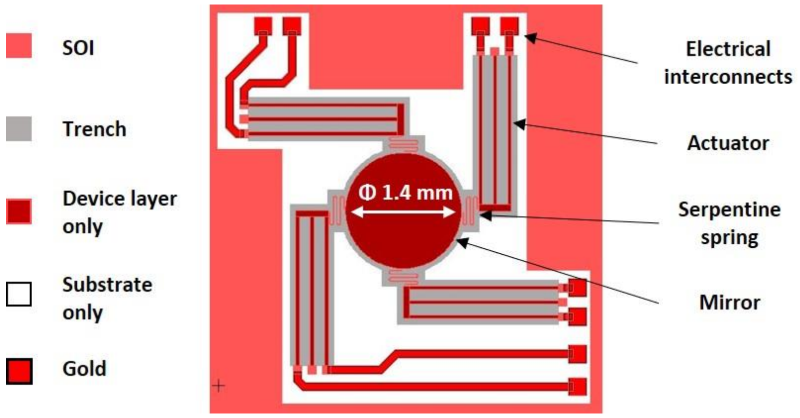

Figure 2-2: Top view design of the MEMS mirror with four electrothermal actuators radially connected to a circular mirror by serpentine springs.

mechanical resonance. The resulting movement of the actuator could then be used to tilt a mirror attached to the actuator. In later chapters, the fixed tilt angle of the mirror is used for laser wavelength tuning and the resonant scanning is used for laser Q-switching. The design of the MEMS mirror and its performance characteristics are given in the following subsections.

2.2.1. Mirror design

A schematic showing the top-view structure of the ET mirror chip is shown in Figure 2-2. The design consisted of four electrothermal actuators positioned radially around a circular mirror of 1.4 mm diameter. The device layer thickness was chosen to be 10 μm since this resulted in the largest displacement during actuation [95]. Each actuator consisted of three longitudinal beams with a width of 40 μm, a length of 1800 μm and a lateral centre-to-centre spacing of 175 μm. These beams were commonly connected at one end to a joint beam of length 390 μm & width 80 μm. At the opposite end, the beams were anchored separately to the substrate by end pads and connected to their respective electrical pathways. Each actuator, at the joint beam end, was connected to the mirror by a serpentine spring with a width of 8 μm and an outer turning radius of 25 μm. The mirror, actuators and serpentine springs were fully released from the substrate, as indicated by the trench area (grey) in Figure 2-2.

Operation of an actuator was achieved by inducing a current flow through the outermost longitudinal beams by applying an electrical potential difference across them. The temperature of said beams then rose through Joule heating, and thermal expansion occurred.

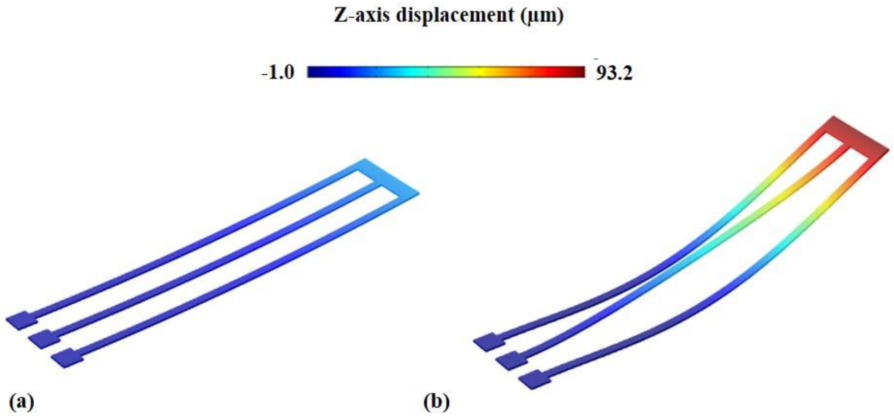

Figure 2-3: FEM simulations showing the electrothermal actuator with (a) no actuation, and (b) 7 V applied to the outermost longitudinal beams. A scaling factor of 5x was used to exaggerate the visual displacement.

The central longitudinal beam had no current flow and was therefore colder than the other beams. The central beam therefore functioned as a mechanical constraint. The stress induced by thermal expansion and the mechanical constraint caused the outermost beams to buckle and the actuator was displaced in the upward direction. The upwards displacement of the actuator then resulted in tilting of the circular mirror. The radial positioning of four actuators enabled 2D control of the mirror tilt angle in both directions from the mirror resting position.

An illustration of the actuator movement for an applied potential difference of 7 V is given in Figure 2-3, which was taken from a finite element model (FEM) of the device. A scaling factor of 5x was used to exaggerate the visual displacement of the device, while the colour scale indicates the actual displacement. The FEM is discussed in more detail in the following subsections.

2.2.2. Fabricated device

The designed MEMS mirror was fabricated using SOIMUMP’s and a scanning electron microscope image of the fabricated device is shown in Figure 2-4. To make the mirror compatible for use within a solid-state laser, a high-reflectance optical coating was required. A multi-layer dielectric coating was desired but was unable to be implemented without hindering the performance of the device. A thin layer of gold was therefore considered instead to give a reflectance of 96 % in the near infrared. The gold coating from SOIMUMP’s was not used for this device because the coating thickness was inflexible and would result in a highly stressed structure. The resulting surface curvature of the device was

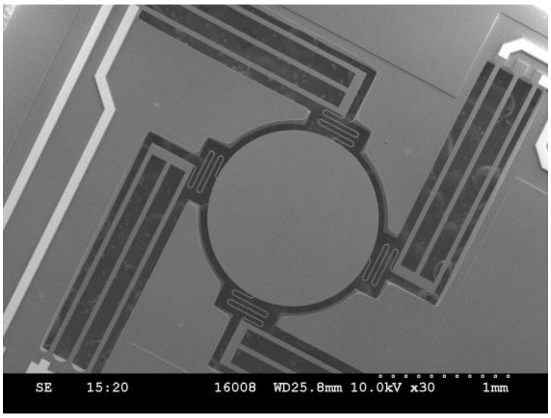

Figure 2-4: Scanning electron microscope image of the fabricated ET mirror.

then not practical for use in solid-state laser systems. Instead, a thin layer of gold with a target thickness of 200 nm was deposited on the mirror surface using thermal evaporation. This was done by John Mackersie at the University of Strathclyde. The die was mounted on a microscopy slide using Kapton tape for this process. A 3D-printed mask was placed over the die to ensure that gold was deposited only on the mirror surface. This prevented short circuits on the electrical pathways and ensured that the coating did not interfere with the performance of the actuators.

The mirror surface curvature was measured using a Veeco NT1100 white light interferometer with 5x magnification before and after the deposition of the gold coating. The curvature before coating deposition was measured to be 13.3 m^{-1} with a spherical concave profile. After coating deposition, the curvature was measured to be parabolic concave with a value of 20.0 m^{-1} near the centre of the mirror. The reflectance of the mirror was measured by directing the output beam of a Nd: YAG laser onto the mirror surface and measuring the optical power of the beam before and after reflection by the mirror. The mirror reflectance was measured to be 96 % using a Thorlabs S314C power meter.

2.2.3. Finite element model

To demonstrate the actuation concept of the MEMS mirror and predict its performance characteristics, a FEM was built using the commercial software package COMSOL Multiphysics (version 4.2a). The software modules for MEMS and heat transfer were used to simulate the structural mechanics and the thermal performance of the device. The inputs to the model included the device geometry, the material properties, the boundary conditions and the meshing conditions. The software then compiled the respective equations using an

Table 2-2: Material properties of gold [95].

Material property	Unit	Value
Electrical conductivity	S m^{-1}	4.5×10^{7}
Density	Kg m^{-3}	19300
Surface emissivity	-	0.02
Specific heat capacity	J K^{-1} kg^{-1}	129
Thermal conductivity	W m^{-1} K^{-1}	317
CTE	K^{-1}	14.2×10^{-6}
Young's modulus	GPa	70.9
Poisson ratio	-	0.44
Thermal stress	MPa	147

iterative solution defined by the finite element method. Results that could be extracted from the model include the temperature distribution, the current density and the z-axis displacement (among many others).

Model construction

The first step in the construction of the model was to define the geometry of the device. The modelled geometry included only the MEMS mirror device (actuators, mirror and gold coating). The second step was then to input the material properties of the silicon actuators, the silicon mirror and the gold coating. The anisotropic material properties of single crystal silicon given in Table 2-1 were used for the actuators and the mirror, with the temperature-dependent material properties set using piecewise cubic functions defined by the software. The material properties of the gold coating were modelled with the isotropic material properties given in Table 2-2.

The third step of the model construction was to define the boundary conditions of the model. The first boundary condition was the intrinsic stress of the device layer that resulted from the doping process. This was modelled as a through-thickness stress gradient using the same technique reported in [65], where the condition was input as an ‘initial stress’. The second boundary condition involved deposition of the gold coating. The coating was deposited at an elevated temperature and then cooled to room temperature after the process finished. The different thermal expansion rates of silicon and gold then resulted in stress-induced curvature of the mirror surface. This thermal stress was calculated to be 147 MPa using the Stoney equation for a thin metallic layer deposited on a substrate [98]. The thermal stress was then defined as an ‘initial stress’ within the gold layer.

A boundary condition was then set for the anchoring of the actuators. The end pads of the actuators were anchored to the substrate in the fabricated device and were therefore fixed in position. This was defined in the model by fixing the displacement of the end-faces of the actuators to 0. The end-faces of the actuators were also fixed in temperature at a value of 293 K to factor in the effects of the insulating oxide layer between the device layer and the substrate. Heat transfer through conduction was inherently calculated by the finite element solution, whilst convection to the surrounding air was defined using a heat transfer coefficient of 250 W m^{-2} K^{-1} [95]. The final boundary condition was to apply an electrical potential difference across one of the actuators. A voltage was defined at the end-face of one of the outermost longitudinal actuator beams, while the opposite longitudinal beam on the same actuator was grounded. All other surfaces were electrically insulated to external influences.

The final step of the model construction was to generate a mesh, i.e. creating small geometrical cells (elements) to accurately model the device geometry. The cells must be small enough to form a realistic representation of the real-world device, but large enough that the computing power required to compute the FEM calculations is not excessive. Three quadrilateral face meshes were created: one for the circular mirror and the coating, one for the actuator beams and one for the serpentine springs. Each face mesh was swept through the material thickness to give two layers, resulting in a total of 3754 elements. The mesh used in this work was optimized by varying the mesh density until the results of the simulation differed by less than 1 % for a change in the number of layers.

Results

The FEM was split into two parts: a modal analysis and a stationary analysis. The modal analysis was used to compute the eigenfrequencies of the mirror structure. The mechanical resonance of the device could therefore be predicted, and the dynamic mode shapes could be analysed. The stationary analysis was used to apply a steady-state electrical signal to an actuator. The FEM would then solve the resulting temperature distribution and couple it to a static mechanical deformation.

The modal analysis model computed the first six eigenfrequencies of the ET mirror. The two eigenfrequencies of interest occurred at f_{res} = 1976 Hz and 1977 Hz and are shown in Figure 2-5. The mode shapes occurred on orthogonal axes since the structure contained actuators on

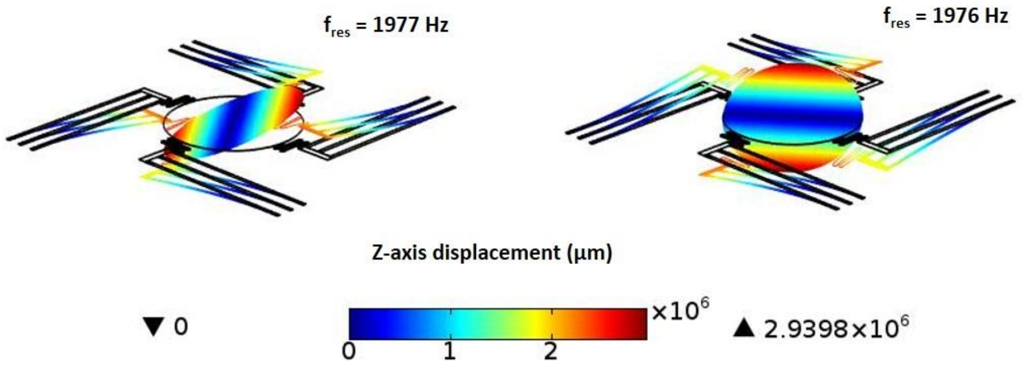

Figure 2-5: Image taken from a FEM showing the eigenfrequency modes of the ET mirror.

orthogonal axes. It is important to note that other eigenfrequencies of the device resulted in other movement modes that could hinder the performance of the device. These are considered parasitic and enough spacing between the frequencies of these modes and the modes of interest are required to prevent mode coupling. For this device, no parasitic modes occurred within 800 Hz of the modes of interest. It was expected that no coupling would occur with such a large separation.

For the stationary analysis, a parametric sweep of the potential difference was applied across the terminals of one actuator ranging from 0 V to 15 V in steps of 3 V. A maximum of 15 V was chosen because this was the voltage at which previous experiments by other members of the CMP resulted in the actuator glowing, indicating that its temperature had risen above 525 °C. It was estimated that the device temperature was in the range of 700 °C – 900 °C because of the colour of the incandescence. This could therefore be used as a sanity check for the simulation. The devices were never heated beyond this temperature to prevent damage or performance degradation. Some sample results from the simulation are shown in Figure 2-6.

With 0 V applied to the actuators, the mirror tilt angle was simulated to be 0° and the temperature of the device was uniform at room temperature. Increasing the voltage across one actuator resulted in a temperature gradient along the longitudinal beams and tilting of the mirror. At a voltage of 15 V, the maximum temperature of the device was simulated to be 1198 K (925 °C) at the buckling point of the outermost actuator beams. The simulated temperature at a voltage of 15 V was slightly higher than the predicted range of 700 – 900 °C. The most probable reason for the overestimation of temperature is a discrepancy in the boundary conditions for heat transfer. The temperature of the actuator beams at their connection to the end pads was fixed at room temperature in the simulation. It was observed

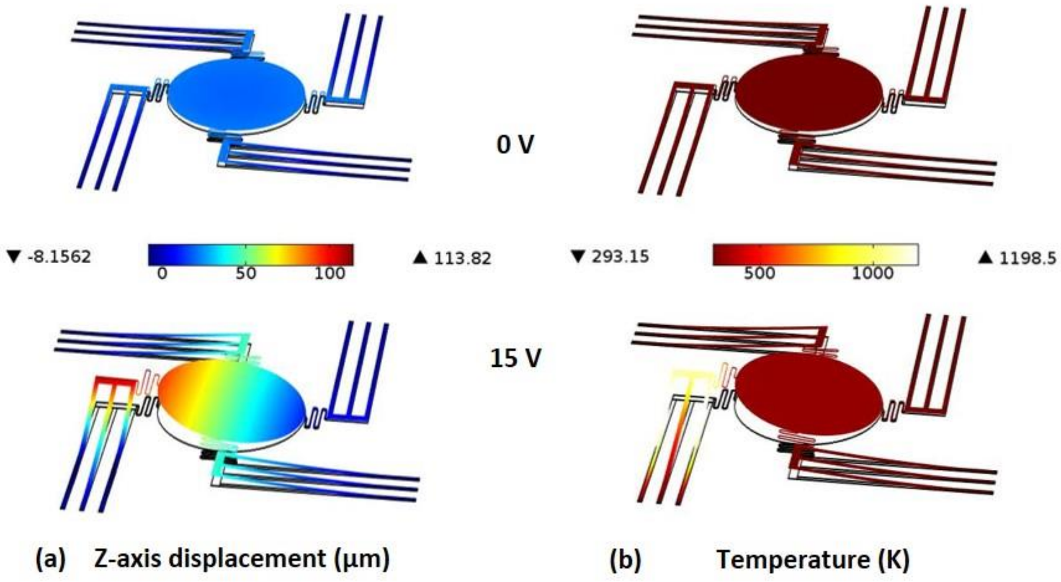

Figure 2-6: Images from FEM simulations with 0 V and 15 V applied to one actuator, showing (a) the z-axis displacement and (b) the temperature distribution of the device. A scaling factor of 2.6 was used on the visual effects.

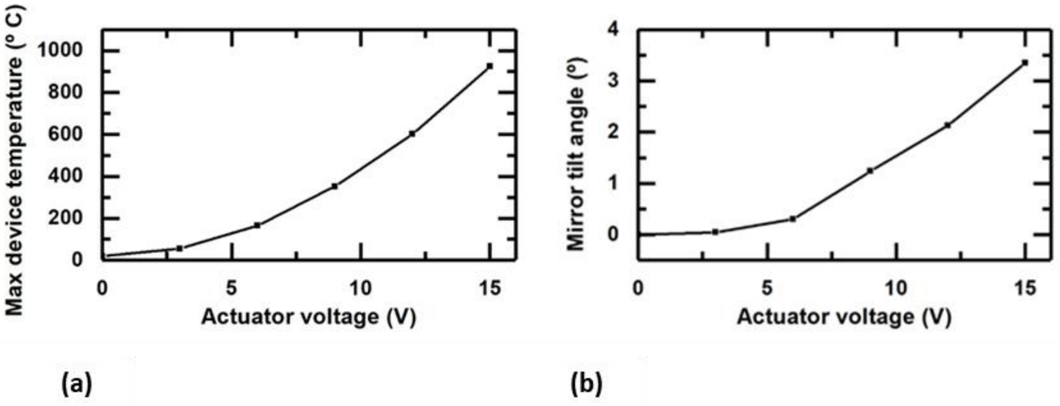

Figure 2-7: Plots of (a) the maximum simulated device temperature against actuator voltage and (b) the simulated mirror tilt angle against actuator voltage.

from thermal images of the ET mirror that these areas of the device experienced an increase in temperature when the device was under actuation. There was in fact also an unexpected rise in the temperature of the substrate layer. Attempts were made to include the substrate in the FEM model, but limits on the computational power were encountered with the required meshing. Future work to include this in the model could bring more accurate simulation results.

A plot of the maximum simulated device temperature against actuator voltage is shown in Figure 2-7a. A nonlinear rise in temperature was observed as the actuator voltage was increased, occurring because of the temperature dependent material properties of the device layer. The simulated mirror tilt angle was calculated from the Z-axis displacement at opposite edges of the circular mirror. A plot of the calculated mirror tilt is shown in Figure 2-7b, highlighting an increase from 0° to 3.3° as the actuator voltage was increased from 0 V to 15 V. The simulated response showed a nonlinear rise in mirror tilt angle up to an actuator voltage of ~ 6 V, with higher voltages showing a linear rise.

2.2.4. Experimental evaluation

To evaluate the performance of the fabricated ET mirror, the die was mounted onto a custom-made printed circuit board (PCB) using double sided tape. The electrical interconnects for each actuator were created through wire bonding using 25 μm thick aluminium wire. Leads were soldered to the PCB to allow easy access for crocodile clip connectors. The leads could then be connected to an Agilent 33250A signal generator. The maximum signal amplitude that the signal generator could output was 10 V. This was the maximum voltage that was applied to the actuators since only small static tilt angles (<< 1°) were required for the wavelength tuning of the lasers reported in later chapters.

Static mirror tilt

The signal generator was connected to only one actuator at a time to evaluate the static tilt performance of each individual ET actuator. The beam from a HeNe laser was directed towards the centre of the mirror and reflected onto a screen orientated perpendicularly to the direction of the beam at 1.9 m from the ET mirror. With no actuation, the centre of the reflected beam was marked on the screen to provide a reference point. The optical tilt angle of the mirror could then be calculated by measuring the beam displacement on the screen and using trigonometry. The mechanical tilt angle of the mirror, as calculated in the FEM simulations, was half of the optical tilt angle. The minimum change in displacement of the beam that could be reliably measured was 1 mm, corresponding to a mechanical tilt angle of 0.015°.

Voltages from 0 V to 10 V in steps of 1 V were applied to each actuator in turn, labelled A1 to A4 in Figure 2-8a. Figure 2-8b shows a plot of the measured mechanical tilt angle of the mirror against actuator voltage. No measurable change in tilt angle was observed below an actuator voltage of 3 V. Thermal expansion until this point was not enough to cause a

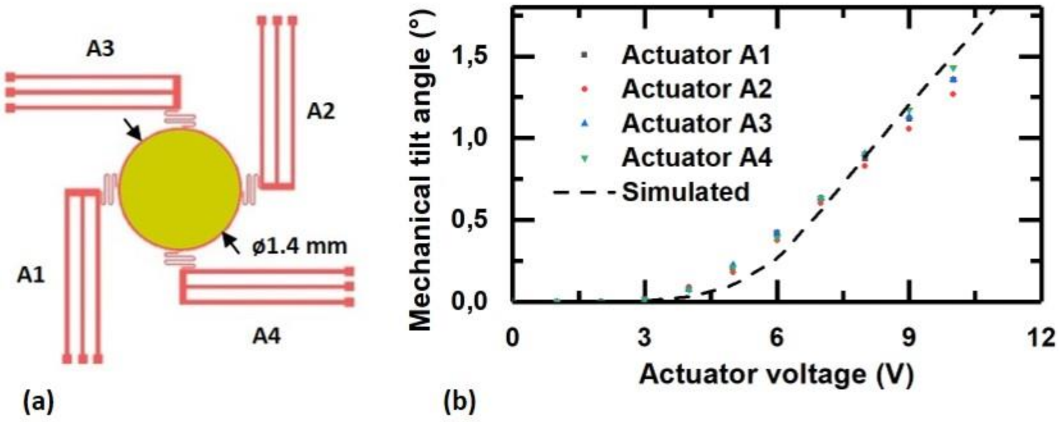

Figure 2-8: (a) Schematic of the ET mirror design with labelled actuators A1-A4. (b) Plot of the mechanical mirror tilt angle against actuator voltage for each actuator.

measurable out-of-plane movement of the mirror. At an actuator voltage of 3 V, the mechanical tilt angle of the mirror was measured to be 0.015° for all actuators. A nonlinear rise in tilt angle was then observed until an actuator voltage of 5 V, corresponding to a mechanical tilt angle of 0.20 ± 0.025°. A linear rise in tilt angle was then observed for actuator voltages from 5 V up to 10 V, where the mechanical tilt angle was measured to be 1.33 ± 0.08°. The direction of the mirror tilt was different for every actuator. Displacement of an actuator was always upward on the out-of-plane axis (z-axis) for an increase in actuator voltage. The radial positioning of the actuators at 0°, 90°, 180° and 270° then enabled mirror tilt on orthogonal axes in both directions from the mirror resting position.

The measured mirror tilt angle showed in Figure 2-8b was compared to the results of the FEM simulation; this time ran from 0 V to 10 V in steps of 1 V. The simulation showed similar results to the experimental analysis with no measurable change in tilt angle occurring below an actuator voltage of 3 V. A nonlinear rise in tilt angle was then observed between actuator voltages of 3 V and 6 V, followed by a linear rise until 10 V. The simulated mechanical tilt angle of the mirror was 0.26° at 6 V and 1.51° at 10 V. The results of the simulation matched the experimental results very well on average. However, in the nonlinear region (3 V to 6 V in Figure 2-8b), the rise rate of the tilt angle against actuator voltage was simulated to be slower than that of the measured results. Contrarily, the slope of the linear region (6 V to 10 V) was simulated to be larger. Possible inaccuracies in the model arise from the dimensional tolerances of the device and the boundary conditions for heat transfer. Nevertheless, the simulation gave a good indication of the device performance.

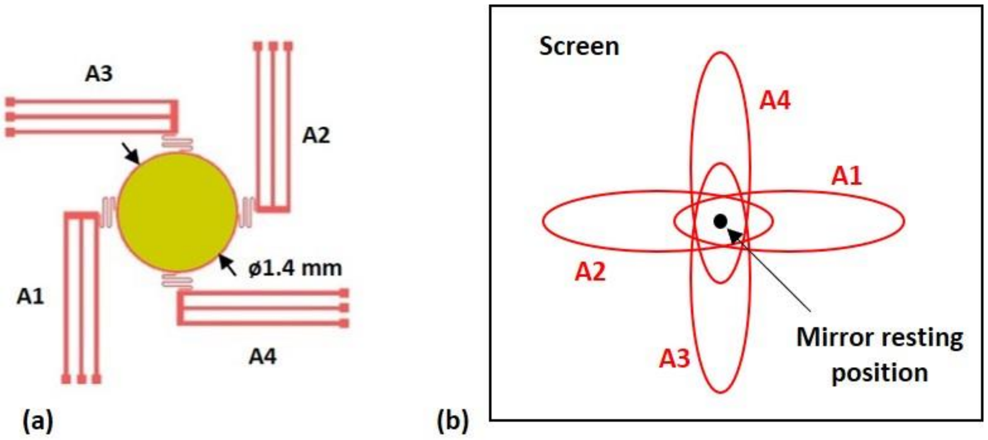

Figure 2-9: (a) Schematic of the ET mirror design with labelled actuators A1-A4. (b) Illustration of the scan line, as observed on a screen, for each actuator operated individually with a signal amplitude of 10 V and a signal frequency of 2050 Hz.

Resonant scanning

The output signal from the Agilent signal generator was modified to a square-wave signal to analyse the mechanical resonance of the ET mirror. A square-wave signal was used because it resulted in the largest possible scan angle of the mirror. This resulted from maximizing the force induced on the mirror by ensuring the fastest rise/fall of the device temperature. The signal had a duty cycle of 50% and an offset equal to half of the signal amplitude. Again, the maximum amplitude that the signal generator could output was 10 V. A similar measurement setup to that used for the static tilt analysis of the mirror was used for this analysis, but with 113 mm between the screen and the mirror. Again, only one actuator was used at a time.

The scanning movement of the mirror resulted in a scan line being observed on the screen as the HeNe beam was deflected over time. The dimensions of the scan line then defined the TOSA of the ET mirror through trigonometry. A nonlinear scanning movement of the mirror was detected because the scan line on the screen was elliptical in shape. This indicated that there was coupling between the resonant axes of the device. An illustration of the scan line as observed on the screen is shown in Figure 2-9 for each actuator and is compared to the mirror resting position. None of the scan lines intersected the mirror resting position and an offset was observed between the centre of the elliptical scan lines and the mirror resting position.

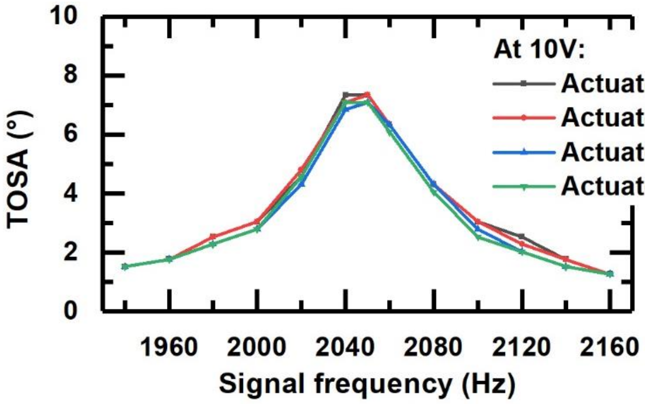

Figure 2-10: Plot of the measured mirror TOSA on the major axis against signal frequency for each actuator at a constant signal amplitude of 10 V.

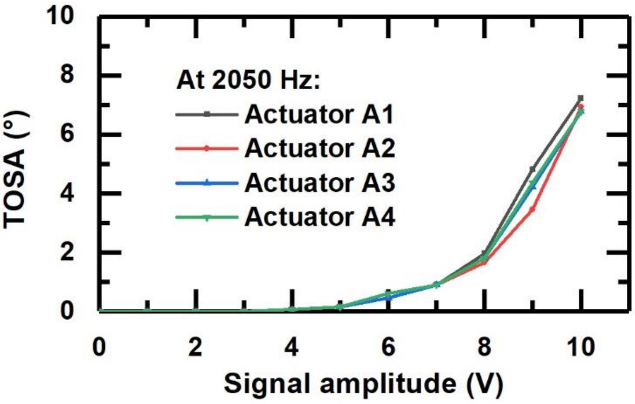

Figure 2-11: Plot of the measured mirror TOSA against actuator signal voltage for each actuator at a constant signal frequency of 2050 Hz.

At the maximum signal amplitude of 10 V, the peak resonance was identified at 2050 ± 5 Hz for all four actuators. This resulted in an offset of 3.7% (74 Hz) between the experimental and simulated results. This was a good match where discrepancy could be explained through the dimensional tolerances of the device defined by the foundry. For example, the tolerance on the thickness of the device layer is quoted as 10 ± 1 µm. The impact that this tolerance had on the mechanical resonance was simulated to be ± 9.3% (186 Hz). The simulated eigenfrequencies were therefore within the tolerance limits, indicating that the results of the simulation were accurate.

To compare the performance of each actuator, the TOSA on the major axis of each ellipse was measured. This was first done at different signal frequencies with a constant signal amplitude of 10 V. A plot of the measured TOSA against signal frequency is shown in Figure 2-10. The peak TOSA was measured to be 7.1 ± 0.3° at the peak resonance of

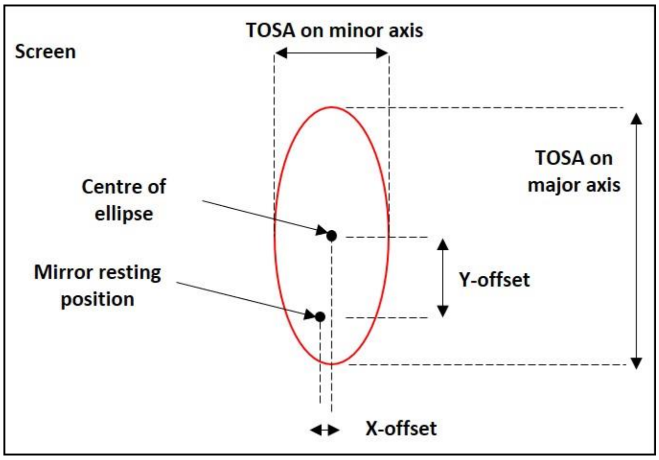

Figure 2-12: Illustration of the scan line as seen on the screen when actuator A4 was driven, showing the comparison of the elliptical profile to the mirror resting position.

2050 Hz. The TOSA then dropped off on either side of the peak with a 1/e bandwidth of 50 Hz for all actuators, limited by air and structural damping. The signal frequency was then held constant at 2050 Hz and the signal amplitude was varied. The measured TOSA against signal amplitude is shown in Figure 2-11. The measured TOSA dropped from 7.1° at 10 V to a minimum of 0.06° at 4 V. A minimum signal amplitude of 4 V was required to activate the mechanical resonance of the mirror.

Actuator A4 was chosen to further analyse the nonlinear scan profile of the mirror since each actuator gave similar results in their respective scanning directions. The offset between the elliptical scan line and the mirror resting position was analysed according to Figure 2-12. Actuator A4 was used with a signal frequency of 2.06 kHz in the lasers described in later chapters. This signal frequency was chosen to enable simpler alignment of the lasers and is fully discussed in later chapters. The following characterization therefore maintained a constant signal frequency of 2.06 kHz.

The distance between the ET mirror and the screen was fixed at 610 mm. The signal amplitude was varied from 10 V to 6 V in steps of 1 V. Plots of the resulting data are shown in Figure 2-13. The TOSA on the major axis of the ellipse decreased nonlinearly from 6.3° at 10 V to 0.6° at 6 V. The TOSA on the minor axis of the ellipse was measured to be 0.4° at 10 V and 0.05° at 9 V. Below 9 V the TOSA on the minor axis became so small that it could not be measured (the ellipticity of the scan line increased to form a vertical line). The Y-

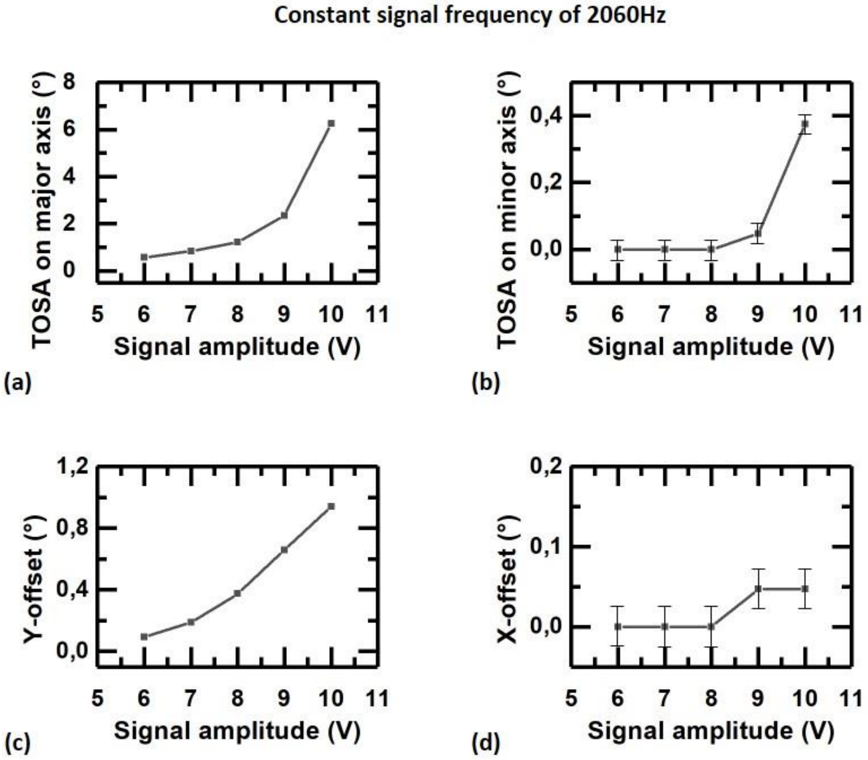

Figure 2-13: Plots of (a) the TOSA on the major axis, (b) the TOSA on the minor axis, (c) the Y-offset and (d) the X-offset of the elliptical scan profile for the ET mirror as defined by Figure 2-12.

offset between the centre of the ellipse and the mirror resting position was measured to be 0.9° at 10 V and decreased nonlinearly to 0.1° at 6 V. The x-offset between the centre of the ellipse and the mirror resting position was measured to be 0.05° at 10 V and 9 V. Below 9 V the x-offset became so small that it could not be measured, hence the sudden jump to 0°.

As observed in the above results, the scanning movement was not centred around the mirror resting position. The offset on the Y-axis occurred because the average temperature of the actuator during one movement cycle was elevated above room temperature. A theoretical model of the actuator temperature while scanning at its mechanical resonance was reported in [95]. The reason for the offset on the X-axis is not fully understood at this time, although potential causes could be inhomogeneity in the thickness of the gold coating and the nonlinear response of the mirror.

2.2.5. Discussion

The nonlinear scanning movement observed in the resonant response of the ET mirror could be greatly reduced by an improved mirror design. The same conceptual design with actuators of different dimensions on orthogonal axes would reduce the coupling between the axes because the mechanical resonance is dependent on said dimensions. Such mirrors have been designed by other members of the CMP for other projects, but unfortunately in the time available for this work there were no functional devices available. As an example, a mirror with a diameter of 2 mm was fabricated where the actuators on the x-axis had beams with a length of 2 mm and the actuators on the y-axis had a length of 1.6 mm. The peak resonance on the x-axis was measured to be 1.2 kHz while on the y-axis it was measured to be 1.52 kHz. No measurable coupling was observed between the resonant axes.

The characterization of the ET mirror in this section was focused towards use in the lasers described in later chapters. The static tilt of one actuator at a time was used for the tunable laser described in Chapter 4. The resonant tilt of one actuator was used for creating pulsed operation of the lasers as described in Chapters 3 and 5. The mirror is also capable of other movement capabilities including 2D tilt control with static tilt of multiple actuators, static tilt combined with resonant scanning, and raster scanning. The case of static tilt combined with resonant scanning is investigated briefly in Chapters 3 and 5 with a focus on its application for those specific lasers. The other movement modes were not characterized because they were not within the scope of this thesis.

2.3. MEMS mirror array with electrostatic actuators

The MEMS mirrors with electrostatic (ES) actuators that were used for this thesis were similar to those reported in [65]. The only differences were small changes in the dimensions of the circular mirror and the torsion beams to analyse the stability of the mirror movement at higher frequencies. Since this type of mirror has already been characterized, a brief overview of the mirror performance is given in this section.

2.3.1. Mirror design

A compact array of four ES mirrors was designed where each device included a circular mirror supported on either side by a rectangular torsion beam, with a one-sided comb-drive

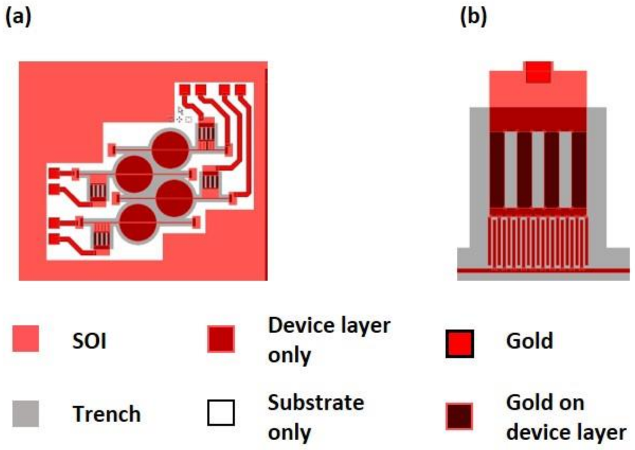

Figure 2-14: (a) Top view design of the MEMS mirror array with electrostatic comb-drive actuators. (b) Zoomed view of the electrostatic comb-drive actuator.

present on one of the torsion beams. A top-view schematic of the chip design is shown in Figure 2-14a. Every mirror had an identical comb-drive actuator, shown in Figure 2-14b. The mirrors had a circular mirror diameter of 750 µm and torsion beams with a length of 725 µm. The width of the torsion beams was different for each of the four mirrors, ranging in 1 µm steps from 14 µm for the uppermost mirror to 17 µm for the lowermost mirror. The device layer thickness was chosen to be 25 µm because this resulted in a flatter mirror surface than a 10 µm thick device layer.

The comb-drive consisted of 21 interleaving combs and a bimorph structure on the fixed comb-drive side (gold on silicon). 11 of the interleaving combs were connected to the fixed bimorph structure, while the other 10 were connected to the movable torsion beam. The combs had a length of 160 µm, a width of 10 µm and a centre-to-centre spacing of 16 µm, leading to an airgap of 6 µm between adjacent combs. The purpose of the bimorph structure was to elevate the fixed combs, resulting in an initial offset between them and the moving combs. An in-depth analysis of the bimorph structure and its role in improving device performance for the used mirror design family was reported in [43].

2.3.2. Finite element model

The FEM for the ES mirror was built using the MEMS module of COMSOL Multiphysics. A modal analysis was used to identify the first six eigenfrequencies of the MEMS mirrors. The material properties for single crystal silicon given in Table 2-1 were used again as model inputs. A linear elastic material model was used with anisotropic material properties and a

Table 2-3: Results of the FEM for the ES mirror.

Width of torsion beam	Mechanical resonance
14 µm	9106 Hz
15 µm	9898 Hz
16 µm	10640 Hz
17 µm	11432 Hz

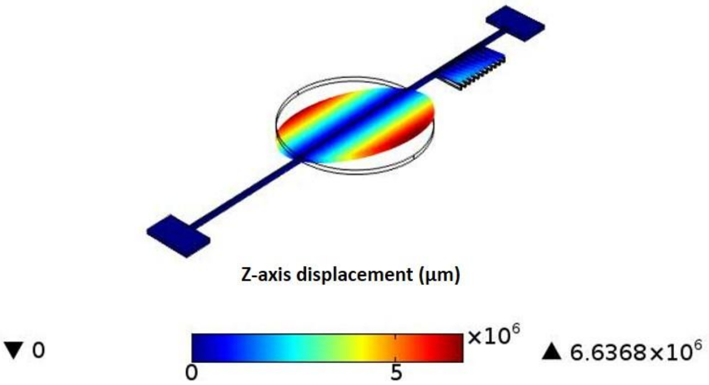

Figure 2-15: Image taken from a FEM showing the movement mode of the ES mirror.

condition that the lower side of each end pad was fixed. A tetrahedral mesh was used with a minimum element size of 0.389 µm and a total number of 18280 elements. This mesh was a default mesh in COMSOL, and optimization was done by changing the default mesh densities until the difference in the results was less than 1%. A parametric solver was set up to vary the width of the torsion beam from 14 µm to 17 µm in steps of 1 µm.

From the results of the simulation, only one movement mode was of interest because it was the only one which allowed free movement of the combs and tilted the circular mirror. The remaining five modes were considered parasitic since they resulted in in-plane movement of the combs, which would cause the moving combs and the fixed combs to become locked together. An image of the movement mode of interest is shown in Figure 2-15 and the corresponding mechanical resonance for each mirror geometry is given in Table 2-3. For a torsion beam width of 14 µm, the mechanical resonance of the mirror was simulated to occur at a frequency of 9106 Hz (f_{res}). The frequency then increased to 9898 Hz at 15 µm, 10640 Hz at 16 µm, and 11432 Hz at 17 µm. The separation between the mode of interest and the parasitic modes was simulated to be more than 1.4 kHz for all the mirror geometries. Mode coupling was therefore expected to be negligible.

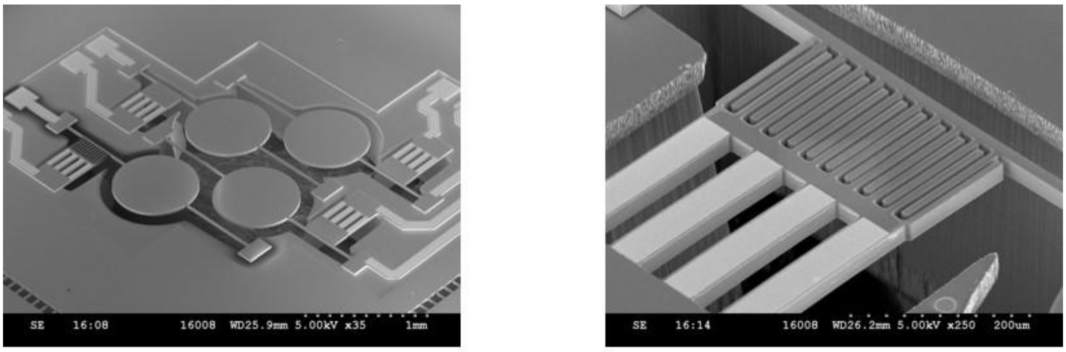

(a) (b)

Figure 2-16: SEM images showing (a) the fabricated array of ES mirrors and (b) a close-up of the comb-drive.

2.3.3. Experimental results

Fabrication and coating

The ES mirrors were fabricated using SOIMUMP's and SEM images of the devices are shown in Figure 2-16. To make the mirrors compatible with use within a solid-state laser, a multi-layer dielectric coating was ideally required. This was developed in collaboration with Helia Photonics Ltd who deposited 13 layer-pairs of SiO_2 / Nb_2O_5 with ¼ λ thickness to achieve a theoretical reflectance of > 99 % at λ = 1064 nm. This was done via ion-beam sputtering, with the MEMS die mounted on a microscopy slide using Kapton tape (which also masked the bond pads).

The average ROC of the mirrors before coating was measured to be 0.44 m using a Veeco NT1100 white light interferometer with 10x magnification. After coating, the average ROC was measured to be 60 mm convex. This indicated that the coating process induced large stresses on the mirror structure. The reflectance of the optical coating was measured by directing the output beam from a 2-mirror Nd: YAG laser towards one of the mirrors. The optical power of the beam before and after reflection by the mirror was then measured using a Gentec XLP12-3S laser power detector. The reflectance at λ = 1064 nm was measured to be 98 %, which was less than the theoretical reflectance of the coating. This was expected to be a result of shadowing from the Kapton tape used to mask the bond pads during the coating process.

Mechanical resonance

To analyse the mechanical resonance of the ES mirrors, the die was mounted onto a custom-made PCB using double-sided tape. The electrical interconnects were made via wire bonding with 25 µm thick aluminium wire. Electrical wires were then soldered to the PCB to allow easy access to crocodile clip connectors. Each mirror could then be connected separately to an Agilent 33250A signal generator via a 20x voltage amplifier. A 10 kΩ resistor was used between the mirror and the signal generator to prevent damage in the case of a short circuit between the combs. The maximum signal amplitude that could be supplied to the mirrors was 200 V. The signal generator was configured to output a square-wave signal with a duty cycle of 50% and an offset equal to half of the signal amplitude. A square-wave signal was chosen to maximize the force induced on the mirror. Each mirror was analysed in turn, with only one mirror being actuated at a time. A HeNe laser was directed towards the mirror being actuated and reflected onto a screen to detect the mirror movement.

In the case of the mirrors with 14 µm and 15 µm wide torsion beams, no movement could be induced. It was thought that the optical coating influenced the frequency response of the mirror, perhaps leading to mode coupling involving the parasitic movement modes. The remaining two mirrors could be resonantly excited. The peak mechanical resonance of the mirror with 16 µm wide beams was identified at $f_{res} = 10.06$ kHz, with a corresponding TOSA of 5.9° at a signal amplitude of 200 V. In the case of the mirror with 17 µm wide beams, the peak mechanical resonance was identified at $f_{res} = 10.685$ kHz, with a corresponding TOSA of 4.8° at a signal amplitude of 200 V.

The measured peak mechanical resonance of the coated ES mirrors was measured to be ~ 6 % lower than the results of the FEM simulation for the bare silicon mirrors. This was a result of two factors: the deposition of the dielectric coating and the fabrication tolerances defined by the foundry. The die on which the ES mirrors characterized in this chapter was based was not tested before coating and thus a direct comparison could not be made. However, other dies were tested without an optical coating and were measured to yield a peak mechanical resonance ~ 3% lower than the simulated results. This was verified to be within the fabrication tolerances of ± 1 µm for the thickness of the device layer. It was also observed that all four mirrors on the uncoated chip operated correctly, indicating that the optical coating had a detrimental impact on the performance of some of the ES mirrors.

The ES mirrors could be excited at their mechanical resonance, f_{res}, or at the second harmonic frequency of their mechanical resonance, f_{2x}. This occurred because the force induced on the structure was not dependent on which direction the fixed combs were

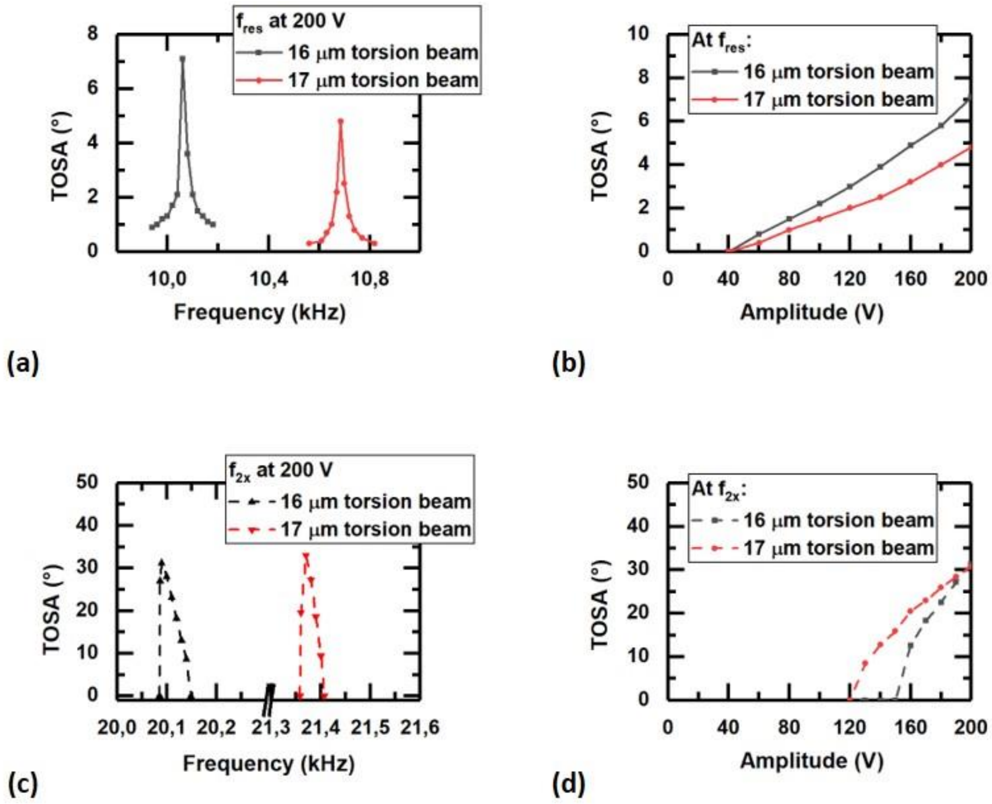

Figure 2-17: Plots showing the TOSA of the ES mirrors for different actuation conditions: (a) TOSA vs signal frequency with a signal amplitude of 200 V for the case of f_{res}, (b) TOSA vs signal amplitude when driven at f_{res}, (c) TOSA vs signal frequency with a signal amplitude of 200 V for the case of f_{2x}, (d) TOSA vs signal amplitude when driven at f_{2x}.

displaced from the moving combs. Therefore, since the mirror crossed the resting position twice per movement cycle, a driving signal of twice the resonant frequency would also induce movement. This was investigated for similar mirrors in [65] and was observed to produce a larger TOSA due to maximizing the mirror torque. When driven at f_{res}, the frequency response of the mirrors was linear. However, when driven at f_{2x}, the frequency response was nonlinear and hysteretic. This was caused by nonlinearities in the electrostatic excitation of the mirrors and their mechanical properties. A full discussion of the nonlinear effects was reported in [65].

Driving the mirror at f_{res} and f_{2x} was analysed for different signal frequencies and amplitudes, and the results are shown in Figure 2-17. The frequency response of the coated mirrors when driven at their mechanical resonance, f_{res}, with a signal amplitude of 200 V is shown in Figure 2-17a. A symmetrical response was observed with a 1/e drop-off of 80 Hz for the

TOSA of both functional mirrors. The TOSA of the mirrors was also dependent on the amplitude of the driving signal, as shown in Figure 2-17b. In the case of the mirror with 16 µm wide torsion beams, the TOSA dropped linearly from 5.9 ° to 0.9 ° when the signal amplitude was reduced from 200 V to 50 V. For the same conditions, the TOSA of the mirror with 17 µm wide torsion beams dropped from 4.8° to 0.3°. For both mirrors, a signal amplitude of more than 40 V was required to achieve a scanning movement using this driving scheme.

When driven at f_{2x}, the peak mechanical resonance was measured to be 20.09 kHz and 21.37 kHz for the mirrors with 16 µm and 17 µm wide torsion beams respectively. The resulting mirror TOSA's were respectively 31.3° and 33.0°, as shown in Figure 2-17c. A steep drop-off was measured on the lower tail of the frequency response for both mirrors and hysteresis was also observed. This was consistent with the results reported in [65]. When driven at f_{2x}, the response of the TOSA to signal amplitude was also nonlinear, as shown in Figure 2-17d. A signal amplitude of 160 V was required to activate the resonance of the mirror with 16 µm wide torsion beams, resulting in a TOSA of 12.5 °. For the mirror with 17 µm wide torsion beams, a signal amplitude of 130 V was required which resulted in a TOSA of 9.0 °.

2.3.4. Discussion

As a result of the deposition of a multi-layer dielectric coating, the curvature of the ES mirror changed from 2.3 m^{-1} concave to 16.7 m^{-1} convex. This occurred because coating deposition occurred at an elevated temperature. The return to room temperature then resulted in the multi-layer structure being stressed due to the difference in the thermal expansion coefficients of the layers. The resulting mirror curvature was not ideal for use in solid-state lasers and must be improved in future work. The measured reflectance of the coating (98 %) was also lower than the theoretical reflectance (> 99.5 %). The root cause for this effect is unknown but could be a result of masking the bond pads during the coating process. Masking of the bond pads was needed to prevent the optical coating from being deposited on them, making it possible to create the electrical interconnects. The masking may have resulted in an uneven distribution of the coating layers, although this could not be measured.

The ES mirror was used as the Q-switch in the laser described later in Chapter 3. For this laser, the convex curvature of the ES mirror was worked around by adjusting the resonator design. The development of an HR optical coating with a flat surface and a curvature that does not change with temperature would simplify the design of such lasers and optimize their performance. The impact of the coating on this particular laser is fully discussed in Chapter 3.

2.4. Summary

Two types of MEMS mirror have been designed and fabricated for use within the solid-state laser systems described in later chapters. A mirror with electrothermal actuators which could scan at its mechanical resonance or be tilted to a fixed angle was reported. The mirror tilt was made possible on two axes and in both directions from the mirror rest position by the radial positioning of the actuators. The peak mechanical resonance was measured at 2.05 kHz and showed a nonlinear (elliptical) movement profile with a peak TOSA of 7.1 ° at a signal amplitude of 10 V. The mirror could also be tilted to a fixed angle of up to 1.33 ° by applying a DC voltage of 10 V to an actuator. An array of dielectric-coated mirrors with electrostatic comb-drive actuators was also characterized. Two mirrors with respective peak resonances at 10.06 kHz and 10.685 kHz were reported. The mirrors could be driven at their mechanical resonance or at the second harmonic frequency of the mechanical resonance. A peak TOSA exceeding 30° was measured for both mirrors for a signal amplitude of 200 V when driven at the second harmonic frequency of their mechanical resonance.

In the following chapter, the mechanical resonance of both devices is reported to Q-switch a Nd: YAG laser, which had tunable pulse duration enabled by controlling the scan angle of the MEMS mirror being actuated. In Chapter 4, static tilt control of the ET mirror is reported to enable wavelength tuning of a continuous wave Yb: KGW laser when combined with a dispersing prism in the Littman configuration. The same Yb: KGW laser platform is then reported to yield tunable output wavelength and Q-switch pulse duration, enabled by dual-axis tilt control of the ET mirror.

3. Q-switched Nd: YAG laser with flexible temporal output characteristics

A Nd: YAG laser Q-switched by a scanning MEMS mirror was previously reported in [18]. For this chapter, the same Nd: YAG laser module was used but in a different resonator configuration to allow improved flexibility of the temporal output characteristics such as pulse duration control and pulse burst mode. Both families of MEMS mirrors characterized in Chapter 2, electrostatic (ES) and electrothermal (ET), were used as intracavity mirrors in one laser system. The different resonant frequencies of the ES and ET mirrors allowed two separate Q-switch rates by alternating which mirror was resonantly scanning. The pulse duration could be tuned by controlling the rotational speed of the mirrors. Finally, the laser could be on/off controlled using the static tilt capability of the ET mirror, enabling bursts of pulses in a form of pulse-on-demand.

This proof-of-concept demonstration aims to show the broad range of possibilities enabled by MEMS as intracavity mirrors in solid-state lasers; and is to my knowledge the first to use multiple intracavity MEMS mirrors to tune the properties of a single laser output beam. The design of the experiment is described in Section 3.1 and includes details of the laser construction and the measurement setup. The experimental characterization of the laser is then given in Section 3.2. The chapter is then rounded off with a discussion of the results in Section 3.3.

3.1. Experiment design

3.1.1. Gain medium and pump source

The laser gain medium used for this work is commercially available from Northrop Grumman (item number RBAT30-1C2). The module contained a Nd: YAG rod with a length of 63 mm, a diameter of 3 mm and a doping concentration of 0.6% (atomic weight). Both end facets of the rod were anti-reflection coated at $\lambda = 1064$ nm. Three laser diode bars were located radially around the rod to provide the source of optical pumping. The module was liquid cooled to room temperature via a pump system that used a 66/33 % mix of water and

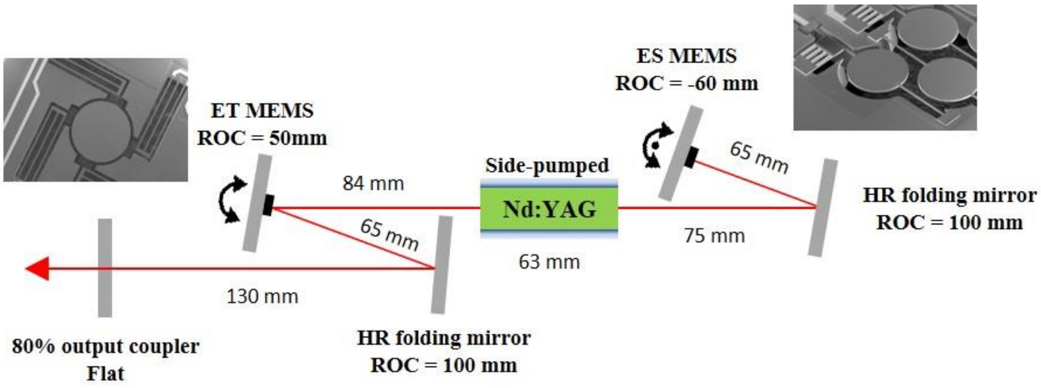

Figure 3-1: Diagram of the Nd: YAG laser with two MEMS mirrors to enable flexible temporal output characteristics.

ethylene glycol. The laser diode bars were powered by a Glassman Europe LP35-35 DC power supply. A full characterization of the working Nd: YAG module was reported in [65], including the efficiency of the laser diode bars and the thermal lensing effect.

3.1.2. Resonator

The resonator was designed using the optical simulator tool WinLase. The simulator computed the ABCD-matrices of common laser components and provided information about the laser stability and the 1/e^2 width of the intracavity beam. A summary of the ABCD-matrix method and its use in WinLase was previously given in Section 1.1.3. The intracavity beam was assumed to be Gaussian and parallel to the optical table. Two important factors considered in the resonator design were the diameter of the MEMS mirrors and the room for change in their surface curvature. Firstly, the incident laser beam must be confined to the mirror surface, which was small when compared to conventional laser mirrors. Secondly, a proportion of the incident laser power would be absorbed within the multilayer structures of the coated MEMS mirrors, resulting in heating. This would cause the mirrors to deform through thermal expansion of the material layers with different thermal expansion coefficients.

As a result of the above-mentioned factors, the complexity of the resonator construction increased. The five-mirror resonator shown in Figure 3-1 was designed to fold the intracavity beam onto the MEMS mirrors and provide enough flexibility for the mirror curvature to shift during operation of the laser. A HR folding mirror with a concave ROC of 100 mm was used on one side of the Nd: YAG rod to fold the intracavity beam onto the ES mirror. Recall that an array of dielectric-coated ES mirrors was characterized in Section 2.3. For this work, the

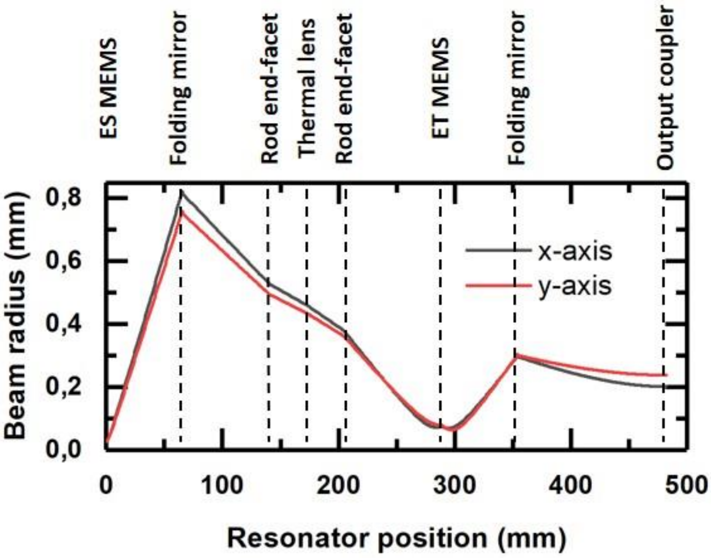

Figure 3-2: Plot of the simulated intracavity beam radius over the length of the resonator.

mirror with a resonant frequency of 10.06 kHz was used. The folding mirror was positioned 75 mm from the Nd: YAG rod at an angle of 5° and 65 mm from the surface of the ES mirror, which had a convex ROC of 60 mm and a diameter of 750 µm. On the other side of the rod, the gold-coated ET mirror (also from chapter 2) which had a concave ROC of 50 mm and a diameter of 1.4 mm was positioned 84 mm from the end facet of the rod at an angle of 5°. This was proceeded by another HR folding mirror with a concave ROC of 100 mm at a distance of 100 mm from the ET mirror. The folding mirror was again angled at 5° and was proceeded by the output coupler, which was flat and had a reflectance of 80 % at λ = 1064 nm. The described resonator had a total physical length of 482 mm.

The Nd: YAG rod was simulated in WinLase as two slabs with a length of 31.5 mm and a refractive index of 1.82. The slabs were separated by a thin lens with a focal length of 560 mm to simulate the thermal lensing effect at an optical pump power of 86 W [65]. The resonator mirrors were simulated with their specified ROC values and angles of incidence. A plot of the simulated intracavity beam radius ($1/e^2$) is shown in Figure 3-2. The simulated beam radius was observed to be comfortably confined within the edges of the MEMS mirrors, with values of 28 ± 3 µm and 70 ± 7 µm at the surfaces of the ES and ET mirrors respectively. The described variation in the beam radius was a result of the 5 ° incidence angle of the folding mirrors and the computed range of MEMS mirror ROC's (30 mm to 500 mm). For the same parameters, the resonator stability factor was computed to be 0.8 ± 0.19 over the computed range of MEMS mirror ROC's. This factor was calculated by

WinLase which uses the g-parameter method of analysing resonator stability, as discussed in Section 1.1.3. The computed stability characteristic indicated that the induced change in curvature of the MEMS mirrors was not expected to have a large impact on the resonator stability.

3.1.3. Measurement setup

The five-mirror laser was constructed and aligned such that the lowest CW laser threshold was achieved. This was done by using a HeNe laser as an alignment reference and finely adjusting the angles of the resonator mirrors. The minimum CW laser threshold was realised at an optical pump power of 56.2 W, which was ~ 11 W higher than the threshold of a standard 2-mirror resonator built around the same laser module (80% output coupler + HR end mirror). This increase corresponded to losses due to absorption at the MEMS mirrors and scattering at the surfaces of the angled resonator mirrors.

The MEMS mirrors were set up identically to that of their characterization in Chapter 2. The ES mirror was connected to an Agilent 33250A signal generator via a 20x voltage amplifier and a series 10 kΩ resistor to protect the mirror from damage in the case of a short circuit at the comb-drive. The maximum signal amplitude that could be supplied to the ES mirror was 200 V, limited by the output of the signal generator & amplifier. The signal generator was configured to output a square-wave signal with a frequency of 10.06 kHz, a duty cycle of 50 % and an offset equal to half the signal amplitude. The ET mirror was connected directly to another Agilent 33250A signal generator. The ET mirror could be driven at its resonant frequency (2.06 kHz) or statically by outputting a DC voltage signal. The maximum signal amplitude that could be supplied to the ET mirror was 10 V, limited by the output range of the signal generator.

To measure the temporal properties of the output beam from the Q-switched laser, the beam was focused onto a 1.5 GHz photodiode as shown in Figure 3-3a. A neutral density filter was used immediately before the photodiode to reduce the incident optical power and prevent damaging the device. This was done after re-directing the output beam using two silver-coated mirrors, M1 and M2, to allow adequate space on the optical bench for all the measurement equipment. The output from the photodiode was input to a Femto DHPCA-100 amplifier (bandwidth up to 200 MHz) and then to an Agilent DS06034A oscilloscope. The average optical power of the laser output beam was measured using a thermal power detector

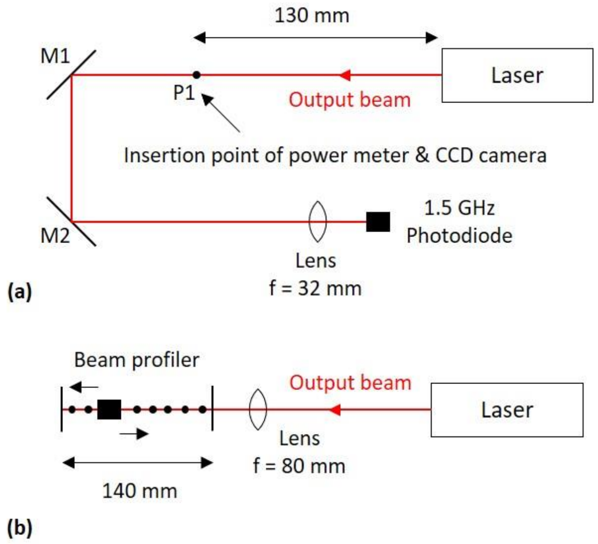

Figure 3-3: (a) Measurement setup for the temporal properties, optical power and transverse mode profile of the laser output beam. (b) Measurement setup for the M^2 beam divergence rate of the laser output beam.

(Gentec XLP12-3S) inserted into the path of the output beam at point P1 in Figure 3-3a, prior to the silver-coated mirrors.

The spatial properties of the laser output beam were measured using a CCD camera (WinCamD UCD12) and a beam profiler (Thorlabs BP104-IR). Neutral density filters were used accordingly to reduce the incident optical power and prevent damage to the devices. The CCD camera was inserted into the beam path at point P1 in Figure 3-3a, 130 mm from the output coupler. This was used to measure the transverse mode profile of the beam. The beam profiler was used to measure the beam divergence rate according to Figure 3-3b. The M^2 divergence rate was used, which is a dimensionless parameter that compares the divergence of a laser beam to that of an ideal Gaussian beam at the same wavelength. To measure the M^2, the beam was first focused using a lens with a focal length of 80 mm. The focal point was identified using the beam profiler, and the $1/e^2$ beam radius, w, was then measured in 10 mm intervals on either side over a range of 140 mm. The measured distribution was then fitted to a simulated Gaussian beam distribution defined by Equation 3-1 [21], where w_{fit} is the beam radius at a distance z from the focal point, w_f is the beam radius at the focal point and λ is the laser wavelength (1064 nm).

$$w_{fit}(z) = w_f \sqrt{1 + \left(\frac{z\,\lambda\,M^2}{\pi\,w_f^2}\right)^2} \qquad \text{(Equation 3-1)}$$

3.2. Laser characterization

The following subsections provide the experimental characterization of the laser described in Section 3.1. The characterization is split into three subsections. The first investigates tunable pulse duration enabled by controlling the scan angle of the ES mirror. The second investigates two separate Q-switch rates enabled by actuation of either the ES or ET mirror, which have different resonant frequencies. The third investigates a form of pulse-on-demand enabled by static tilt of the ET mirror, which brings the resonator into and out of alignment. To prevent damage to the surface of the MEMS mirrors due to laser heating, the average output power of the Q-switched laser was limited to 50 mW for this investigation. This limit was chosen based on the failure limit of the MEMS mirrors from past experiments.

3.2.1. Tunable pulse duration

The five-mirror Nd: YAG laser was originally set up in CW mode to find the optimal alignment with no actuation of the MEMS mirrors. The minimum pump power required to achieve the CW laser threshold was 56.2 W. The laser could then be Q-switched by activating the mechanical resonance of one of the MEMS mirrors, by which the resonator losses were controlled by the tilt angle of the scanning mirror. The duration of the resulting laser pulses was controllable through the rotational speed of the MEMS mirror as it passed through resonator alignment, which was dependent on the scan angle of the mirror. Changing the mirror scan angle, and inherently its rotational speed, could be done in two ways: changing the frequency or changing the amplitude of the driving signal supplied to the MEMS mirror. In order to maintain the same Q-switch rate, the signal amplitude was chosen as the tuning mechanism in this work.

Properties of the laser output at the maximum mirror scan angle

The ES mirror was used as the Q-switch device to investigate tunable pulse duration because it yielded the largest scan angle. Recall from Section 2.3.3 that the ES mirror could be driven either at its resonant frequency (f_{res}) or at its corresponding double harmonic (f_{2x}), both of which resulted in the same mirror movement frequency, f_{res}. The peak value of the TOSA for each driving scheme was detected at f_{res} = 10.06 kHz and f_{2x} = 20.09 kHz, with f_{2x} giving the largest TOSA of 31.3° at a signal amplitude of 200 V. The laser was first investigated with the ES mirror scanning at its largest scan angle.

With the laser initially operating in CW mode just above the laser threshold, the mechanical resonance of the ES mirror was then activated resulting in the mirror scanning at a TOSA of 31.3°. Lasing was lost at this point because the laser threshold for Q-switching was higher than that of CW mode. The new laser threshold was reached at an optical pump power of 59.6 W. The optical pump power was further increased until an average output power of 50 mW was achieved. This was realised at a pump power of 64.1 W. The TOSA was monitored by directing the beam from a HeNe laser onto the ES mirror and reflecting it onto a screen. The TOSA of the ES mirror was measured to increase to 31.7° as a result of the increase in laser power. This was a result of heating which caused thermal expansion of the MEMS structure, leading to a change in the distance between the interleaving combs of the comb-drive. The temperature dependent material properties of single crystal silicon were also a factor in this effect.

A plot showing a sample of the pulsed laser output (pulse train) is shown in Figure 3-4a and a zoomed plot of a single pulse is shown in Figure 3-4c. The pulse emission frequency was double the resonant frequency of the ES mirror, which in this case was equal to the mirror driving frequency, 20.09 kHz. Consecutive pulses were measured to have different pulse durations, indicating that the mirror was moving slower in one direction when it passed through laser alignment. This could be compensated by making small adjustments to the angle of the ES mirror within the resonator. However, nonlinearities meant that every change in the mirror driving signal required further fine tuning of the mirror angle within the resonator. In the interest of time, and to represent a realistic system, the laser was characterized for one alignment only.

A FWHM pulse duration of 477 ± 2 ns was measured when the ES mirror was scanning in one direction and a duration of 513 ± 2 ns was measured when scanning in the opposite direction. The average pulse amplitude jitter was measured to be 7 % and the average timing jitter was measured to be 4 ns. The pulse train was temporally compared to the driving signal of the ES mirror and the time at which the ES mirror was at the midpoint of its scanning movement. The midpoint was detected using a HeNe laser directed towards the ES mirror and a 2 GHz photodiode positioned at the centre of the resulting scan line. It was later discovered that the photodiode was damaged, resulting in an uncharacteristic response especially on the falling edge of the input signal. However, the rising edge was still successfully detected and could be used for these measurements. Alike

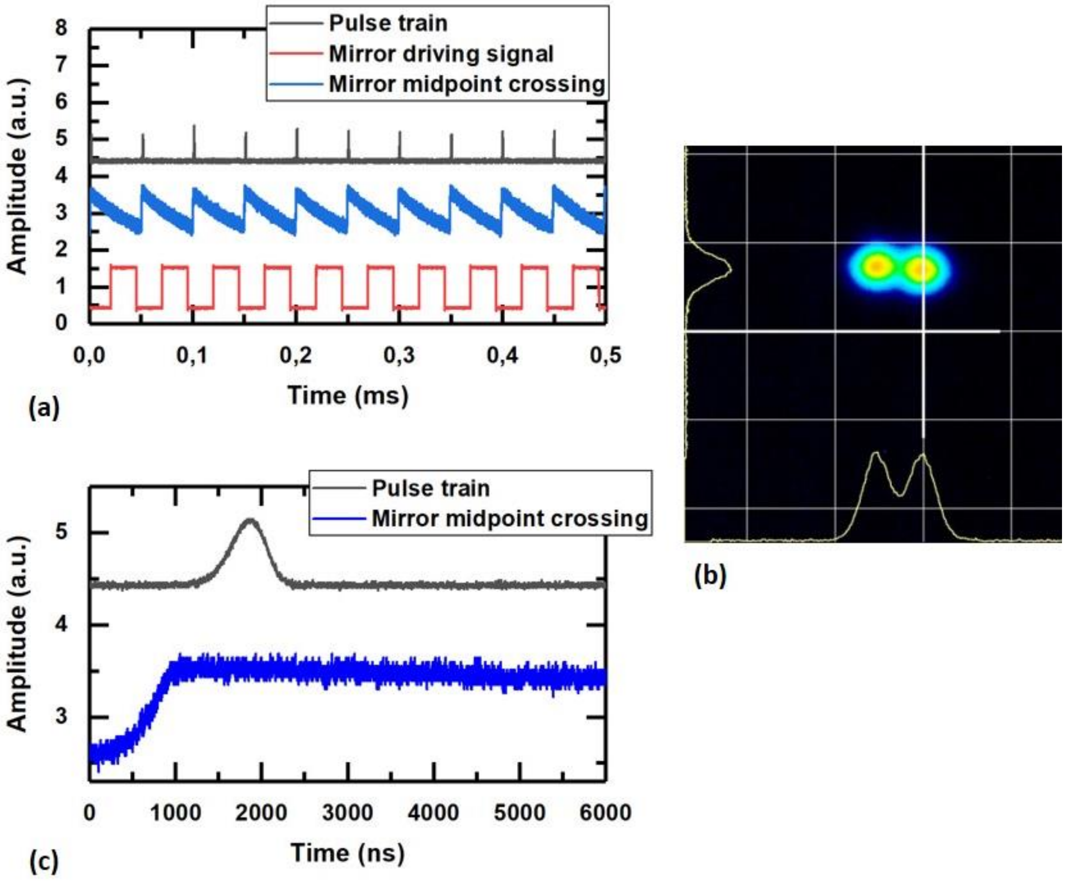

Figure 3-4: Laser output characteristics with a signal of amplitude 200 V and frequency 20.09 kHz supplied to the ES mirror. (a) Temporal comparison of the laser pulse train, the mirror driving signal and the midpoint crossing of the mirror scanning movement. (b) Image of the transverse mode profile taken directly from a CCD camera. (c) Measured profile of a sample pulse temporally compared to the midpoint crossing of the mirror scanning movement.

the work in [18], a delay was observed between crossing the midpoint of the mirror movement and pulse emission. The delay was measured to be ~ 850 ns. The delay in pulse emission resulted in a dual-spot output beam since the delay occurred for all pulses emitted when the ES mirror was scanning back and forth in opposite directions. The measured transverse mode profile of the output beam is shown in Figure 3-4b. The profile for both beams was observed to be TEM_{00} and the M^2 beam divergence was measured to be 1.3 on the x-axis and 1.1 on the y-axis.

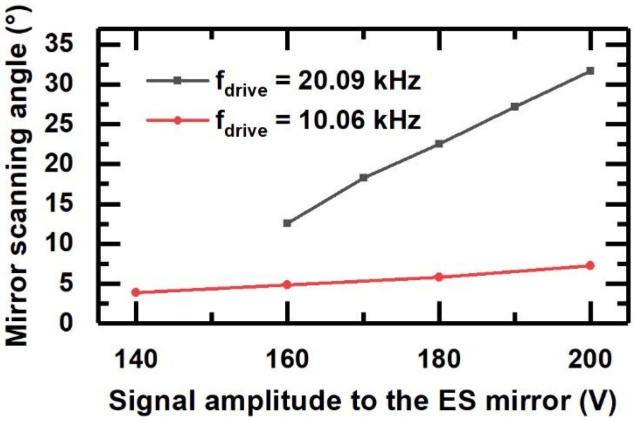

Figure 3-5: Plot showing the scanning angle of the ES mirror against the amplitude of the driving signal at frequencies of 20.09 kHz and 10.06 kHz.

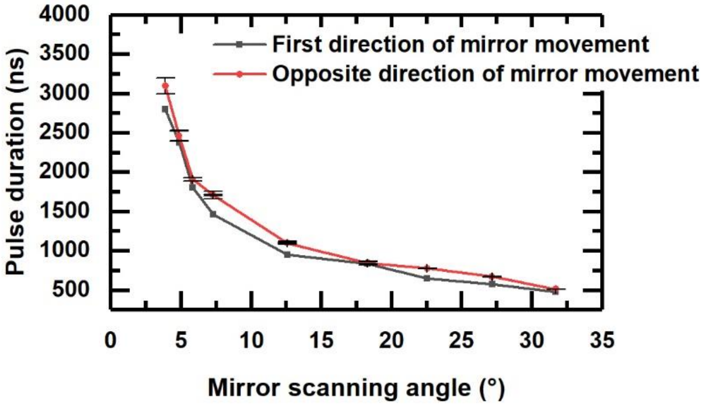

Figure 3-6: Plot showing the FWHM pulse duration of the Q-switched laser output against the scanning angle of the ES mirror.

Properties of the laser output when the mirror scan angle was reduced

The scanning angle of the ES mirror was changed by modifying the amplitude of its driving signal. At every change, the pump power was adjusted to achieve an average laser output power of 50 mW and the temporal characteristics of the laser output were measured. At f_{2x} = 20.09 kHz, the driving voltage was reduced from 200 V to 160 V in steps of 10 V. The mirror TOSA was measured and was observed to decrease from 31.7° to 12.6°. This was the lowest driving voltage that could sustain resonant scanning of the ES mirror at a driving frequency of 20.09 kHz. A plot of the mirror scanning angle against the driving voltage is shown in Figure 3-5. To achieve lower TOSA values, the driving frequency was changed to

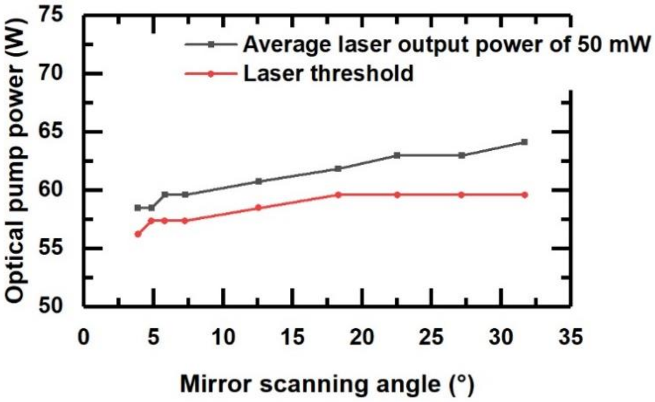

Figure 3-7: Plot showing the optical pump power required to achieve laser threshold and an average laser output power of 50 mW against the scanning angle of the ES mirror.

f_{res} = 10.06 kHz. The TOSA was then measured to decrease from 7.3° at 200 V to 3.9° at 140 V.

The average duration of pulses emitted when the ES mirror was scanning in opposite directions continued to be different at lower mirror scanning angles. However, both were observed to increase as the mirror scanning angle was reduced. At f_{2x} = 20.09 kHz, the pulse duration for one scanning direction increased from 477 ± 2 ns to 950 ± 20 ns for respective TOSA's of 31.7° and 12.6°. The pulse duration for the other scanning direction increased respectively from 513 ± 2 ns to 1103 ± 5 ns. At f_{res} = 10.06 kHz, the pulse duration for one scanning direction increased from 1465 ± 10 ns to 2800 ± 100 ns for respective TOSA's of 7.3° and 3.9°. The pulse duration for the opposite scanning direction increased respectively from 1710 ± 50 ns to 3100 ± 100 ns. A plot of the pulse duration against mirror scanning angle is shown in Figure 3-6. The mirror scan angle was not reduced further because this resulted in multiple pulsing, indicating that the switching speed was too slow to allow efficient Q-switching.

The optical pump power to achieve laser threshold and to achieve an average laser output power of 50 mW at each change in mirror scan angle was recorded. Both were observed to decrease as the mirror scanning angle was decreased, as shown in Figure 3-7. The laser threshold decreased from 59.6 W to 56.2 W when the mirror TOSA was reduced from 31.7° to 3.9° respectively. For the same scan angles, the pump power to achieve an average laser output power of 50 mW decreased from 64.1 W to 58.5 W. This is consistent with the mirror moving more slowly through resonator alignment, resulting in pulse build-up occurring nearer the angle of lowest resonator loss.

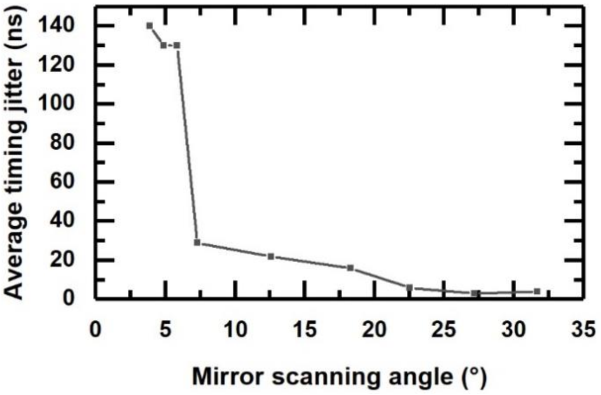

Figure 3-8: Plot showing the average timing jitter of the Q-switched laser output against the scanning angle of the ES mirror.

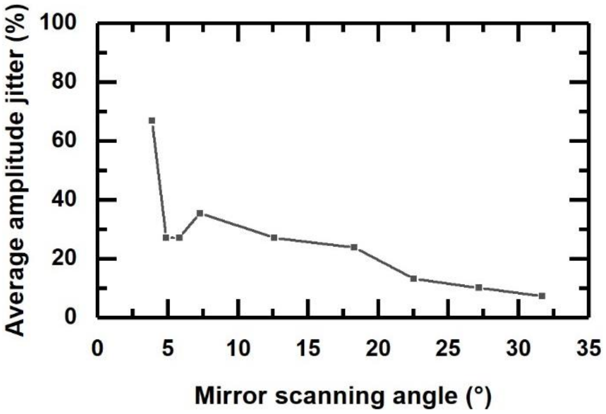

Figure 3-9: Plot showing the average amplitude jitter of the Q-switched laser output against the scanning angle of the ES mirror.

The average timing jitter and the average amplitude jitter of the pulsed laser output were measured as the mirror scanning angle was decreased. A plot of the timing jitter is shown in Figure 3-8 and a plot of the amplitude jitter is given in Figure 3-9. Both were observed to become more erratic at lower scanning angles. The average timing jitter was measured to be below 30 ns until a mirror scanning angle of 7.3°. It then spiked to over 130 ns for lower scanning angles. The average amplitude jitter showed an increasing trend from 7% at a TOSA of 31.7° to 67% at a TOSA of 3.9°. The amplitude jitter at a scanning angle of 3.9° even contributed to a completely missing pulse in the sample pulse train shown in Figure 3-10. The exact cause of the jitter fluctuation is unknown but was most likely caused by very small nonlinearities in the movement of the ES mirror. Small changes in the resonator alignment, and thus the laser dynamics, would have been caused by laser heating of the mirror and the resulting change in its scanning movement and surface curvature. The laser heating for each pulse duration may have been different due to differences in the thermal dissipation.

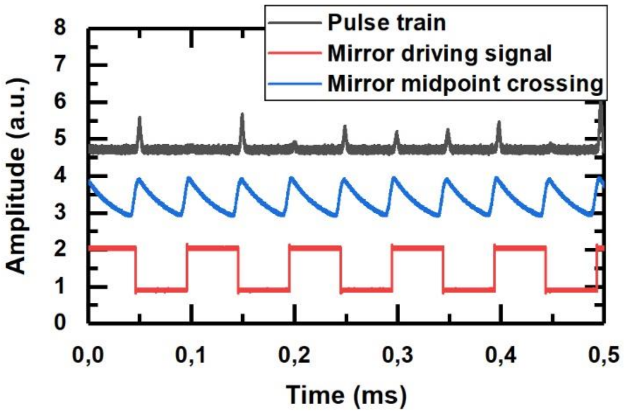

Figure 3-10: Temporal comparison of the laser pulse train, the mirror driving signal and the midpoint crossing of the mirror scanning movement. The driving signal of the ES mirror had a frequency of 10.06 kHz and an amplitude of 140 V.

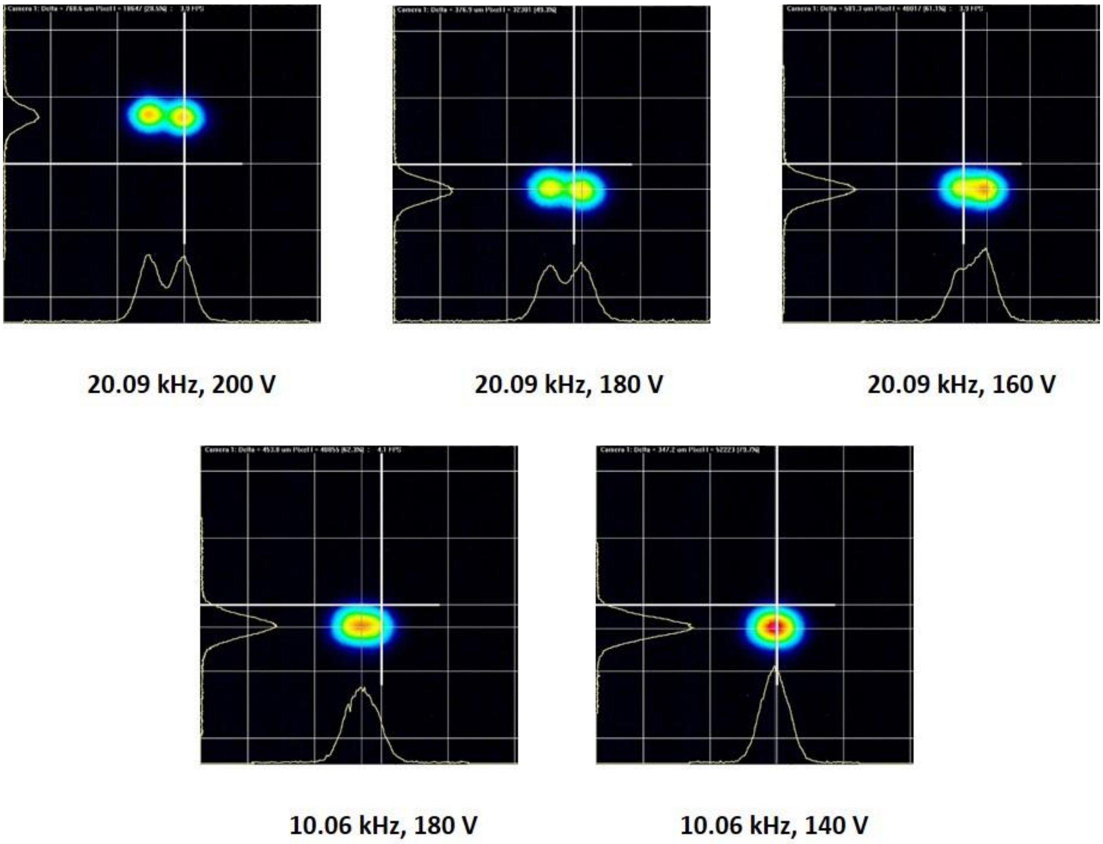
20.09 kHz, 200 V

20.09 kHz, 180 V

20.09 kHz, 160 V

10.06 kHz, 180 V

10.06 kHz, 140 V

Figure 3-11: Transverse mode profile of the laser output beam for different driving signals supplied to the ES mirror.

The transverse mode profile of the laser output was monitored 130 mm from the output coupler as the pulse duration was tuned. The profile at every pulse duration was observed to be TEM_{00} for both beams emitted when the ES mirror was scanning in both directions. Images of the transverse mode profile taken using the CCD camera are shown in Figure 3-11. The angular offset between the two beams decreased as the pulse duration decreased. This was a result of the reduced rotational speed of the mirror, meaning that pulse emission occurred nearer the centre of the scanning movement. This resulted in overlapping of several of the measured beams, which made accurate measurement of the M^2 beam divergence impossible. It is not expected that the M^2 deviated much from the values measured for the largest mirror scan angle.

3.2.2. Different Q-switch rates

The inclusion of two separate MEMS mirrors within the resonator enabled use of either mirror to Q-switch the laser. The ES mirror could Q-switch the laser at a rate of 20.09 kHz while the ET mirror could Q-switch the laser at a rate of 4.12 kHz. With the ES mirror Q-switch characterized in the previous section, the ET mirror was now investigated as the Q-switch and compared to use of the ES mirror.

Recap of the ET mirror performance

Recall from Section 2.2.4 that the scanning movement of the ET mirror was elliptical due to coupling between the resonant axes, originating from the radial positioning of four identical actuators (see Figure 3-12a). The largest mirror scan angle with the setup available was measured to be 7.1° for a signal with an amplitude of 10 V and a frequency of 2.05 kHz (applied to the south actuator, A4). The offset between the upwards and downwards motion of the mirror was measured to be 1.5°, and the offset between the centre of the scanning movement and the mirror rest position was 2° on the y-axis (see Figure 3-12b). There was also a very small offset on the x-axis, measured to be less than 0.2°. The measurement accuracy was limited by the width of the beam from the HeNe laser used to analyse the mirror scanning movement.

It was expected that the angular offset between the upward and downward motions of the mirror would cause the laser to misalign when the ET mirror was resonantly scanning, since the movement path would never precisely cross the point that laser alignment was set up for (the mirror resting position). A trade-off was therefore made between the ellipticity and the

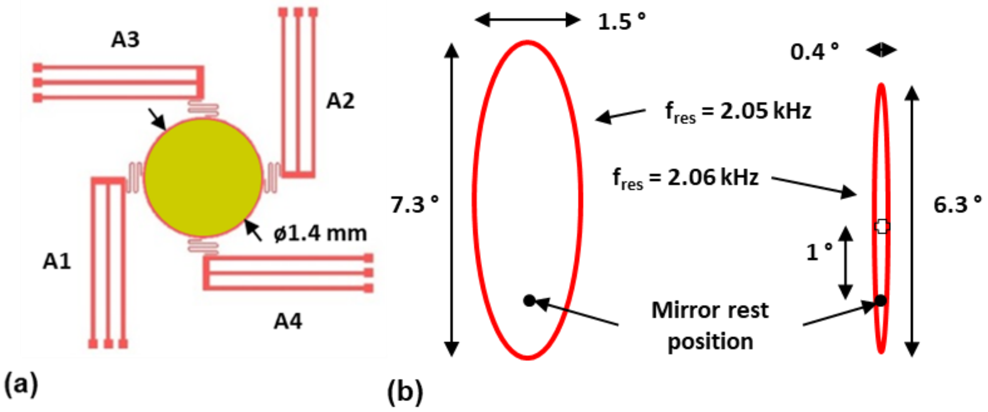

Figure 3-12: (a) Schematic of the ET mirror design. (b) Illustration of the elliptical scan profile of the ET mirror resonantly driven at frequencies of 2.05 kHz and 2.06 kHz. The signal amplitude was 10 V in both cases and the signal was applied to A4.

mirror scan angle, ensuring that laser alignment was still possible with the shortest possible pulse duration. A resonant frequency of 2.06 kHz was chosen, resulting in a mirror TOSA of 6.3° for a signal amplitude of 10 V, with an offset of 0.4° between the upwards and downwards movements of the scan profile. The offset between the centre of the scanning movement and the mirror rest position was 1° on the y-axis and less than 0.2° on the x-axis.

Properties of the laser output at the maximum scan angle

The scan profile of the ET mirror meant that only one of the mirror movement directions resulted in pulse emission. The Q-switch rate was therefore 2.06 kHz as opposed to the rate of 4.12 kHz that was predicted previously. The laser threshold was reached at an optical pump power of 56.2 W and the pump power required to achieve an average output power of 50 mW was 59.6 W. A plot of a sample pulse train is shown in Figure 3-13a and a zoomed plot of a single pulse is shown in Figure 3-13c. The pulse train was temporally compared to the driving signal supplied to the ET mirror. The FWHM pulse duration was measured to be 1450 ± 40 ns with an average timing jitter of 320 ns and an average amplitude jitter of 9%. The transverse mode profile was measured 130 mm from the output coupler and is shown in Figure 3-13b. The profile was observed to be TEM_{00} and the M^2 beam divergence was measured to be 1.2 on the x-axis and 1.1 on the y-axis. This was comparable to that of using the ES mirror as the Q-switch.

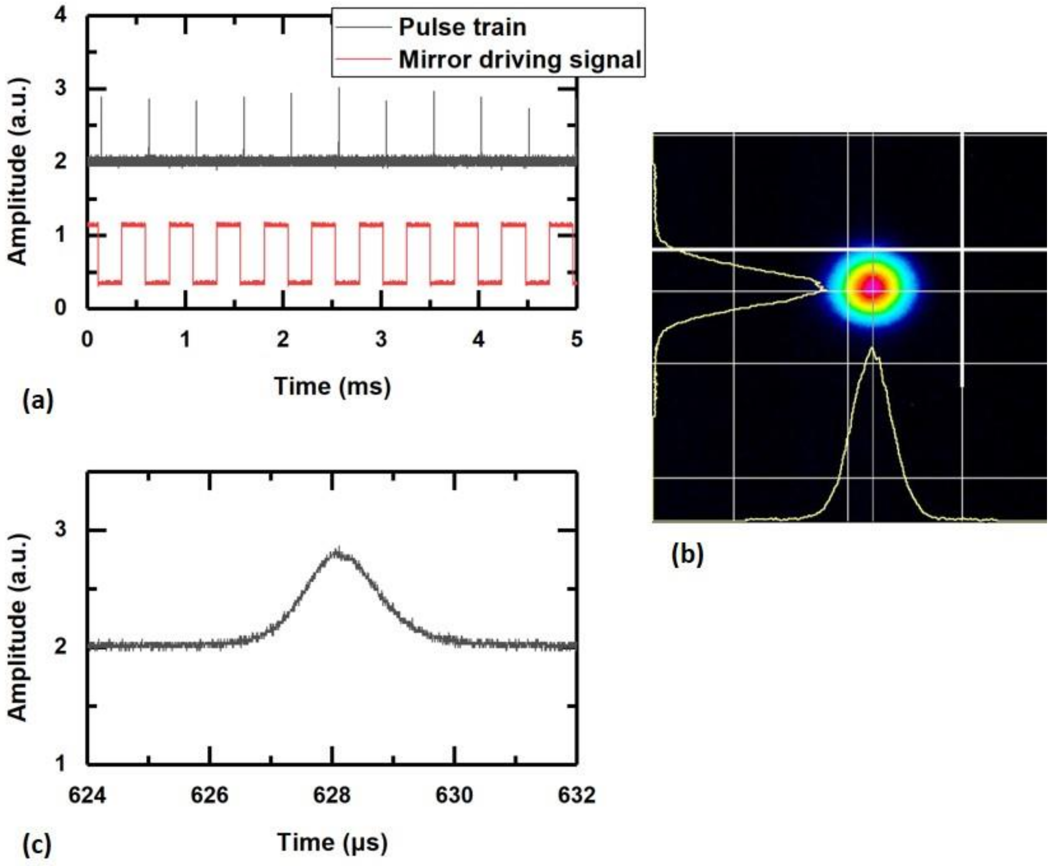

Figure 3-13: Laser output characteristics with a signal of amplitude 10 V and frequency 2.06 kHz supplied to A4 of the ET mirror. (a) Temporal comparison of the laser pulse train and the mirror driving signal (b) Image of the transverse mode profile taken directly from a CCD camera. (c) Measured profile of a sample pulse.

Effects of changing the mirror scan angle

The scanning angle of the ET mirror was changed by modifying the driving signal applied to actuator A4. The signal amplitude was reduced to 9 V while maintaining a frequency of 2.06 kHz, resulting in a reduction of the mirror TOSA from 6.3° to 2.4° on the major axis of the elliptical scanning movement. The high degree of nonlinearity in the mirror response led to a drastic change in the performance of the laser. A sample pulse train of the laser output is given in Figure 3-14. An aperiodic Q-switch rate was observed with two pulses being emitted per movement cycle of the ET mirror. It was evident that both the upward and downward motions of the mirror scanning profile resulted in pulse emission. This was caused by the two sides of the elliptical scan profile coming closer together, which led to

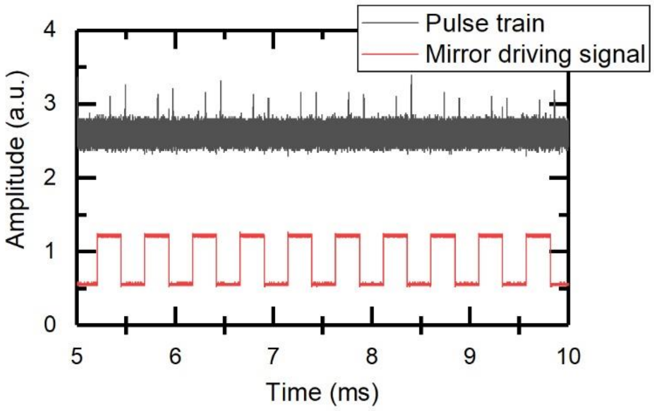

Figure 3-14: Sample pulse train of the laser output with a signal amplitude of 9 V at a frequency of 2.06 kHz applied to the ET mirror.

both movement directions coming into laser alignment. The average pulse duration was measured to be more than 3500 ns, which also resulted in multiple pulsing just like in the case of using the ES mirror as the Q-switch. Only the maximum scan angle of the ET mirror was therefore usable in this case to achieve an efficient Q-switch.

3.2.3. Pulse-on-demand functionality

As well as Q-switching, the static tilt of the ET mirror could be used to tilt the mirror in and out of resonator alignment. As a result, the pulsed laser output could be turned on and off digitally on-demand. To demonstrate this, the laser was first setup to be Q-switched by the ES mirror with a supplied signal amplitude of 200 V at a frequency of 20.09 kHz. The optical pump power was adjusted such that the average laser output power was 50 mW. A signal with an amplitude of 10 V and a frequency of 10 Hz was then supplied to actuator A1 of the ET mirror (see Figure 3-12a). The optical tilt angle of the mirror was therefore alternating between 0° (rest position) and 2.7° at a rate of 10 Hz.

A sample pulse train of the laser output is shown in Figure 3-15. Spikes in the laser output were observed because of the ripple in the power supply to the pump diodes, which is discussed further in Section 3.3. The on / off switching time of the laser was dependent on the switching speed of the ET mirror. The switching time was measured by temporally comparing the pulse train with the signal supplied to the ET mirror. The resulting plot is given in Figure 3-16, showing the measured switching time of 5 ms. It was observed that for

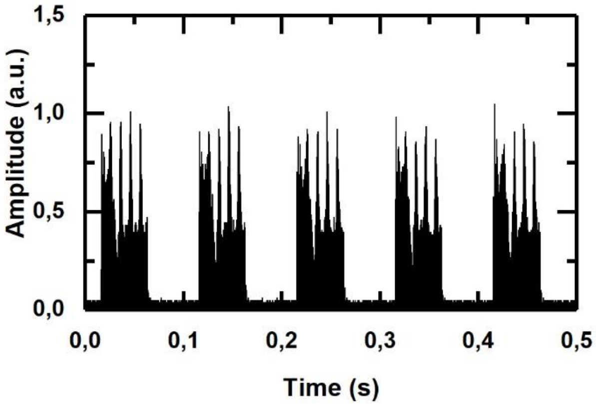

Figure 3-15: Sample pulse train of the pulse-on-demand laser output while a 200 V, 20.09 kHz signal was supplied to the ES mirror and a 10 V, 10 Hz signal was applied to the ET mirror.

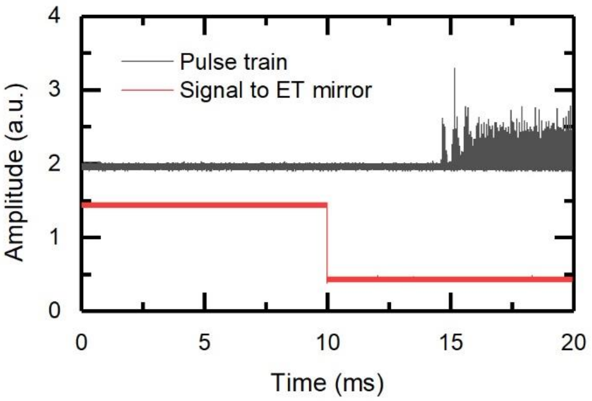

Figure 3-16: Temporal comparison of the laser pulse train and the 10 Hz signal supplied to the ET mirror.

the first few milliseconds of pulsing, the amplitude of the pulses varied periodically. This was most likely caused by the mirror overshooting when moving between tilt angles of 2.7 ° and 0 °. Another effect was also observed where the first 25 ms of pulses in each burst had a higher average amplitude than the remainder of the pulses. The cause of this effect is currently unknown.

3.3. Discussion

A proof-of-concept characterization of a MEMS Q-switched solid-state laser with flexible temporal output characteristics has been reported. The use of two MEMS mirrors with different actuation mechanisms enabled three different laser functionalities. The first was tunable pulse duration between ~ 500 ns and ~ 3000 ns. The second was two separate Q-switch rates of ~ 20 kHz and ~ 2 kHz. The third was a form of pulse-on-demand, where one mirror Q-switched the laser and the other tilted in and out of laser alignment.

The average laser output power for this work was limited to 50 mW to prevent damage to the surface of the MEMS mirrors through ablation or laser heating. This laser output power can be used for some biomedical applications, but to be compatible with use in defence or manufacturing applications, the average output power would have to be scaled up to over 1 W. Two failure modes were experienced previously for an average output power approaching 100 mW. The first was ablation of the gold-coating on the ET mirror. The second was physical locking of the comb-drive on the ES mirror. The locking occurred because of electrostatic pull-in, which can be caused by thermal expansion and the temperature dependent material properties of single crystal silicon. The scanning movement of the ES mirror was therefore prohibited. This so-called pull-in effect has been reported previously in literature and is a known failure mode of electrostatic comb-drives.

To enable power-scaling beyond 1 W, HR coatings with more than 99% reflectance would be required to reduce the absorption within the MEMS mirror. Ideally the coating would also be thermally balanced to prevent a change in mirror curvature through laser heating. To this date, such a coating has not been developed for a MEMS mirror. The optical coating also had an influence on the resonator which was designed to focus the beam onto the MEMS mirrors and provide enough freedom for the curvature of the MEMS mirrors to shift during operation of the laser. The development of a HR coating for MEMS mirrors with a flat surface profile would also enable a much simpler resonator design and reduce the spatial requirements of the laser. The resonator could even be further simplified by the development of a hybrid MEMS device to enable all the laser functionalities by itself.

Nonlinearity in the responses of both the ET and ES mirrors had an impact on the laser performance. The ellipticity of the scanning movement of the ET mirror could be prevented by using actuators with different eigenfrequencies on the two orthogonal axes of rotation. This would reduce the coupling between the axes and result in a 1D scanning movement. The laser could then be Q-switched at double the mirror movement frequency like that reported with use of the ES mirror. As for the ES mirror, nonlinearities arise from several factors. The two most notable factors are the one-sided design of the comb-drive and coupling between eigenfrequencies of the mirror structure. Improvements to the design of the ES mirror could help reduce such nonlinearities.

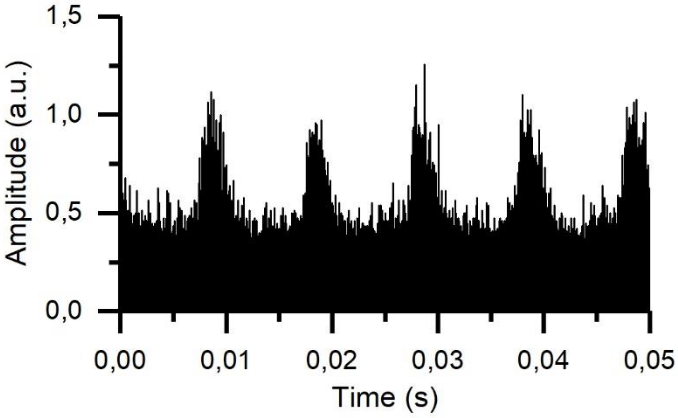

Figure 3-17: Sample pulse train of the laser output over a longer timeframe to show the effects of a ripple in the output signal of the pump diode power supply.

Another factor which had an influence on the performance of this laser was a ripple in the electrical output of the power supply to the pump diodes. This was specified as up to 300 mA at a frequency of 100 Hz and was observed to change the amplitude and pulse duration of the laser pulses. A sample pulse train over a time frame of 50 ms is shown in Figure 3-17, showing the effect of the ripple on the 50-mW laser output when the ES mirror was scanning at a TOSA of 31.7°. While this could be eliminated using a better-quality power supply, it is worth noting because it could have impacted the measurements of the pulse duration, amplitude jitter and timing jitter.

4. Wavelength tunable Yb: KGW laser

Previous work involving MEMS mirrors as intracavity elements in solid-state lasers has focused on tuning the temporal and spatial characteristics of the output beam. In this chapter, the concept of using an intracavity MEMS mirror to tune the spectral characteristics of the output beam from a solid-state laser is investigated. The concepts of tuning the output wavelength of lasers were discussed previously in Chapter 1. In the context of solid-state lasers, the most common method of wavelength tuning is the use of optical filters such as etalons, birefringent filters, dispersing prisms or diffraction gratings. The use of etalons and birefringent filters for wavelength tuning are not reliant on mirrors and are thus inapplicable to the use of MEMS mirrors as the tuning element. Prism-pairs combined with a movable aperture or a single prism combined with a rotatable mirror can actively tune the wavelength of minimum losses within the resonator. Gratings are used in the Littrow or Littman configurations which were shown in Figure 1-4. In the Littrow configuration, the grating is rotated to tune the wavelength of minimum losses within the resonator. The Littman configuration uses a similar concept, but the grating is combined with a rotatable mirror as the tuning element.

In this chapter, the use of a dispersing prism combined with a MEMS mirror is reported to tune the output wavelength of an end pumped Yb: KGW laser. The MEMS mirror used for this work was the mirror with electrothermal (ET) actuators which was characterized in Chapter 2. Static tilt of the ET mirror was used to tune the laser wavelength of minimum losses within the resonator. With this gain medium, the theoretical tuning range was between $\lambda = 1020$ nm and $\lambda = 1060$ nm. This is the first reported use of a MEMS mirror to tune the output wavelength of a solid-state laser.

The laser design is described in Section 4.1, including a characterization of the pump source, the Yb: KGW crystal and the design of the resonator. A geometrical optics model of the resonator is then described in Section 4.2 to predict the laser wavelength as the ET mirror is actuated. The impact of the laser dynamics on the tuning performance is also considered. The experimental characterization of the laser is given in Section 4.3 and compared to the results of the geometrical model. The chapter is then rounded off with a discussion of the results in Section 4.4.

4.1. Laser design

Yb: KGW was selected as the laser gain medium for its broad spectral emission band at around $\lambda = 1$ µm when optically pumped at $\lambda_{pump} = 980$ nm. Wavelength tuning using this gain medium was theoretically possible between $\lambda = 1020$ nm and $\lambda = 1060$ nm. The same laser optics as those used for the Nd: YAG laser reported in Chapter 3 could then also be used for this laser. Another factor in the choice of this gain medium was the possibility of Raman scattering, which was used for other projects within the CMP. The design of the tunable laser built around this gain medium is discussed in the following subsections.

4.1.1. End-pump system

A fibre-coupled diode laser (LIMO35-F100-DL980-S1775), with a fibre core diameter of 100 µm and a numerical aperture of 0.22 was used to optically end-pump the Yb: KGW crystal. The diode laser module was mounted on a temperature controller, which was air-cooled at 28 °C to provide optimised optical pumping at $\lambda_{pump} \approx 980$ nm. A SM800 series Delta Elektronika power supply was used to power the diode laser. The threshold of the diode laser was achieved at an input current of 6.3 A. The laser output power then rose linearly to 25.3 W at a maximum input current of 40 A, measured using a Thorlabs S314C power meter. This corresponded to a slope efficiency of 0.76 W/A. A plot of the input current against laser output power is shown in Figure 4-1. The maximum input current to the laser was limited by the specification of the laser module.

The transverse mode profile of the diode laser output was measured using a Thorlabs BP104-IR beam profiler positioned 20 mm from the end of the optical fibre. This was the maximum distance at which the output beam was confined to the aperture of the profiler. To prevent damage to the profiler, the beam was attenuated using a flat laser mirror with a reflectance of 98 % at $\lambda = 980$ nm. This was the only feasible attenuator that could fit in the space provided. The output power of the diode laser was therefore limited to 18 W (attenuated to 360 mW) for measurement of the transverse mode profile. A top hat-shaped transverse mode profile was observed on both the x-axis and the y-axis for laser output powers of 2.7 W, 10.3 W and 18 W. The exposure time of the profiler was adjusted accordingly for each measurement to avoid saturation of the sensor. Images of the measured transverse mode profiles at different laser output powers are shown in Figure 4-2.

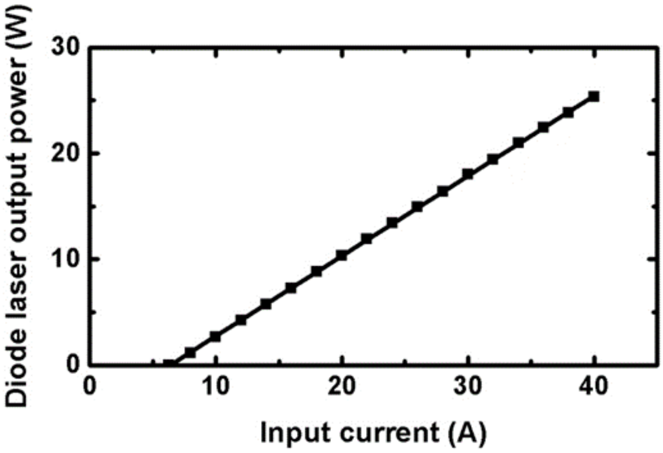

Figure 4-1: Plot of diode laser output power against input current.

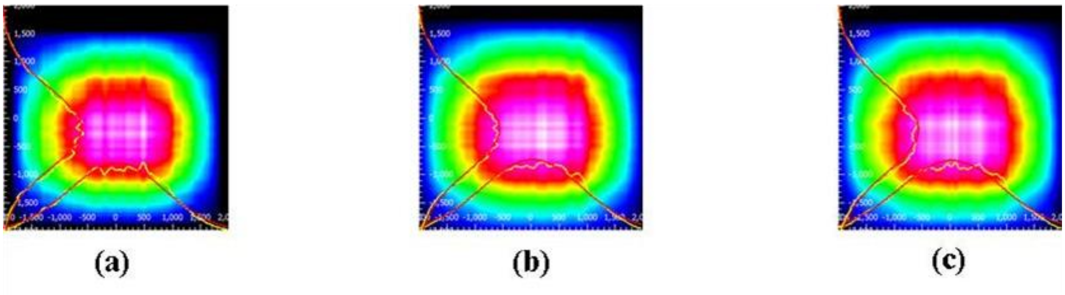
(a) (b) (c)

Figure 4-2: Transverse mode profiles of the diode laser at output powers of (a) 2.67 W, (b) 10.33 W and (c) 18 W.

The output beam from the diode laser was passed through an imaging system designed to focus the beam through the Yb: KGW crystal. A schematic of the imaging system is shown in Figure 4-3. The system consisted of two lenses and a resonator mirror. The first lens had a focal length of 20 mm and was fixed in position 20 mm from the end of the optical fibre. The second lens had a focal length of 40 mm and was mounted on an XYZ-translatable stage 52 mm after the first lens. The second lens was used for fine adjustment of the pump beam propagation through the Yb: KGW crystal. The resonator mirror was a 6 mm thick, 0.5” diameter mirror with a ROC of 250 mm which was positioned 27 mm after the second lens of the imaging system. The mirror was a bandpass filter which was anti-reflectance coated for λ = 808 nm to λ = 980 nm on the pump-side (R < 0.25 %). On the crystal-side, the mirror was high-reflectance coated for λ = 1030 nm to λ = 1200 nm (R > 99.9 %), with a transmission band from λ = 808 nm to λ = 980 nm (R < 5 %). The total optical loss of the pump beam from the surfaces of imaging system was measured to be between 4 % and 5 %.

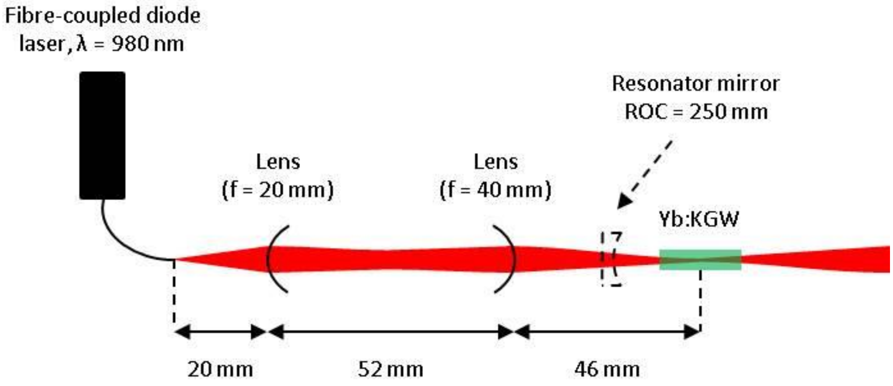

Figure 4-3: Diagram of the end-pump system for the Yb: KGW laser.

The imaging system allowed convenient measurement of the M^2 beam divergence rate using the same method as that described in Chapter 3 (see Figure 3-3b). The Thorlabs beam profiler was used to measure the beam radius at several locations around the beam waist. Distance intervals of 10 mm were used up to 40 mm in either direction from the beam waist. The resulting values were then fitted to a simulated Gaussian beam distribution defined by Equation 3-1. The mirror with 98 % reflectance was again used to attenuate the beam. A filter wheel and a neutral density filter were used to further attenuate the beam to prevent damage to the beam profiler. At a laser output power of 2.7 W, the measured values for the M^2 were 26 on the x-axis (parallel to the optical table) and 24 on the y-axis (perpendicular to the optical table) The M^2 increased to 27 for a pump power of 10.3 W and then increased further to 30 for a pump power of 18.0 W on both the x-axis and the y-axis. The measured M^2 for the pump laser was much larger than that typically achieved with solid-state lasers. This is a common characteristic for laser diodes, where the laser output is often multi-modal.

The movable lens of the imaging system was adjusted in conjunction with the design of a simple two-mirror resonator to match the distribution of the pump beam to that of the intracavity beam of the Yb: KGW laser. This would then enable the best laser efficiency because the pump energy is confined to spatially overlap the laser beam. The two-mirror resonator is described later in Section 4.1.2 to have an expected $1/e^2$ beam radius of between 118 µm and 154 µm within the crystal. The $1/e^2$ radius of the pump beam waist was monitored using the same setup of the Thorlabs beam profiler as that used in the previous M^2 measurement. After adjustment of the lens, the measured beam waist radius was 110 µm at a pump power of 1 W. This then increased to 150 µm at a pump power of 18 W, providing a

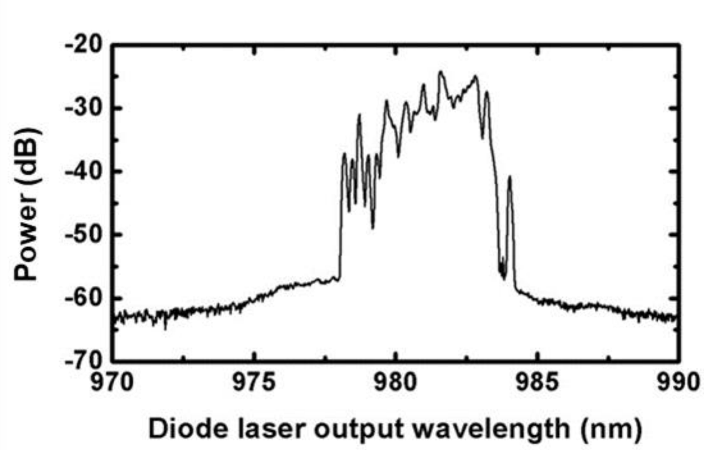

Figure 4-4: Measured optical spectrum of the diode laser output at an output power of 25.3 W.

good match between the distribution of the pump beam and the predicted laser beam. The distance between the movable lens and the pump beam waist was measured to be 46 mm.

To measure the optical spectrum of the resulting pump beam, a proportion of the beam was fed to an optical spectrum analyser (OSA) by collimating it into a fibre optic patch cable. The beam was first attenuated to an output power of less than 250 mW using the flat mirror with 98 % reflectance and a filter wheel to prevent damage to the OSA. The measurement was therefore relative to the coupling efficiency and not absolute. The OSA was configured with a resolution bandwidth of 0.1 nm and a video bandwidth of 2 kHz. The peak pump wavelength at the entrance to the Yb: KGW crystal was measured to be 978 nm at 2.67 W of pump power. This then shifted towards 981.7 nm at the maximum pump power of 25.3 W. The full-width half maximum (FWHM) linewidth was measured to be ~ 2.5 nm throughout. A plot of the optical spectrum measured at a pump power of 25.3 W is shown in Figure 4-4.

4.1.2. Yb: KGW laser crystal

The quasi-three-level laser structure of Yb: KGW is illustrated in Figure 4-5. The pump band, E_3, exists at $\lambda = 980$ nm, which precedes a short, non-radiative transition to the upper laser level, E_2. The laser transition occurs between levels E_2 and E_1, where spectral broadening enables emission from $\lambda = 1020$ nm to $\lambda = 1060$ nm. The term ‘quasi-three-level’ laser arises from the proximity of the lower laser level to the ground state. A significant proportion of the ion population therefore exists in the lower laser level at thermal equilibrium, following the Boltzmann distribution. Significant reabsorption consequently

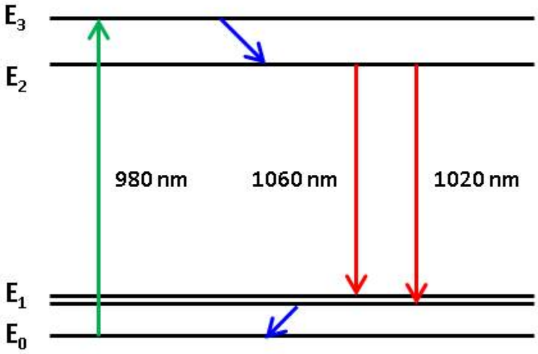

Figure 4-5: Quasi-three-level laser system for Yb: KGW showing the pump (green), laser (red) and short, non-radiative (blue) transitions.

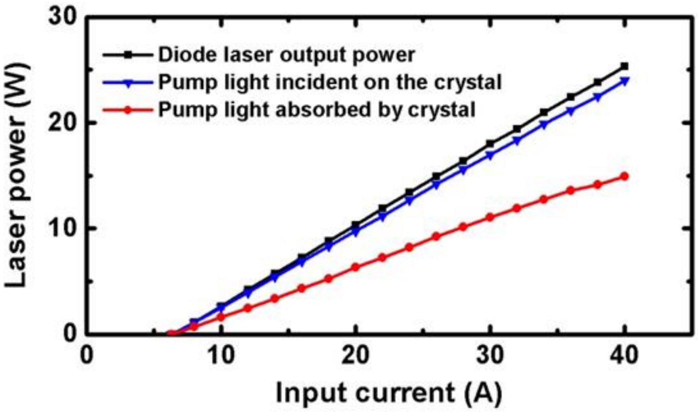

Figure 4-6: Plot showing the diode laser output power, pump light incident on the crystal and pump light absorbed by the crystal against input current to the diode laser.

occurs at the laser wavelength, effectively forming an intermediate step between the three-level and four-level laser systems.

The Yb: KGW laser crystal used for this work was custom-made by Altechna to be N_g-cut with an Yb-doping concentration of 1% (atomic weight). The crystal had a length of 10 mm and the end facets were right-angle cut with dimensions of 5x2 mm. As discussed previously, the crystal was chosen as a trade-off to satisfy two separate research projects: this work based on a tunable laser, and another project involving a Raman laser conducted by colleague Ran Li. The emission cross-section of N_g-cut Yb: KGW is lower than that of N_p or N_m-cut Yb: KGW but was more than adequate for this proof-of-concept investigation.

The end facets of the crystal were anti-reflectance coated and yielded R < 0.1 % between λ = 1020 nm and λ = 1060 nm. It was also anti-reflectance coated between λ = 1130 nm and λ = 1170 nm for use in the Raman laser. The crystal was encased in a custom-built copper

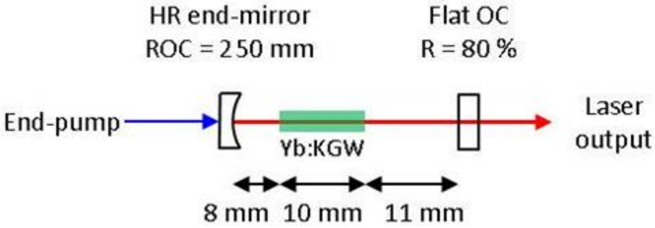

Figure 4-7: Two-mirror laser used to characterise the Yb: KGW laser crystal.

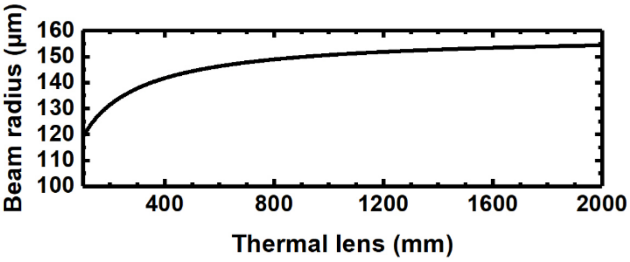

Figure 4-8: Simulated 1/e^2 beam radius at the centre of the crystal against the focal length of the thermal lens for the laser shown in Figure 4-7.

block with openings at the end facets of the crystal to facilitate the laser beam path. Indium foil was placed between the crystal and the copper block to enhance the thermal interface. The block was then water cooled at 22 °C to prevent thermally induced damage to the crystal.

The absorbed pump power within the crystal was calculated by measuring the optical power of the pump beam immediately before and after interaction with the crystal. This was done using a Thorlabs S314C optical power meter. Optical pumping resulted in 63 ± 2 % of the incident pump light being absorbed by the crystal over the full range of pump powers. For a maximum of 25.3 W of incident pump power, 24.0 W was incident on the laser crystal and 14.9 W was absorbed by the crystal. A comparative plot of the pump power from the diode laser, the incident pump power at the Yb: KGW crystal and the absorbed pump power against input current to the diode laser is shown in Figure 4-6.

To further assess the crystal properties, a short two-mirror resonator was designed around the crystal. The resonator was designed using the ABCD-matrix simulator tool WinLase. A diagram of the resonator is shown in Figure 4-7. The Yb: KGW crystal was simulated using two slabs, each of length 5 mm and a refractive index of 2, with a thin lens positioned between for inclusion of thermal lensing effects. A mirror with a ROC of 250 mm was positioned 8 mm from one facet of the crystal. A flat mirror was positioned 11 mm from the opposite crystal facet. An accurate method for measuring the focal length of the thermal lens

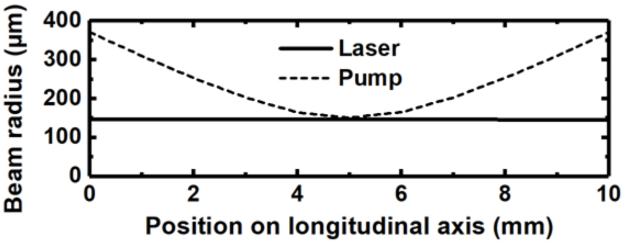

Figure 4-9: Comparative plot of the simulated (WinLase) $1/e^2$ beam radius of the laser in Figure 4-7 and the $1/e^2$ radius of the pump beam calculated from Equation 3-1 with $M^2 = 30$. Both plots are over the length of the Yb: KGW crystal.

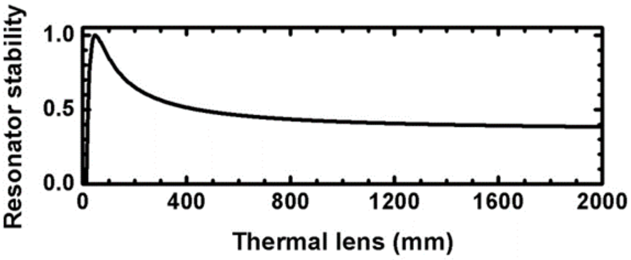

Figure 4-10: Simulated (WinLase) resonator stability against focal length of the thermal lens for the laser shown in Figure 4-7.

was not possible for the end-pumped laser with a curved end-mirror on the pump-side. The simulated effects of the thermal lens were therefore analysed for a large range of focal lengths to guarantee a stable resonator.

For a thermal lens of focal length between 100 mm and 2000 mm, the $1/e^2$ beam radius of the fundamental laser mode at the centre of the crystal was simulated to be between 118 µm and 154 µm. A plot of the $1/e^2$ beam radius at the centre of the crystal against the focal length of the thermal lens is shown in Figure 4-8. The laser beam radius was therefore comparable to the beam waist of the pump beam for the simulated thermal lensing. A comparison of the simulated $1/e^2$ laser beam radius to the calculated pump beam distribution over the length of the crystal is shown in Figure 4-9. With the actual thermal lens unknown, a thermal lens with focal length 600 mm was assumed as an example. The $1/e^2$ radius of the fundamental laser mode at the crystal facets was simulated to be 147 µm at the pump-side and 145 µm at the opposite side. The $1/e^2$ radius of the pump beam was fitted using Equation 3-1 for the distribution of a Gaussian beam with a M^2 of 30. Assuming the waist of the pump beam was at the centre of the crystal, the $1/e^2$ beam radius at the crystal facets was fitted to be 370 µm. This was considerably larger than that of the simulated intracavity laser beam. The implications of this mismatch are discussed later in Section 4.4. The resonator was simulated to be stable for thermal lens focal lengths between 15 mm and 2000 mm. The

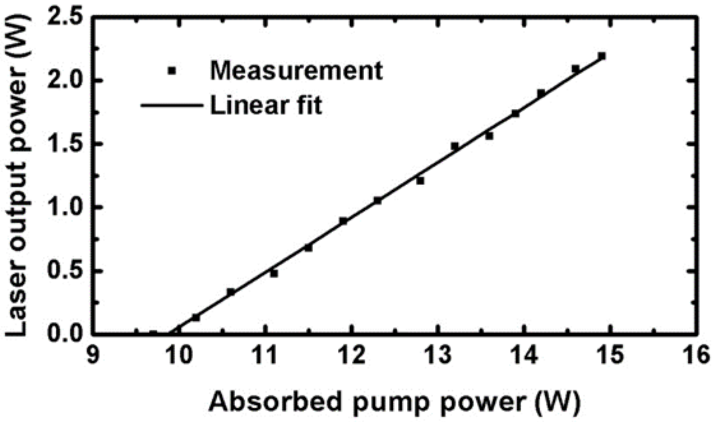

Figure 4-11: Plot of laser output power against absorbed pump power for the two-mirror laser shown in Figure 4-7.

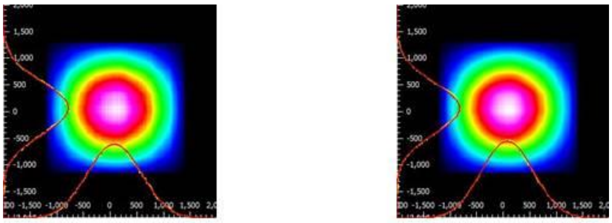
(a) (b)

Figure 4-12: Transverse mode profile of the laser output at powers of (a) 400 mW and (b) 2.19 W for the two-mirror laser shown in Figure 4-7.

resulting plot is shown in Figure 4-10, where a stability value of 0 indicates an unstable resonator.

The resonator was constructed around the Yb: KGW crystal. The centre of the crystal was positioned at the pump beam waist 46 mm from the second lens of the imaging system. The end-mirror on the pump-side was the bandpass mirror described in the Section 4.1.1, which had a ROC of 250 mm. The front surface of the mirror was positioned 8 mm from the pump-side end facet of the crystal. A flat output coupler with R ~ 80 % at both the pump and laser wavelengths was then positioned 11 mm from the opposite crystal facet. The CW threshold of the two-mirror laser was reached at an absorbed pump power of 9.8 W, corresponding to an output power of 16.0 W from the diode laser. The laser output power then rose linearly to 2.19 W when the absorbed pump power increased to 14.9 W, resulting in a slope efficiency of 43 %. This was measured using the Thorlabs 314C optical power meter and is shown in Figure 4-11. The residual pump light was filtered out using an edge filter with a sharp cut-off at λ = 1 µm.

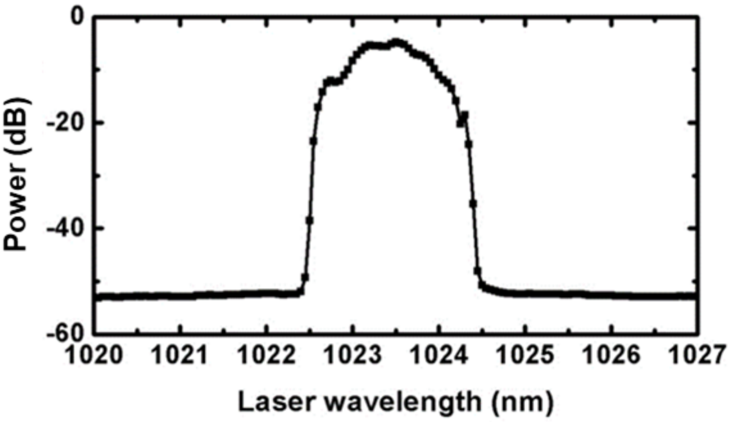

Figure 4-13: Measured optical spectrum of the laser output at a power of 2.19 W for the 2-mirror laser shown in Figure 4-7.

The transverse mode profile of the laser output was measured using a CCD camera 325 mm from the output coupler, with neutral density filters between to prevent damage to the camera. The measured transverse mode profiles at laser output powers of 400 mW and 2.19 W were observed to be TEM_{00} and are shown in Figure 4-12. The M^2 was measured by focusing the output beam using a lens of 100 mm focal length and measuring the beam width at multiple locations around the beam waist using the CCD camera. Distance intervals of 10 mm were used up to a maximum of 70 mm in either direction from the beam waist. The resulting beam distribution was then fitted to a Gaussian beam distribution defined by Equation 3-1. M^2 values of < 1.2 were measured at laser output powers of 400 mW and 2.19 W.

The optical spectrum of the laser output beam from the two-mirror laser was measured by fibre-coupling it to the OSA with a resolution bandwidth of 0.1 nm and a video bandwidth of 2 kHz. The edge filter with a sharp cut-off at $\lambda = 1$ µm was used to filter out residual pump light and a filter wheel was used to attenuate the beam. All measurements were therefore relative to the coupling efficiency and not absolute. At a laser output power of 2.19 W, the peak laser wavelength was measured to be 1023.5 nm with a FWHM linewidth of 0.7 nm. A plot of the OSA measurement is shown in Figure 4-13. The laser in all cases was linearly polarized on the horizontal axis (evaluated using a linear polarizer).

The resonator in Figure 4-7 was used to assess the emission spectrum of the Yb: KGW crystal. The crystal was pumped beneath the laser threshold and the amplified spontaneous emission was measured after the output coupler using the OSA. An edge filter with a sharp cut-off at $\lambda = 1000$ nm was positioned before OSA patch cable to filter out the residual pump

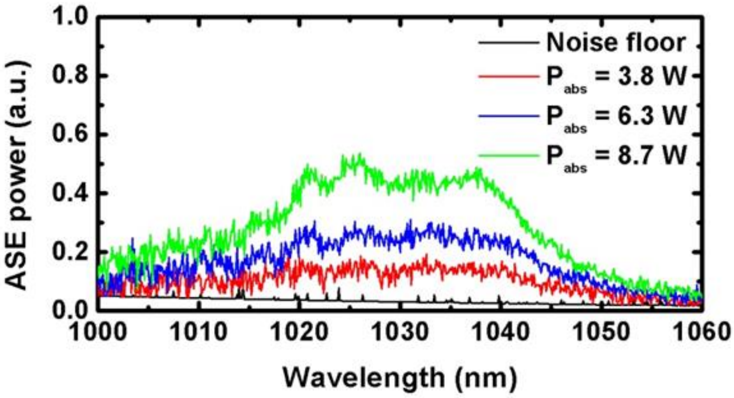

Figure 4-14: Measured optical spectrum of the amplified spontaneous emission (ASE) from the Yb: KGW crystal while being optically pumped at λ = 980 nm.

light. The resolution bandwidth of the OSA was set to 1 nm and the video bandwidth was set to 3 kHz. The resulting spectra at different pump powers are shown in Figure 4-14. The coupling efficiency was maintained for each measurement by not varying the alignment or position of any of the components. The intensity of the amplified spontaneous emission in each case plateaued between λ = 1020 nm & λ = 1038 nm and dropped to half-maximum at λ = 1015 nm & λ = 1043 nm. It was therefore predicted that the most efficient lasing would occur within the plateau region of the ASE spectrum.

4.1.3. Resonator design

The Littman configuration conventionally uses a diffraction grating and a flat end-mirror with tunable tilt angle to select the laser wavelength of minimum losses within the resonator (see Figure 1-4). The end-mirror is positioned at the first diffraction order of the grating, while the laser output beam originates from the zero diffraction order. In this work, the flat end-mirror was replaced with the gold-coated ET mirror characterised previously in Chapter 2. The circular mirror had a reflectance of 96 % at λ ~ 1 µm, a ROC of 50 mm and a diameter of 1.4 mm. The static tilt capability of the mirror could be used to select the laser wavelength of minimum losses within the resonator.

Experiments were first tried with a blazed diffraction grating combined with the ET mirror in both external-cavity and intracavity configurations. The Thorlabs GR25-0310 grating had 300 grooves/mm, was coated with aluminium and yielded a 1st order diffraction efficiency of 73%. However, these experiments were not successful due to several reasons which will be discussed further in Section 4.4. Instead, the ET mirror was combined with a dispersing

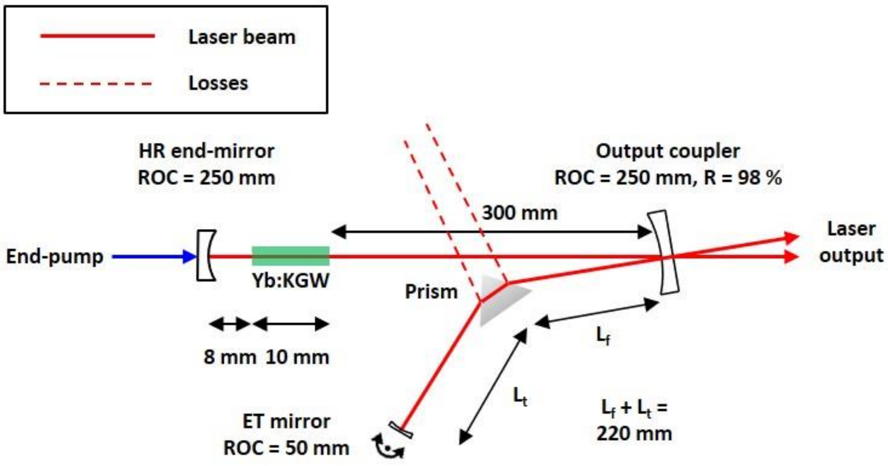

Figure 4-15: Schematic of the intracavity Yb: KGW laser with an equilateral dispersing prism combined with a MEMS mirror to select the wavelength of maximum gain within the resonator.

prism to select the wavelength of minimum losses within the resonator. The following resonator design only includes the intracavity implementation of the prism and the ET mirror.

The resonator was designed using the ABCD-matrix simulation tool WinLase. Various considerations had to be made during the design. Firstly, the intracavity beam had to be confined to the surface of the ET mirror, which was much smaller than conventional resonator mirrors. Secondly, the beam radius of the fundamental laser mode within the Yb: KGW crystal had to sufficiently match the pump beam. Thirdly, a proportion of the incident laser power would be absorbed within the bimorph structure of the gold-coated ET mirror, resulting in heating. This would cause the mirrors to deform through the different thermal expansion coefficients of the material layers. Lastly, since the thermal lens could not be measured, the resonator had to be stable for a large range of thermal lensing to guarantee that a stable resonator could be realised.

From these considerations, the resonator shown in Figure 4-15 was designed. The Yb: KGW crystal and the HR end-mirror on the pump-side were maintained from the two-mirror laser described in Section 4.1.2. A mirror with a ROC of 250 mm and a reflectance of 98 % at the pump & laser wavelengths was positioned 300 mm from the end-facet of the crystal at an angle of 5°. This mirror served as the laser output coupler and folded the intracavity beam through the prism and onto the ET mirror. The prism was made of SF11 glass, equilateral with a surface length of 20 mm, and angled near the Brewster angle to minimize the resonator losses. It was positioned a distance L_f from the folding mirror / output coupler. The

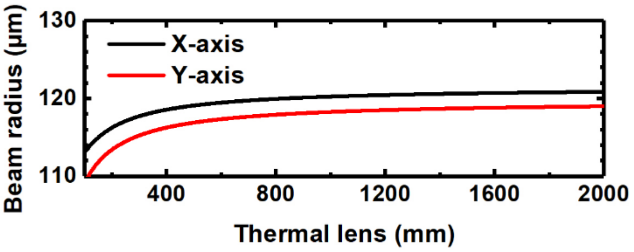

Figure 4-16: Plot of the simulated 1/e^2 beam radius of the fundamental laser mode at the centre of the Yb: KGW crystal against the focal length of the thermal lens for the resonator shown in Figure 4-15.

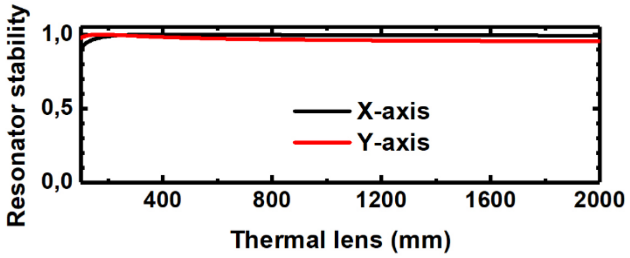

Figure 4-17: Plot of the resonator stability against focal length of the thermal lens for the resonator shown in Figure 4-15.

ET mirror was then positioned a distance L_t from the adjacent side of the prism. The combined distance of $L_f + L_t$ was 220 mm. The physical length of the resonator was therefore 548 mm, assuming the intracavity beam entered and exited the prism at the centre of the prism faces. Since the intracavity beam encountered the output coupler twice in a round trip, two output beams would occur. A similar effect would occur due to reflection from the faces of the prism.

The Yb: KGW crystal was simulated using two slabs with a length of 5 mm and a refractive index of 2, separated by a thin lens representing the thermal lensing effect. The resonator mirrors were then input with their respective values for ROC and tilt angle. The SF11 prism was simulated as a slab with a physical length of 10 mm and a refractive index of 1.7. To analyse the effect of the thermal lens on the resonator, focal lengths between 100 mm and 2000 mm were simulated. A plot of the 1/e^2 beam radius at the centre of the Yb: KGW crystal against the focal length of the thermal lens is shown in Figure 4-16. The 1/e^2 beam radius was simulated to be 117 ± 4 µm on the x-axis and 114 ± 5 µm on the y-axis over the range of thermal lenses. The resonator stability was simulated to be between 0.94 and 0.99 over the same range, as shown in Figure 4-17. This indicated that the thermal lens had little impact on the resonator. The simulated 1/e^2 beam radius for a thermal lens value of 600 mm

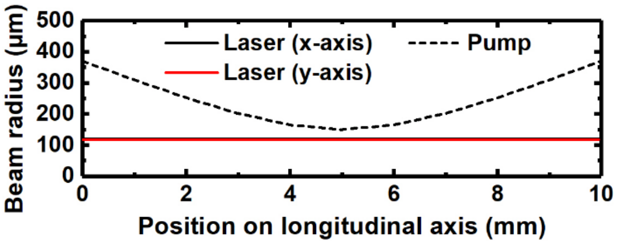

Figure 4-18: Plot of the simulated 1/e^2 beam radius of the fundamental laser mode and the pump beam over the length of the Yb: KGW crystal for the resonator shown in Figure 4-15.

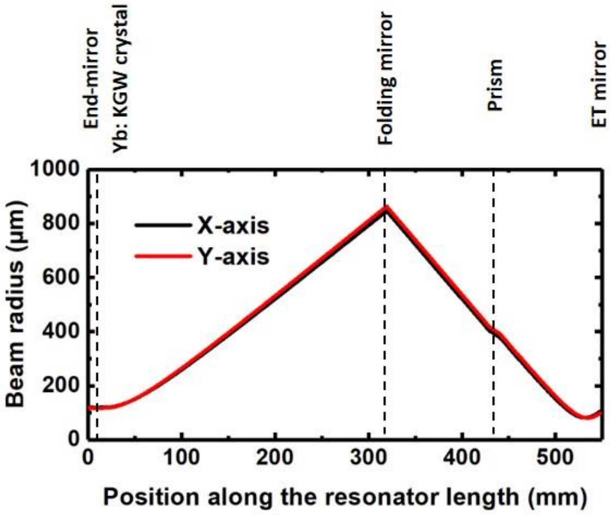

Figure 4-19: Plot of the simulated 1/e^2 beam radius of the fundamental laser mode over the length of the resonator shown in Figure 4-15.

was compared to the pump beam distribution within the crystal in the same way as for the two-mirror laser described in Section 4.1.2. The resulting plot is shown in Figure 4-18. Again, the pump beam at the crystal facets was considerably larger than that of the simulated intracavity laser beam.

A plot of the 1/e^2 radius of the intracavity beam radius over the length of the resonator for the same thermal lens value of 600 mm is shown in Figure 4-19. The resulting beam radius at the surface of the ET mirror was simulated to be 105 µm on the x-axis and 99 µm on the y-axis. This indicated that the beam was comfortably confined to the surface of the ET mirror. This proved consistent over all the performed simulations, showing that the diameter of the ET mirror was not an issue for the designed resonator.

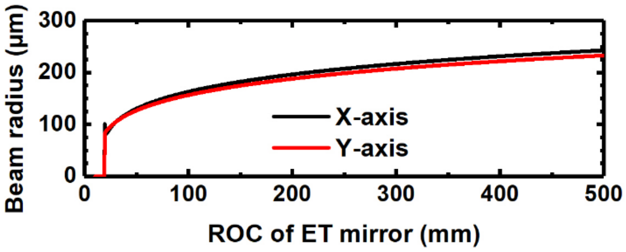

Figure 4-20: Plot of the simulated $1/e^2$ beam radius of the fundamental laser mode at the centre of the Yb: KGW crystal against the ROC of the ET mirror for the resonator shown in Figure 4-15.

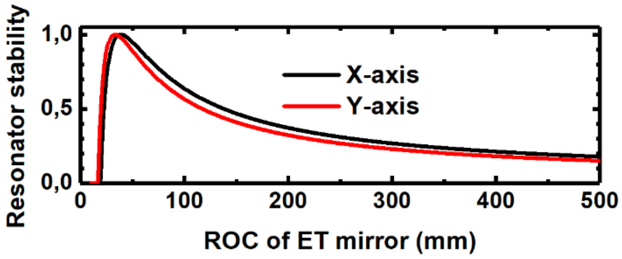

Figure 4-21: Plot of the simulated resonator stability against the ROC of the ET mirror for the resonator shown in Figure 4-15.

The simulation was then performed for a fixed thermal lens value of 600 mm and a ROC range of 10 mm to 500 mm for the ET mirror. The resulting plots of mirror ROC against the $1/e^2$ beam radius at the centre of the Yb: KGW crystal and the resonator stability are shown respectively in Figure 4-20 and Figure 4-21. The $1/e^2$ beam radius at the centre of the Yb: KGW crystal was observed to increase from ~ 84 µm at a ROC of 20 mm to ~ 230 µm at a ROC of 500 mm. The resonator became unstable at ROC's below 20 mm but was stable for the rest of the simulated range of mirror ROC's. Since the ROC of the ET mirror was expected to increase as it heated up, the stability was not expected to cause any issues for the proof-of-concept demonstration. The same could not be said however for the change in beam radius through the crystal. This had to be evaluated experimentally and is discussed later in this chapter.

4.2. Theoretical analysis

The fundamental theory behind wavelength tuning in this work is reliant on Snell's law of refraction. Light of different wavelengths is dispersed as it propagates through the prism, and the tilt angle of the ET mirror then selects which wavelength is optimally fed back through the resonator. To predict the output wavelength of the Yb: KGW laser shown previously in Figure 4-15, a geometrical optics model was constructed using MATLAB. The model simulated the direction of the intracavity beam as it interacted with each optical interface and computed the laser wavelength that was optimally fed back through the resonator. The following subsections discuss the construction of the model, the assumptions made and the simulation results. The impact of the laser dynamics on the performance of the laser is also discussed.

4.2.1. Geometrical optics model

The model was built using a MATLAB function (code shown in Appendix B). The model was purely geometrical and neglected the effects of the laser dynamics. The laser dynamics are discussed separately later in this section. Some assumptions were made to simplify the model. Firstly, the intracavity beam was simulated as a 1D line because the beam radius was irrelevant in simulating the direction of beam propagation. Secondly, only the prism and the ET mirror were included in the model because these had a direct impact on the laser output wavelength. The beam was assumed to be constant throughout the remainder of the resonator.

The model inputs included: the range of laser wavelengths to be simulated, the centre wavelength of the laser (highest gain), the prism parameters, the distance between the ET mirror & the prism and the curvature of the ET mirror. The model then computed the direction of beam propagation for each laser wavelength as it interacted with the prism and the mirror. The output of the model was then a list of laser wavelengths and the corresponding mirror tilt angle that resulted in an overlap between the incident and reflected beams of the mirror.

Model setup

The simulation first mapped the surface boundaries of the prism and the mirror. To align with experimental work described later in this chapter, the model was configured for an equilateral SF11 prism. The refractive index of the prism was calculated using the Sellmeier equation for SF11 [99], shown in Equation 4-1, where n is refractive index and λ is wavelength.

$$n^2 \text{-} 1 = \frac{1.73759695\,\lambda_0^2}{\lambda^2 - 0.013188707} + \frac{0.313747346\,\lambda_0^2}{\lambda^2 - 0.0623068142} + \frac{1.89878101\,\lambda_0^2}{\lambda^2 - 155.23629} \qquad \text{(Equation 4-1)}$$

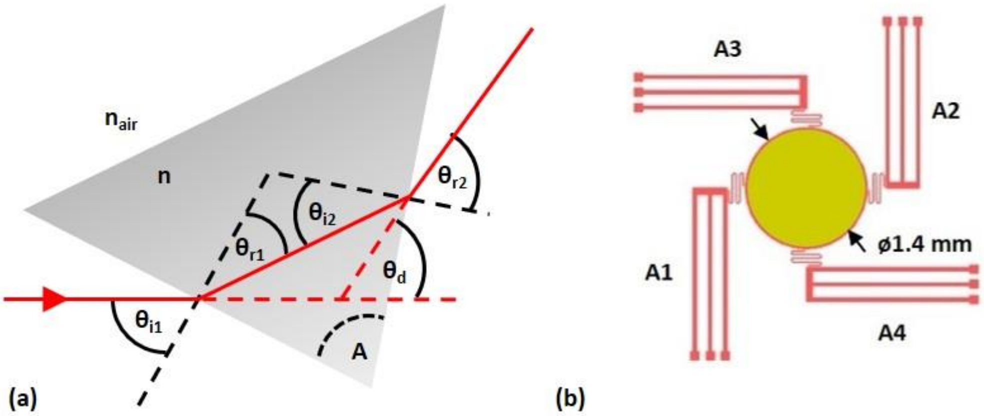

Figure 4-22: (a) Diagram of the prism orientation where $n_{air} = 1$ is the refractive index of air, n is the refractive index of the prism, θ_{i1} and θ_{i2} are the angles of incidence, θ_{r1} and θ_{r2} are the angles of refraction, θ_d is the angle of deviation and A is the apex angle. (b) Schematic of the ET mirror with labelled actuators A1 to A4.

The angle of incidence at prism entry, θ_{i1}, was fixed at that which resulted in the minimum angle of deviation, θ_d, for the beam at the centre wavelength, λ_0. This was also done to align with experimental work. With this fixed prism configuration, a beam of any wavelength could then be mapped through the prism using Snell's law and geometry to calculate the points at which the beam intersected the prism boundaries. An illustration of the prism boundaries and the mapped beam are shown in Figure 4-22a. The ET mirror was then mapped at a distance L_t from the prism exit point of the λ_0 beam at an angle of θ_d (referring to the resonator design in Figure 4-15). The mirror surface boundary was mapped as a circle segment with a radius equal to the ROC of the ET mirror (50 mm).

The simulated mirror surface boundary could be tilted in both clockwise and anti-clockwise directions. Recall from Chapter 2 that the ET mirror had four radially positioned actuators labelled A1 to A4, as shown in Figure 4-22b. Only two actuators were necessary for this work because the wavelength tuning was performed on one axis only. In the later described experimental work, actuators A1 and A2 were used since these coincided with the dispersive axis of the prism. In the simulation, activating actuator A1 resulted in anti-clockwise tilt of the mirror and a negative tilt angle. Activating actuator A2 resulted in clockwise tilt of the mirror and a positive tilt angle. After mapping the tilted mirror surface boundary, the point of intersection between the incident beam and the mirror was calculated. The angle of incidence and the angle of reflection for the beam at the mirror surface were then calculated.

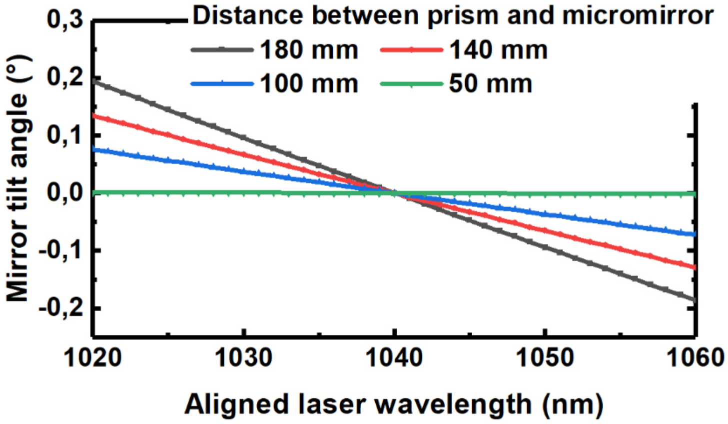

Figure 4-23: Simulated laser wavelength against mirror tilt angle at distance of L_t = 50 mm, 100 mm, 140 mm and 180 mm between the prism and the ET mirror.

The results of the model were computed using an iterative solution of the above setup. At each laser wavelength, the beam was mapped through the prism and reflected by the ET mirror. The ET mirror was tilted in steps of 0.001 ° until the angle of reflection for the beam at the ET mirror was equal to the angle of incidence. The corresponding tilt angle was then stored alongside the laser wavelength to indicate the mirror tilt angle at which the resonator was optimally aligned.

Results

The simulation was configured to compute the mirror tilt angle at which resonator alignment occurred for laser wavelengths between λ = 1020 nm and λ = 1060 nm (the gain bandwidth of Yb: KGW). Steps of 1 nm were used and the centre wavelength to map the prism and mirror surface boundaries was set to λ_0 = 1040 nm. The above setup was used at distances of L_t = 50 mm, 100 mm, 140 mm and 180 mm between the prism and the ET mirror. The results of the simulation are shown in Figure 4-23.

The mirror tilt angle required for a laser output wavelength of 1040 nm was simulated to be 0 ° for all values of L_t, which was expected because this was the centre wavelength. At L_t = 180 mm, the mirror tilt angle required for laser output wavelengths of 1020 nm and 1060 nm was simulated to be 0.194 ° and -0.186 ° respectively. As the value of L_t was decreased, the mirror tilt angle to achieve the same laser wavelengths decreased towards ± 0.001 ° at L_t = 50 mm. This decrease was a result of the curved mirror surface. At L_t = 50 mm, the prism was located at the centre of curvature of the ET mirror surface. All laser wavelengths were simulated to be simultaneously in resonator alignment. Laser wavelength tuning would theoretically be prohibited in the case that all laser wavelengths were simultaneously in resonator alignment because the laser wavelength of maximum net gain would dominate regardless of the mirror tilt angle. To achieve laser wavelength tuning, the prism must be positioned away from this position.

As the distance between the prism and the ET mirror was increased from 50 mm, the beams at laser wavelengths of 1020 nm and 1060 nm were simulated to shift further towards the edges of the ET mirror. Considering a $1/e^2$ beam radius of 117 μm at the ET mirror, the edge of a $\lambda = 1020$ nm beam would extend beyond the edge of the mirror at $L_t = 450$ mm. At $\lambda = 1060$ nm, this would occur at $L_t = 470$ mm. Both distances are longer than the distance $L_f + L_t = 220$ mm defined by the resonator design. It was therefore predicted that all laser wavelengths supported by Yb: KGW would be confined to the surface of the ET mirror for the designed resonator. At $L_t = 180$ mm, the minimum and maximum laser wavelengths that were fully confined to the mirror surface were simulated to be $\lambda = 992$ nm and $\lambda = 1093$ nm.

The same simulations were computed for a flat mirror in the place of the curved ET mirror. In this case, the mirror tilt angles required for laser wavelengths of 1020 nm and 1060 nm were -0.074 ° and 0.071 ° respectively for all values of L_t. The direction of tilt required for the upper and lower wavelengths was reversed from the case of the curved mirror. This occurred because, in the case of the curved mirror, the value of L_t was larger than the ROC of the mirror, meaning that the prism was positioned beyond the focal point.

4.2.2. Other considerations

While the MATLAB model provided a purely geometrical analysis of the laser wavelength as the ET mirror was tilted, the theoretical analysis would not be complete without considering the laser dynamics. Such aspects as the laser threshold condition and the laser output power could not be estimated because the gain cross-section of the Yb: KGW crystal could not be quantified experimentally. Nevertheless, the gain cross-section of the crystal and its impact on the tunable laser wavelength can still be explained hypothetically.

The laser wavelength is mostly influenced by two factors: the resonator losses and the effective gain cross-section of the Yb: KGW crystal. The resonator losses are controlled by the prism and the ET mirror as described previously. The effective gain cross-section of the crystal is wavelength dependent, and thus each discrete laser wavelength requires a different pumping intensity to achieve laser threshold. The gain cross-section was also reported in

[100] to shift when the intensity of optical pumping was changed, which was thought to be a result of reabsorption. The resonator losses and the gain cross-section combined will therefore depict the laser wavelength.

Consider the case where the prism was positioned at the centre of curvature of the ET mirror, resulting in all laser wavelengths being simultaneously in resonator alignment. The resonator losses will therefore be uniform across the range of laser wavelengths, meaning the laser wavelength is dependent only on the gain cross-section. Laser wavelength tuning using a MEMS mirror would therefore be infeasible. However, consider the case where the resonator losses are not uniform across the range of laser wavelengths and in fact yield an inverted Gaussian profile. Tilting of the ET mirror then results in the peak transmitted wavelength shifting across the spectrum. With a steep rise in losses on either side of the transmitted wavelength, the laser wavelength will follow the resonator losses until the pump intensity becomes insufficient to sustain lasing. With a slow rise in losses on either side of the transmitted wavelength, the laser wavelength will depend on whether the resonator losses are enough to overcome the gain cross-section of the crystal.

Considering the hypothetical analysis above, a threshold must exist at which point the resonator losses dominate over the gain cross-section. The losses of the resonator in this work are dependent on the curvature of the ET mirror, the dispersive power of the prism and the proximity of the prism to the centre of curvature of the ET mirror. The threshold is evaluated experimentally in the following section.

4.3. Experimental characterisation

The resonator shown in Figure 4-15 was constructed around the Yb: KGW crystal described in Section 4.1.2. The first experiment investigated the impact of the curved mirror surface on the wavelength tunability in a similar manner to the theoretical analysis in Section 4.2, where the distance between the prism and the ET mirror, L_t, was varied. The second experiment then fully characterized the tunable Yb: KGW laser in a fixed configuration to give the optimum tuning conditions.

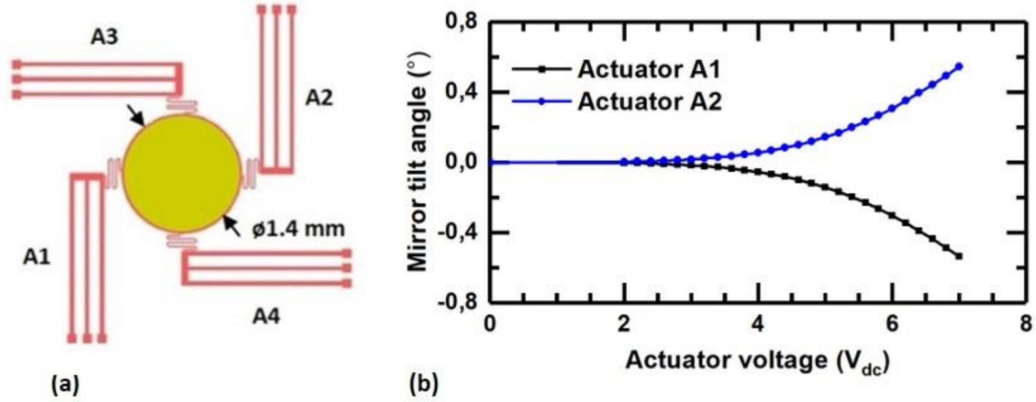

Figure 4-24: (a) Schematic of the ET mirror with labelled actuators A1 to A4. (b) Plot showing the tilt angle of the ET mirror against voltage applied to actuators A1 and A2.

4.3.1. ET mirror

The ET mirror was initially characterized in Chapter 2 and was shown to achieve a mirror tilt angle of 1.33° for an actuator voltage of 10 V. From the results of the geometrical optics model in Section 4.2.1, it was anticipated that only small tilt angles were required to tune the laser wavelength (< 0.2°). The ET mirror was therefore experimentally characterized at very small tilt angles prior to using it in the laser.

The later described laser wavelength tuning was performed using actuators A1 and A2 (see Figure 4-24a). These actuators tilted the ET mirror on the dispersive axis of the prism and were therefore characterized. The mirror tilt angle was measured for actuator voltages between 0 V and 7 V in steps of 0.2 V. The measurements were made by directing the beam from a HeNe laser towards the centre of the ET mirror and reflecting it onto a CCD camera 60 mm from the mirror. The CCD camera then measured the transverse mode profile of the reflected HeNe beam. The point of highest optical intensity was recorded at each actuator voltage and was used to calculate the mirror tilt angle.

The resulting plot of mirror tilt angle against actuator voltage is shown in Figure 4-24b, where negative tilt is anticlockwise and positive tilt is clockwise to align with the setup of the geometrical optics model. The lowest measurable tilt angle was recorded to be ± 0.003 ° for an actuator voltage of 2 V. The mirror tilt angle then rose nonlinearly to a value of -0.537 ° with 7 V applied to actuator A1 and 0.543 ° with 7 V applied to actuator A2. The geometrical optics model predicted that a mirror tilt angle of 0.194 ° would be required to tune the laser wavelength from the centre wavelength to the maximum and minimum wavelengths supported by Yb: KGW. Mirror tilt angles of ± 0.197 ° were measured at an actuator voltage of 5.4 V.

4.3.2. Verification of the theoretical analysis

The geometrical optics model indicated that the curved surface of the ET mirror affected the mirror tilt angle required to achieve a discrete laser wavelength. The hypothetical analysis of the laser dynamics then predicted that the laser wavelength was dependent on both the mirror tilt angle and the gain cross-section of the Yb: KGW crystal. To investigate this, four resonator configurations were investigated with different distances between the prism and the ET mirror (L_t). The four values of L_t were 40 mm, 75 mm, 110 mm and 180 mm. The respective values of L_f were then 180 mm, 145 mm, 110 mm and 40 mm, satisfying the condition $L_t + L_f = 220$ mm defined by the resonator design.

At each value of L_t, the laser was aligned using the short two-mirror laser built around the same Yb: KGW crystal as a reference (described in Section 4.1.2). Firstly, the folding mirror / output coupler was inserted into the beam path 300 mm from the end facet of the Yb: KGW crystal at an angle of 5 °. The equilateral SF11 prism was then inserted into the reflected beam path, with a distance L_f between the folding mirror and the point at which the reflected beam entered the prism. The prism was mounted on a rotational stage and was rotated until the minimum angle of deviation for the beam occurred. This was done to maintain a constant angle of incidence to the prism as L_t was changed. The ET mirror was then positioned at a distance L_t from the point at which the beam exited the prism, with the beam striking the centre of the mirror. The angle of the ET mirror was then adjusted until the reflected beam propagated back through the resonator, forming an external cavity to the short two-mirror laser. The output coupler of the two-mirror laser was then removed, leaving a fully intracavity laser including the prism, the ET mirror and the folding mirror / output coupler.

The minimum laser threshold for each resonator configuration was reached at an absorbed pump power of 7.8 ± 0.2 W. Two output beams were emitted from the output coupler due to a double pass during a roundtrip of the resonator. One beam was emitted from the direction of the crystal and the other was emitted from the direction of the prism. The characteristics of these beams were measured to be similar. The optical spectrum of the laser output just above laser threshold was measured by fibre-coupling one of the beams into an OSA configured with a resolution bandwidth of 0.1 nm and a video bandwidth of 2 kHz. An edge

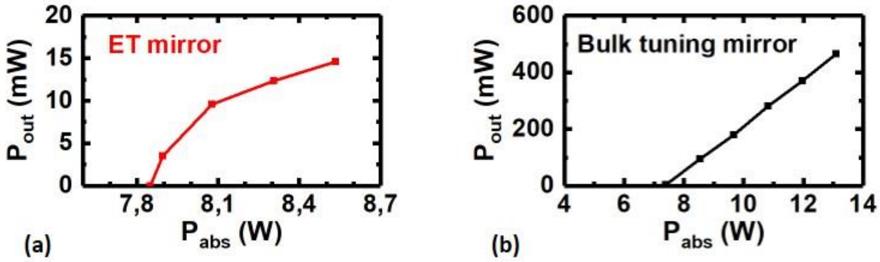

Figure 4-25: Plots showing the laser output power P_{out} against absorbed pump power P_{abs} at λ_0 and L_t = 180 mm for use of (a) the ET mirror and (b) a bulk tuning mirror.

filter was used prior to fibre-coupling to filter out the residual pump light. The peak laser wavelength was measured to be λ_0 = 1028.4 ± 0.4 nm for all values of L_t, which was then considered to be the centre wavelength of the laser.

The laser output power, P_{out}, was limited to 15 mW to prevent damage to the surface of the ET mirror. It was discovered in previous experiments that laser output powers approaching 25 mW resulted in damage to the gold coating due to laser heating. Figure 4-25a shows a plot of the laser output power at λ_0 against absorbed pump power, P_{abs}, in the case of L_t = 180 mm. The laser output power was observed to rise nonlinearly to P_{out} = 14.6 mW at P_{abs} = 8.5 W. This was expected to be the result of a change in surface curvature of the ET mirror, which was simulated in Section 4.1.3 to have an impact on the intracavity beam radius through the Yb: KGW crystal.

To confirm that thermally induced curvature change was the cause of the nonlinear rise in laser output power, the laser was further assessed by comparing use of the ET mirror to use of a bulk mirror. The bulk mirror was a dielectric coated BK7 mirror with a ROC of 50 mm and a reflectance of 98 % between λ = 1020 nm and λ = 1060 nm. This bulk mirror was chosen because it yielded similar properties to the ET mirror, which had a ROC of 50 mm and a reflectance of 96 %. The mirror was inserted into the resonator in an identical manner to the ET mirror at L_t = 180 mm. The minimum laser threshold was reached at P_{abs} = 7.3 W. This was lower than the laser threshold when using the ET mirror because of the higher reflectance of the bulk mirror. The centre wavelength of the laser in this case was measured using the OSA to be λ_0 = 1028.5 nm. A plot of the laser output power at λ_0 against absorbed pump power is shown in Figure 4-25b. A linear relationship was measured with a slope efficiency of 8.0 %, leading to a maximum laser output power of 465 mW at P_{abs} = 13.1 W. This showed that a linear power efficiency was possible when using a mirror with fixed curvature.

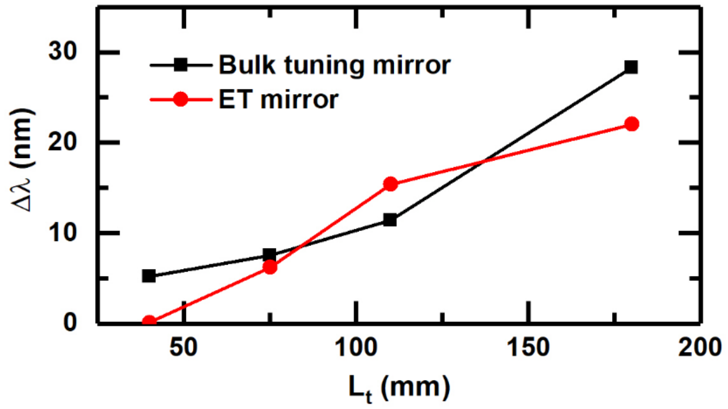

Figure 4-26: Plot showing the maximum wavelength range of the laser, Δλ, at different values of L_t when using the ET mirror and the bulk tuning mirror.

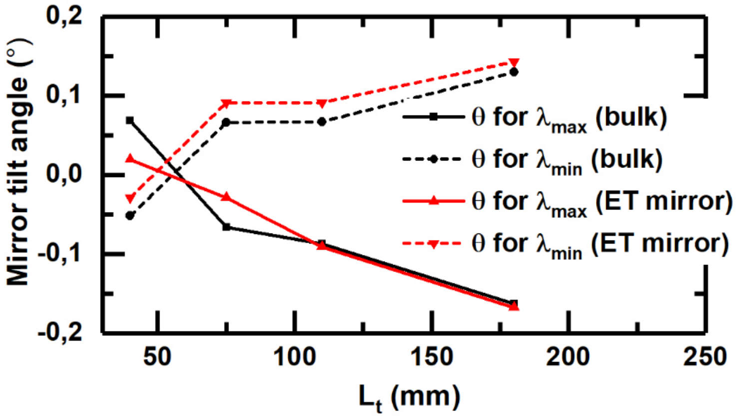

Figure 4-27: Plot showing the mirror tilt angle required to achieve the maximum and minimum laser wavelengths for the ET mirror and the bulk mirror at different values of L_t.

For each value of L_t, the maximum wavelength range of the laser was evaluated for use of the ET mirror and the bulk tuning mirror at an absorbed pump power of 13.1 W. With the ET mirror, tuning was enabled by applying a voltage to either actuator A1 or A2, resulting in mirror tilt on the dispersive axis of the prism. To prevent damage to the surface of the ET mirror due to excess laser power, the pump power was only increased after increasing the voltage applied to the ET actuator until the resonator losses became too large to sustain lasing. This was done iteratively until the absorbed pump power was 13.1 W. With the bulk mirror, tuning was enabled by tilting the mirror mount on the dispersive axis of the prism. The tilt angle of the mirror was monitored by directing a HeNe beam towards the backside of the mirror and reflecting it towards a screen 2.1 m from the mirror. The optical spectrum of the laser output for each configuration was continuously monitored using the OSA configured with a resolution bandwidth of 0.1 nm and a video bandwidth of 2 kHz.

A plot showing the range of achievable wavelengths at each value of L_t for use of the ET mirror and use of the bulk tuning mirror is shown in Figure 4-26. For both mirrors it was observed that the achievable wavelength range increased as L_t was increased. In the cases of L_t = 40 mm, 75 mm and 110 mm, continuous wavelength tuning was not possible over the full range of laser wavelengths. The laser wavelength was observed to hop as the mirror was tilted when using the ET mirror and when using the bulk mirror. This indicated that tuning the resonator losses was not enough to overcome the gain cross-section of the Yb: KGW crystal. In the case of L_t = 180 mm, continuous tuning was observed over a range of 22 nm using the ET mirror and 28 nm using the bulk mirror.

The mirror tilt angles required to achieve the maximum and minimum wavelengths for each resonator configuration at an absorbed pump power of 13.1 W are shown in Figure 4-27. In all cases, an increasing trend in the required tilt angle was observed as L_t was increased from 75 mm to 180 mm. For example, when using the ET mirror the mirror tilt angle to achieve λ_{min} was -0.03 ° at L_t = 75 mm and -0.17 ° at L_t = 180 mm. The mirror tilt angle to achieve λ_{max} was 0.09 ° at L_t = 75 mm and 0.14 ° at L_t = 180 mm. At L_t = 40 mm, the mirror tilt angle to increase or decrease the laser wavelength was reversed. The mirror tilt angle to achieve λ_{min} and λ_{max} was then 0.02 ° and -0.03 ° respectively. The reversal of the mirror tilt angle was a result of the prism being positioned on the opposite side of the centre of curvature of the ET mirror.

The above described trends are consistent with the trends observed in the results of the geometrical optics model reported in Section 4.2.1. With L_t = 180 mm between the prism and the ET mirror, continuous tuning of the laser wavelength was possible while at smaller distances the tuning showed hopping between wavelengths. This indicated that the tuning of the resonator losses dominated over the gain cross-section of the Yb: KGW crystal at L_t = 180 mm, but not at the smaller distances. It could therefore be concluded that the optimum conditions for wavelength tuning with the designed resonator occurred at L_t = 180 mm. This was the maximum distance that was spatially possible between the prism and the ET mirror for the designed resonator.

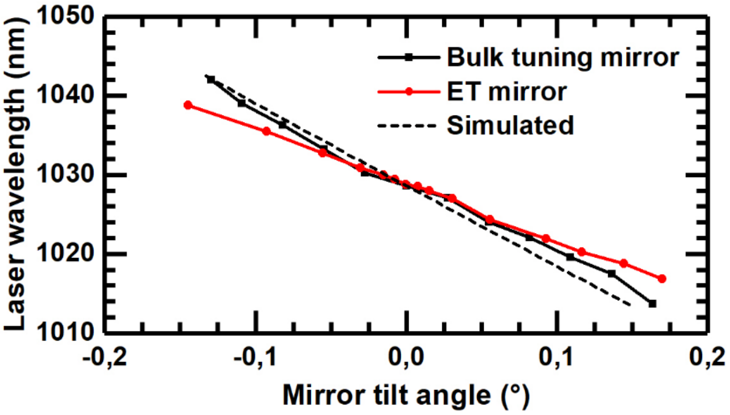

Figure 4-28: Plot showing the laser output wavelength against mirror tilt angle for the ET mirror and the bulk tuning mirror. The experimental response is compared to the simulated results.

4.3.3. Continuous wavelength tuning

For the optimized condition of L_t = 180 mm, the peak laser wavelength was measured using the OSA for both the ET mirror and the bulk tuning mirror as they were tilted. As each respective mirror was tilted and the laser wavelength shifted, the laser output power and the laser threshold also changed. For this part of the investigation, the laser output power when using the ET mirror was kept constant at 10 mW by adjusting the pump power at each measurement. This ensured that the ET mirror was not damaged from excess laser heating.

A plot of the laser wavelength against mirror tilt angle when using the ET mirror and when using the bulk tuning mirror is shown in Figure 4-28. When using the ET mirror, the centre wavelength of the laser was measured to be λ_0 = 1028.8 nm at an absorbed pump power of 8.1 W. The voltage applied to actuator A1 was then increased from 0 V towards 5 V, resulting in the mirror tilt angle changing from 0° to -0.14°. This resulted in the peak laser wavelength shifting upwards to λ_{max} = 1038.8 nm at an absorbed pump power of 13.1 W. At this point, optical pumping became insufficient to maintain a laser output power of 10 mW. The voltage applied to actuator A1 was then returned to 0 V while iteratively adjusting the pump power to avoid damaging the ET mirror. The voltage applied to actuator A2 was then increased from 0 V towards 5.2 V, resulting in the mirror tilt angle changing from 0° towards 0.17°. This resulted in the peak laser wavelength shifting downwards to λ_{min} = 1016.8 nm at an absorbed pump power of 13.1 W. Again, the laser output power dropped below 10 mW at this point. A plot showing the measured optical spectra at various

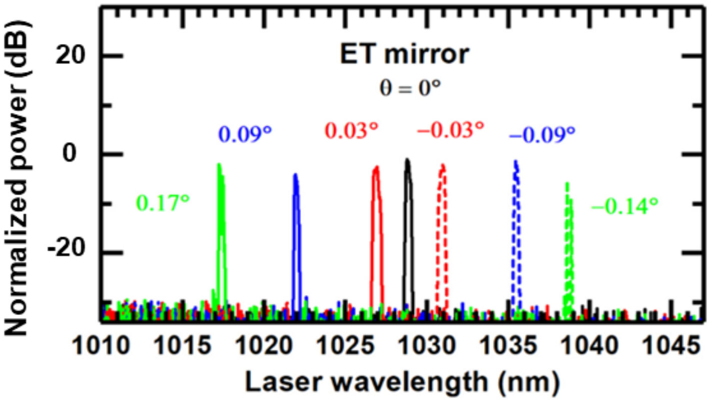

Figure 4-29: Plot showing the optical spectrum of the laser output as the tilt angle of the ET mirror was varied. The laser output power was constant at 10 mW for each measurement.

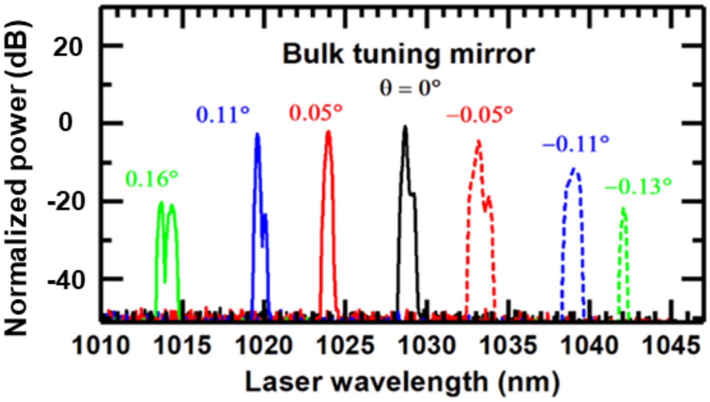

Figure 4-30: Plot showing the optical spectrum of the laser output as the tilt angle of the ET mirror was varied. The absorbed pump power was held constant at 13.1 W.

mirror tilt angles is shown in Figure 4-29. The power in this plot is relative to the coupling efficiency of the OSA which changed for each reading, thus the power has been normalized to 0 dB. The spectral linewidth (FWHM) of the laser output was measured to be < 0.25 nm for all measurements, with measurement accuracy limited by the sampling resolution of the OSA.

When using the bulk mirror, the centre wavelength of the laser was measured to be λ_0 = 1028.5 nm at an absorbed pump power of 7.4 W. The mirror was then tilted clockwise towards a mirror tilt angle of 0.16°, resulting in the peak laser wavelength shifting downwards to 1013.7 nm at an absorbed pump power of 13.1 W. The laser output power dropped below 10 mW at this point. The mirror was then tilted anti-clockwise towards a

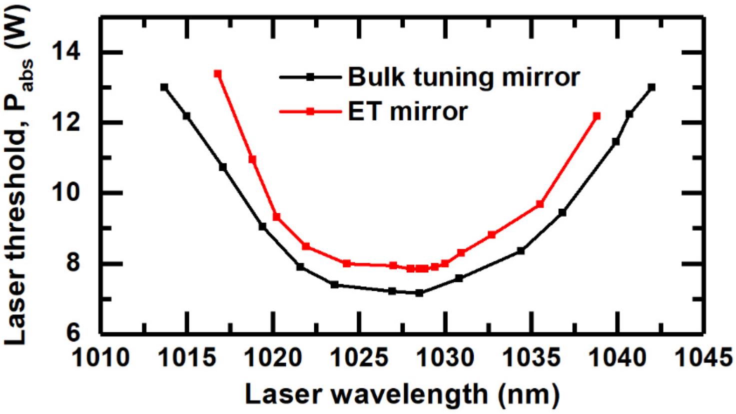

Figure 4-31: Plot showing the optical spectrum of the laser output as the tilt angle of the ET mirror was varied. The absorbed pump power was held constant at 13.1 W.

mirror tilt angle of -0.13°, resulting in the peak laser wavelength shifting upwards to 1042.0 nm at an absorbed pump power of 13.1 W. The laser output power dropped below 10 mW at this point. A plot showing the measured optical spectra at various mirror tilt angles with a constant absorbed pump power of 13.1 W is shown in Figure 4-30. The power in this plot has been normalized to 0 dB since the coupling efficiency changed for each measurement. The FWHM linewidth was measured to be < 0.31 nm for all measurements except for the laser output at a mirror tilt angle of -0.16°, which yielded a double wavelength peak.

The experimental results were compared to simulated results from the geometrical optics model. The model was configured for the centre wavelength of 1028.8 nm, L_t = 180 mm and a mirror ROC of 50 mm. The laser wavelength was simulated to be 1013.8 nm at a mirror tilt angle of 0.15° and 1042.8 nm at a mirror tilt angle of -0.13°. The experimental results provided a very good match to the simulated results, as shown in Figure 4-28.

The absorbed pump power required to reach laser threshold varied with laser wavelength. This was due to the non-uniform gain cross-section of Yb: KGW over the range of laser wavelengths. A plot of the laser threshold against laser wavelength is shown in Figure 4-31. When using the ET mirror, the laser threshold was reached at $P_{abs} = 7.8$ W for $\lambda_0 = 1028.8$ nm. The laser threshold then increased to $P_{abs} = 13.1$ W and $P_{abs} = 12.1$ W for $\lambda_{min} = 1016.8$ nm and $\lambda_{max} = 1038.8$ nm respectively. When using the bulk tuning mirror, the laser threshold was reached at $P_{abs} = 7.3$ W for $\lambda_0 = 1028.5$ nm. It then increased to $P_{abs} = 13.0$ W for both $\lambda_{min} = 1013.7$ nm and $\lambda_{max} = 1042.0$ nm. The difference in laser

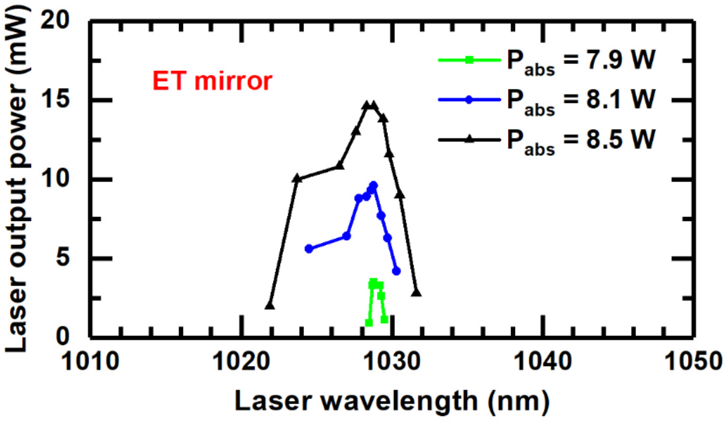

Figure 4-32: Plot showing the optical spectrum of the laser output as the tilt angle of the ET mirror was varied. The absorbed pump power was held constant at 13.1 W.

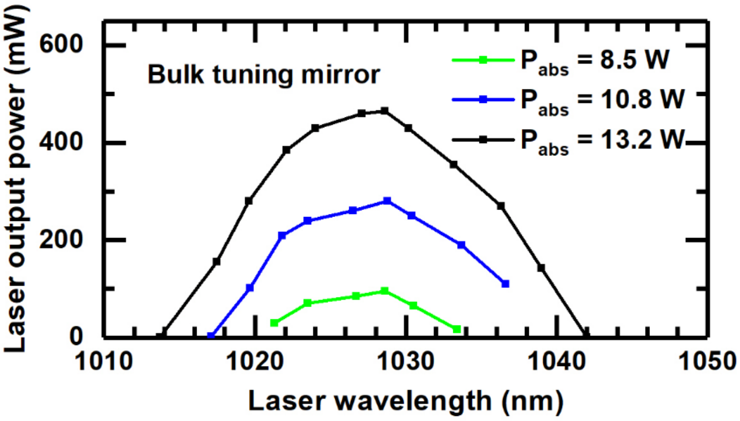

Figure 4-33: Plot showing the optical spectrum of the laser output as the tilt angle of the ET mirror was varied. The absorbed pump power was held constant at 13.1 W.

threshold between use of the ET mirror and use of the bulk mirror was caused by the difference in mirror reflectance.

The variation in laser threshold resulted in a certain range of laser wavelengths for a constant pump power. A plot showing the laser output power against wavelength at various absorbed pump powers is shown in Figure 4-32 for the ET mirror and Figure 4-33 for the bulk tuning mirror. When using the ET mirror, the tunable wavelength range was 1 nm at P_{abs} = 7.9 W, 5.9 nm at P_{abs} = 8.1 W and 9.7 nm at P_{abs} = 8.5 W. The laser output power could not be evaluated at higher absorbed pump powers due to the limit on laser output power. When using the bulk tuning mirror, the tunable wavelength range was 12.1 nm at P_{abs} = 8.5 W, 19.5 nm at P_{abs} = 10.8 W and 28.3 nm at P_{abs} = 13.1 W. According to Figure 4-31, the

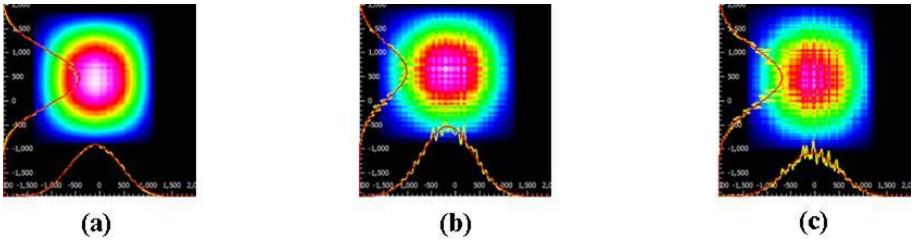
(a) (b) (c)

Figure 4-34: Images of the transverse mode profile of the laser output at laser wavelengths of (a) 1028.8 nm, (b) 1024.3 nm and (c) 1030.9 nm when using the ET mirror for wavelength tuning. The laser output power was 10 mW.

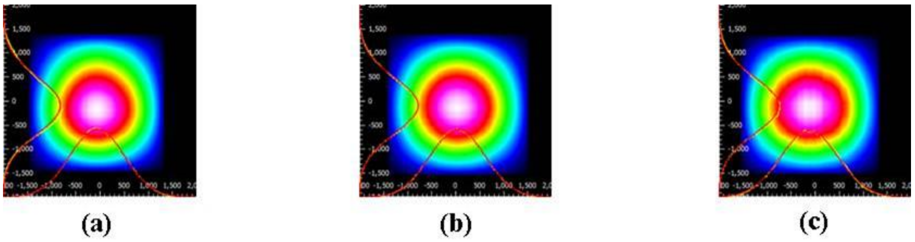
(a) (b) (c)

Figure 4-35: Images of the transverse mode profile of the laser output at laser wavelengths of (a) 1028.5 nm, (b) 1017.5 nm and (c) 1039.0 nm when using the bulk tuning mirror. The laser output power was 30 mW.

tunable wavelength range for using the ET mirror was estimated to be 10 nm, 18 nm and 22 nm at the same respectively values of P_{abs}.

Spatial analysis of the laser output

The M^2 beam divergence rate of the laser output was measured by focusing the output beam using a lens of 100 mm focal length and measuring the beam width at multiple locations around the beam waist using the Thorlabs BP104-IR beam profiler. Distance intervals of 10 mm were used up to a maximum of 70 mm in either direction from the beam waist. The resulting beam distribution was then fitted to a Gaussian beam distribution defined by Equation 3-1. When using the ET mirror, the M^2 was calculated to be 2.0 over the range of laser wavelengths on both the x-axis and the y-axis at a laser output power of 10 mW. Using the bulk mirror, the M^2 was measured to be < 1.2 over the range of laser wavelengths at a laser output power of 30 mW. The reason for the difference in divergence rate when using the bulk tuning mirror instead of the ET mirror is unknown.

When using the ET mirror, the transverse mode profile of the laser output was measured using the beam profiler 50 mm from the output coupler. The resulting images at laser wavelengths of 1028.8 nm, 1024.3 nm and 1030.9 nm are shown in Figure 4-34, all of which show a TEM_{00} profile. When using the bulk tuning mirror, the transverse mode profile of the laser output was measured using the beam profiler 75 mm from the output coupler. The resulting images at laser wavelengths of 1028.5 nm, 1017.5 nm and 1039.0 nm are shown in Figure 4-35, all of which show a TEM_{00} profile.

4.4. Discussion

A proof-of-concept investigation of a wavelength tunable Yb: KGW laser has been reported, where wavelength tuning was enabled by the intracavity combination of a prism and a MEMS mirror. A geometrical optics model was developed to simulate the laser wavelength at which the least resonator losses occurred and showed a close comparison to the experimental results. For the optimized resonator design, continuous wavelength tuning was yielded over a range of 22 nm between 1016.8 nm and 1038.8 nm with FWHM linewidths of less than 0.25 nm.

The laser output power was limited to 10 mW to prevent damage to the surface of the gold-coated ET mirror. Alike the work in Chapter 3, the performance of the tunable laser could be improved by depositing a multi-layer dielectric coating on the surface of the mirror. This would then enable scaling of the laser output power. In the case that the coated mirror surface is flat, this would also enable a simpler resonator design because the tuning capabilities of the laser would not be dependent on the focal point of the mirror. Such a coating has yet to be developed for a MEMS mirror. Further power-scaling could also be achieved by optimizing the overlap between the pump beam and the laser beam. This was not done for this work due to time constraints and difficulty in setting up the end-pumped laser.

The initial plan for this work was to use a diffraction grating in the Littman configuration instead of a prism. Diffraction gratings have a higher dispersive power than prisms, thus resulting in a narrower transmission linewidth within the resonator. Using a grating was possible in an external cavity configuration but was not possible to implement in an intracavity configuration because the grating losses were too high to sustain lasing at the maximum pump power. External cavity configurations were investigated for the use of both a grating and a prism but were halted due to a phenomenon which caused the laser efficiency to be permanently reduced. The root cause for the phenomenon was not found. Initial investigations showed that external cavity configurations yielded a lower laser threshold and a larger range of tunable wavelength, but at the expense of a much wider spectral linewidth.

The SF11 prism was orientated for all laser assemblies such that the laser beam traversed the prism at the minimum angle of deviation, providing a simple and consistent method for laser alignment. This orientation was not precisely at the Brewster angle of SF11 because the prism was equilateral, thus resulting in a different angle of incidence at opposite sides of the prism. The use of a Brewster angle dispersing prism instead of an equilateral prism would have enabled the resonator losses to be minimized. A short investigation was undertaken to determine the effects of different prism orientations on the tunable laser performance. In the intracavity configuration, laser action was only achieved within a range of ± 2 ° of the angle of incidence resulting in the minimum angle of deviation. At the extremes, the beam quality was significantly diminished, leading to a drastic increase in laser threshold and a reduction in the tunable wavelength range. This was most likely a result of aberration introduced by the double pass of the prism during a roundtrip of the resonator.

Different prism materials were also investigated to assess the impact of dispersive power on the tunable laser performance. Equilateral prisms made of BK7 and F2 glass were used in the optimized resonator design where the distance between the prism and the ET mirror was 180 mm. The dispersive power of these prisms was lower than that of SF11, meaning that the spatial separation of light with different wavelengths was smaller. Continuous wavelength tuning in both cases was not possible, with the only changes in laser wavelength being hops between discrete wavelengths. The dispersive power of the prisms was therefore not enough for the resonator losses to overcome the gain cross-section of the Yb: KGW crystal.

Despite the described limitations, a successful proof-of-concept has been reported for a solid-state laser with tunable wavelength enabled by the intracavity combination of a prism and a MEMS mirror. With improvements to the MEMS mirror coating and the resonator design, the laser could be power scaled, the resonator design could be simplified, and the tunable wavelength range could be improved. This technique is applicable to any solid-state laser operating in any region of the optical spectrum.

5. Q-switched Yb: KGW laser with tunable wavelength

In previous chapters, Q-switching and wavelength tuning of solid-state lasers enabled by the actuation of MEMS mirrors was reported. Q-switching of a Nd: YAG laser enabled an intracavity MEMS mirror was reported in Chapter 3, where the mirror was scanning at its mechanical resonance to control the resonator losses. The pulse duration of the laser output was tunable by controlling the scan angle of the MEMS mirror, and inherently its rotational speed. Wavelength tuning of a continuous wave Yb: KGW laser was reported in Chapter 4, enabled the intracavity combination of a MEMS mirror and a dispersing prism in the Littman configuration. In this chapter, the same Yb: KGW laser platform is used to investigate simultaneous laser wavelength tuning and Q-switching enabled by a single intracavity MEMS mirror combined with a dispersing prism in the Littman configuration.

Wavelength tunable, Q-switched solid-state lasers have been previously reported in literature using bulk optical components. For example, a Q-switched Nd: YAG laser was reported with six different output wavelengths between 1318.8 nm and 1356 nm [101]. Q-switching was done using an acousto-optic modulator and the laser wavelength was tuned using a blazed diffraction grating in the Littrow configuration. A Ti: Sapphire laser was also reported with a wavelength tuning range of 150 nm between 720 nm and 870 nm [102]. The laser was end-pumped by a Q-switched, frequency-doubled Nd: YAG laser and wavelength tuning was enabled by a prism and a rotatable output coupler. Both techniques required separate mechanisms for Q-switching and wavelength tuning. For the work in this chapter, both Q-switching and wavelength tuning are enabled by one mechanism: the actuation of a MEMS mirror.

The MEMS mirror used for this work was the mirror with four electrothermal (ET) actuators that was reported in Chapter 2. The tilt angle of the ET mirror was controllable on two axes due to the radial positioning of the actuators around the circular mirror. In this work, one of the tilt axes was used for laser Q-switching while the other tilt axis was used for laser wavelength tuning. The laser setup is described in Section 5.1, including the measurement setup and a brief characterization of the ET mirror with respect to its use in this laser. The experimental characterization of the laser is described in Section 5.2 and the results are discussed further in Section 5.3.

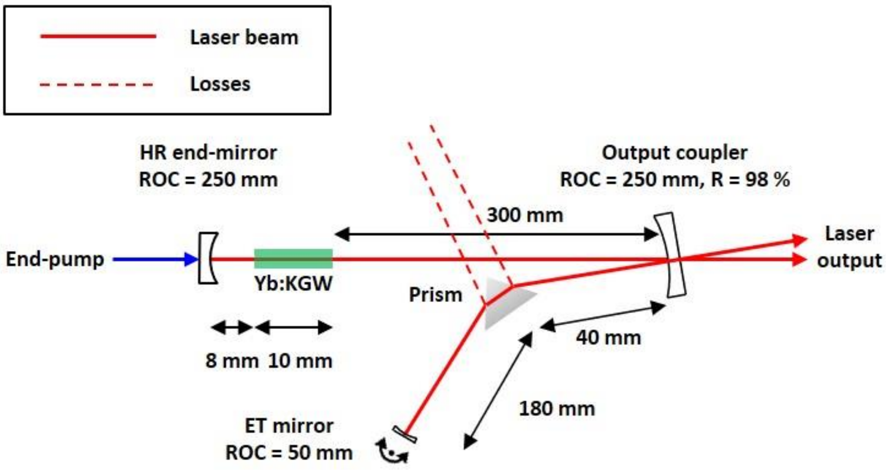

Figure 5-1: Schematic of the intracavity Yb: KGW laser with an equilateral dispersing prism and an ET mirror to enable laser wavelength tuning and Q-switching.

5.1. Laser setup

This work involved the same Yb: KGW laser platform that was reported in Chapter 4, where the Yb: KGW crystal was end-pumped at λ = 980 nm using a diode laser. The optimized resonator design was used to ensure the best laser performance with respect to wavelength tuning. The resonator consisted of a HR end mirror on the pump-side, a folding mirror, a SF11 prism and the ET mirror characterized in Chapter 2. A schematic of the laser is shown in Figure 5-1. The HR end mirror had a ROC of 250 mm and was positioned 8 mm from the pump-side facet of the Yb: KGW crystal. The folding mirror had a ROC of 250 mm, a reflectance of 98 % at the laser wavelength and was positioned 300 mm from the opposite facet of the Yb: KGW crystal. The folding mirror was also the output coupler of the laser. The SF11 prism was positioned 40 mm from the folding mirror and orientated with an angle of incidence that resulted in the transmitted beam propagating with the minimum angle of deviation through the prism. The ET mirror had a ROC of 50 mm and was positioned 180 mm from the prism. As discussed in Chapter 4, two laser output beams occurred due to a double pass of the output coupler during a roundtrip of the resonator. Both beams had similar output characteristics. Two beams were also emitted from the reflections at the prism surfaces. These were considered losses.

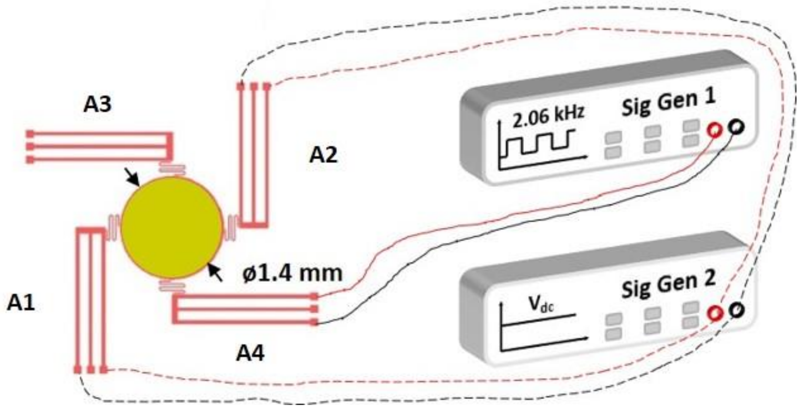

Figure 5-2: Schematic of the ET mirror design with labelled actuators A1 to A4. Actuator A3 was connected to Sig Gen 1 and driven at its mechanical resonance using a square-wave voltage signal. Actuators A1 and A2 were connected in turn to Sig Gen 2 and were tilted to a fixed angle using a DC voltage signal.

5.1.1. ET mirror

The mechanisms behind laser Q-switching and laser wavelength tuning using a MEMS mirror are different. As reported in Chapter 3, Q-switching requires the mirror to scan at its mechanical resonance to rapidly tune the resonator losses. Wavelength tuning on the other hand requires the mirror to be tilted at a fixed angle to select the laser wavelength that is optimally fed back through the resonator, as reported in Chapter 4. To prevent crosstalk between the two tuning mechanisms, the mirror movement for each mechanism had to occur on different tilt axes. The ET mirror was shown in Chapter 2 to have 2D movement capability. This was enabled by four ET actuators positioned radially around the circular mirror, as shown in Figure 5-2.

Laser wavelength tuning was possible when the ET mirror tilt occurred on the dispersive axis of the prism. This coincided with the mirror tilt induced by actuators A1 and A2. Actuators A3 and A4 induced mirror tilt on the orthogonal axis and could therefore be used for laser Q-switching. Only one actuator was required to activate the mechanical resonance of the mirror. Actuator A4 was therefore used since this was the actuator used in the Q-switched Nd: YAG laser in Chapter 3. A diagram of the resulting ET mirror setup is shown in Figure 5-2. Actuator A4 was connected to a signal generator configured to output a square-wave voltage signal with a frequency of 2.06 kHz, a duty cycle of 50% and an offset equal to half the signal amplitude. Actuators A1 and A2 were connected interchangeably to

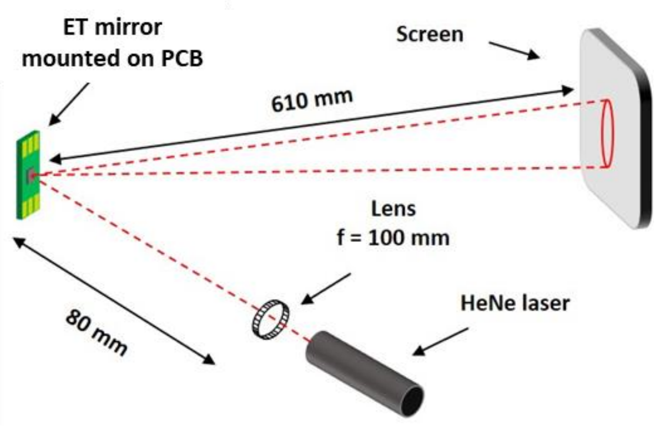

Figure 5-3: Diagram of the measurement setup used to analyse the ET mirror movement.

a second signal generator configured to output a DC voltage signal. Actuator A3 was unused in this work.

Recall from Chapter 2 that the resonant tilt movement of the ET mirror had an elliptical profile caused by coupling between the resonant axes of the device. This occurred because the actuators on orthogonal axes were identical, resulting in the same mechanical resonance on two axes. The peak mechanical resonance, resulting in the largest TOSA on the major axis of the ellipse, was achieved at a frequency of 2.05 kHz. The elliptical scanning movement meant that the mirror did not cross its resting position while resonantly scanning. This was anticipated to complicate the alignment of the Q-switched laser. As discussed in Chapter 3, this was avoided by driving the mirror slightly off-resonance at a frequency of 2.06 kHz, where the ellipticity of the scanning movement was increased towards a 1D line. A diagram of the elliptical scanning movement when driven at 2.05 kHz and 2.06 kHz was shown in Figure 3-12 for a signal amplitude of 10 V.

The characterization of the ET mirror in Chapter 2 included independent investigations of static mirror tilt and resonant scanning. This section describes the investigation of both movement mechanisms activated simultaneously with respect to the setup used for the Yb: KGW laser. The mirror movement was analysed by directing the beam from a HeNe laser towards the ET mirror and reflecting it onto a screen 610 mm from the ET mirror, as shown in Figure 5-3. A lens with a focal length of 100 mm was placed 80 mm from the ET mirror between it and the HeNe laser source. This was done to reduce the spot size on the screen, allowing a more accurate measurement of the mirror tilt angle.

The mirror rest position was marked on the screen as a reference. A square-wave voltage signal with an amplitude of 10 V and a frequency of 2.06 kHz was then supplied to actuator

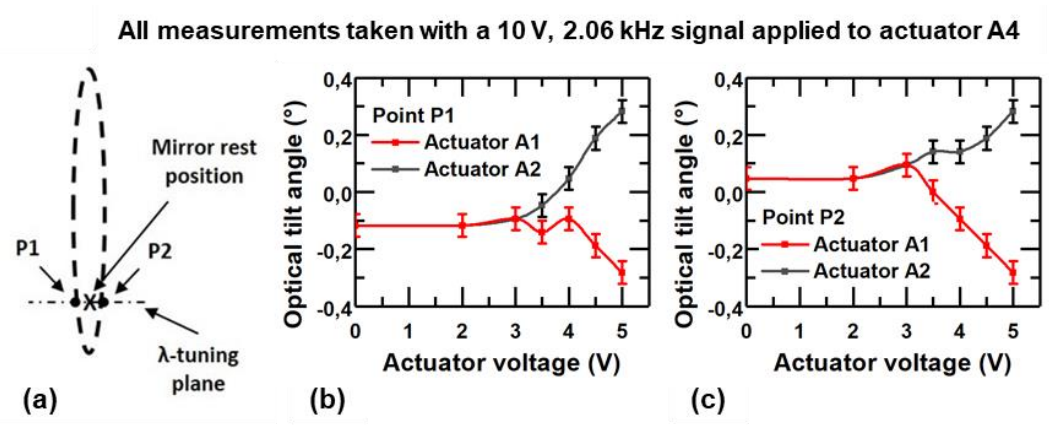

Figure 5-4: (a) Diagram showing the measurement points for the optical tilt angle of the ET mirror while a constant signal amplitude of 10 V at a frequency of 2.06 kHz was applied to actuator A4. (b) Plot showing the optical tilt angle of point P1 with respect to the mirror rest position as a voltage was applied to actuators A1 and A2. (c) Plot showing the optical tilt angle of point P2 with respect to the mirror rest position as a voltage was applied to actuators A1 and A2.

A4, causing it to scan resonantly on the y-axis with an elliptical movement profile and a total TOSA of 6.3° on the major axis of the ellipse. This signal was maintained throughout the following investigation. A DC voltage signal was then applied to either actuator A1 or A2, causing the mirror to tilt on the x-axis in addition to scanning resonantly on the y-axis. The optical tilt angle of the mirror on the x-axis was measured with respect to the mirror rest position at points P1 and P2 of the elliptical scan profile, shown in Figure 5-4a. These points were chosen because they coincided with the wavelength tuning axis of the Yb: KGW laser. Plots of the optical tilt angle of the mirror on the x-axis at points P1 and P2 are given in Figure 5-4b and Figure 5-4c respectively for different DC voltages applied to actuators A1 and A2. Positive values of tilt represent clockwise rotation of the mirror and negative values represent anticlockwise rotation. A measurement accuracy of ± 0.04° was yielded.

With no voltage applied to actuators A1 or A2, the optical tilt angle of points P1 and P2 were measured to be -0.07° and 0.12° respectively, giving an angular separation of 0.19°. A DC voltage was then applied to actuator A1. No measurable change in tilt angle on the x-axis was observed until a voltage of 2 V. The optical tilt angle of point P1 was then measured to change nonlinearly from -0.07° to -0.28° as the voltage across actuator A1 was increased from 2 V to 5 V. The corresponding optical tilt angle of point P2 was measured to change

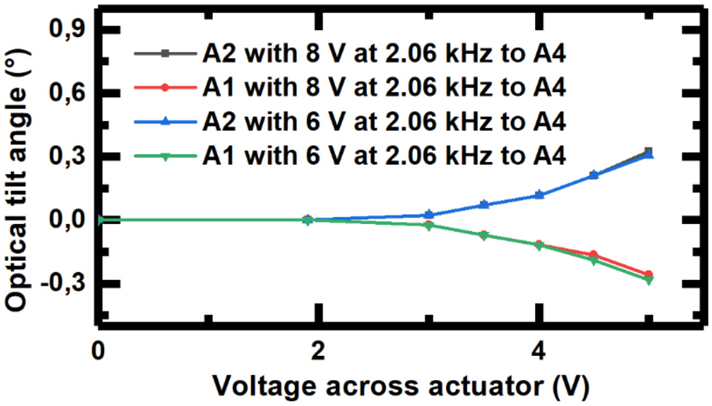

Figure 5-5: Plot showing the optical tilt angle of the ET mirror on the x-axis against the voltage across actuators A1 and A2 while the mirror was resonantly scanning on the y-axis at a rate of 2.06 kHz.

from 0.12° to -0.27° for the same conditions. The angular separation of points P1 and P2 therefore decreased from 0.19° to less than 0.04°.

The voltage across actuator A1 was then decreased to 0 V and the same measurement scheme was applied to actuator A2. No measurable tilt angle on the x-axis was observed until a voltage of 2 V. The optical tilt angle of point P1 was then measured to change nonlinearly from -0.07° to 0.28° as the voltage across actuator A2 was increased from 2 V to 5 V. The optical tilt angle of point P2 was measured to change from 0.12° to 0.31° for the same conditions. The angular separation of points P1 and P2 therefore decreased from 0.19° to less than 0.04°.

The characterization of the ET mirror until this point was done while the mirror was scanning resonantly at a frequency of 2.06 kHz and a TOSA of 6.3° on the y-axis. The same measurement process was applied when the amplitude of the square-wave voltage signal applied to actuator A4 was changed to 8 V and to 6 V, resulting in a reduction of the mirror TOSA to 1.2° and 0.6° respectively. The signal frequency of 2.06 kHz was maintained. For both cases (8 V and 6 V), the angular separation of points P1 and P2 was measured to be less than 0.04 ° throughout. The optical tilt angle of points P1 and P2 individually could therefore not be measured because they were overlapping on the screen. The midpoint of P1 and P2 was therefore measured and the resulting plot is shown in Figure 5-5. With a signal amplitude of 8 V applied to actuator A4, the optical tilt angle of the scanning ET mirror on the x-axis was measured to change from 0° to 0.32° as the voltage applied to actuator A2

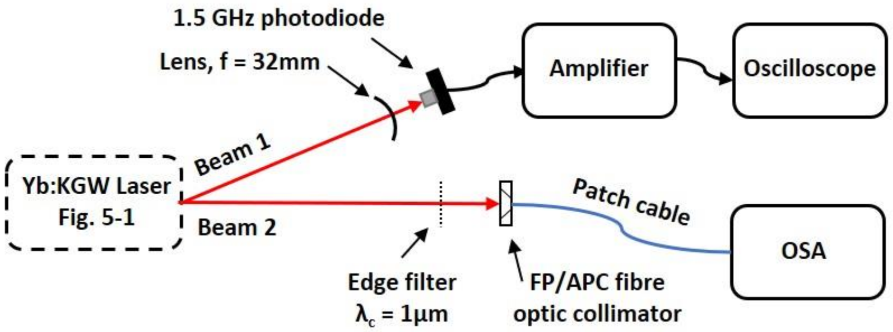

Figure 5-6: Diagram of the experimental setup to measure the spectral and temporal output characteristics of the Yb: KGW laser.

was increased from 2 V to 5 V. For 5 V applied to actuator A1, the optical tilt angle was measured to be -0.26°. With a signal amplitude of 6 V applied to actuator A4, the optical tilt angle of the ET mirror on the x-axis was measured to change from 0° to 0.31° as the voltage applied to actuator A2 was increased from 2 V to 5 V. For 5 V applied to actuator A1, the optical tilt angle was measured to be -0.28°.

5.1.2. Measurement setup

The Yb: KGW laser shown previously in Figure 5-1 was constructed and aligned while the ET mirror was at its resting position to achieve the lowest laser threshold in CW mode. This was done using a short two-mirror laser as a reference as described previously in Section 4.3.2. The CW laser threshold was achieved at an absorbed pump power of 7.8 W. A square-wave voltage signal with an amplitude of 10 V and a frequency of 2.06 kHz was then supplied to actuator A4, causing it to scan resonantly on the y-axis with an elliptical movement profile and a TOSA of 6.3° on the major axis of the ellipse. At this point, lasing was lost because of two reasons: the higher laser threshold required for Q-switched lasers, and the fact that the elliptical movement profile of the mirror did not cross the mirror rest position. The pump power was increased iteratively while adjusting the angle of the ET mirror until lasing re-occurred. The minimum laser threshold occurred at an absorbed pump power of 8.7 W, at which point P1 in Figure 5-4a overlapped the original mirror rest position.

The resulting Q-switched laser yielded two output beams because of a double pass of the output coupler during a roundtrip of the resonator. The characteristics of these beams were measured to be similar. One of the beams was used to measure the spectral characteristics of the laser output, while the other was used to simultaneously measure the temporal characteristics. A diagram of the measurement setup is shown in Figure 5-6. The spectral laser characteristics were measured by fibre-coupling the beam emitted from the direction of the Yb: KGW crystal (beam 2) into an HP86142A optical spectrum analyser (OSA). An edge filter with a sharp cut-off at $\lambda = 1$ µm was used to filter out residual pump light. The OSA was configured with a resolution bandwidth of 0.1 nm and a video bandwidth of 2 kHz. The temporal laser characteristics were measured by focusing the beam emitted from the direction of the prism (beam 1) onto a 1.5 GHz photodiode using a lens with a focal length of 32 mm. The output of the photodiode was then fed through a Femto DHCPA-100 amplifier and into an Agilent DS06034A oscilloscope.

The transverse mode profile and the M^2 divergence rate of the laser output were intermittently measured for beam 2 after insertion of the edge filter. The transverse mode profile was measured using a WinCamD UCD12 CCD camera inserted into the beam path. The M^2 was evaluated by focusing the beam using a lens with a focal length of 100 mm and measuring the $1/e^2$ beam radius at several positions around the beam waist. Distance intervals of 10 mm up to a maximum of 60 mm from the beam waist were used. The resulting distribution was then fitted to a simulated Gaussian beam distribution defined by Equation 3-1.

5.2. Experimental results

The following subsections describe the experimental characterization of the wavelength tunable, Q-switched laser. As described in the previous section, the laser was initially set up with the ET mirror scanning at a TOSA of 6.3° on the y-axis. The laser output beam was firstly characterized in this initial condition. Laser wavelength tuning was then investigated by tilting the scanning ET mirror to a fixed angle on the x-axis. Control of the Q-switch pulse duration was then investigated by changing the TOSA of the mirror on the y-axis.

The average output power of the Q-switched laser was limited to 5 mW to prevent ablation of the ET mirror surface due to laser light absorbed within the gold layer. The average laser output power was monitored by inserting an optical power meter (Gentec XLP12) into the path of beam 1 in Figure 5-6.

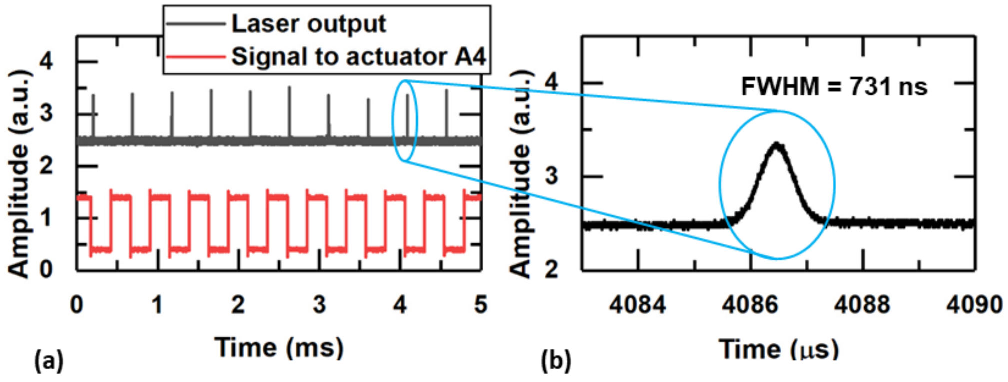

Figure 5-7: Temporal plots of the Q-switched laser output: (a) temporal comparison of the laser output with the 10 V, 2.06 kHz square-wave voltage signal applied to actuator A4, (b) zoomed plot showing a single pulse.

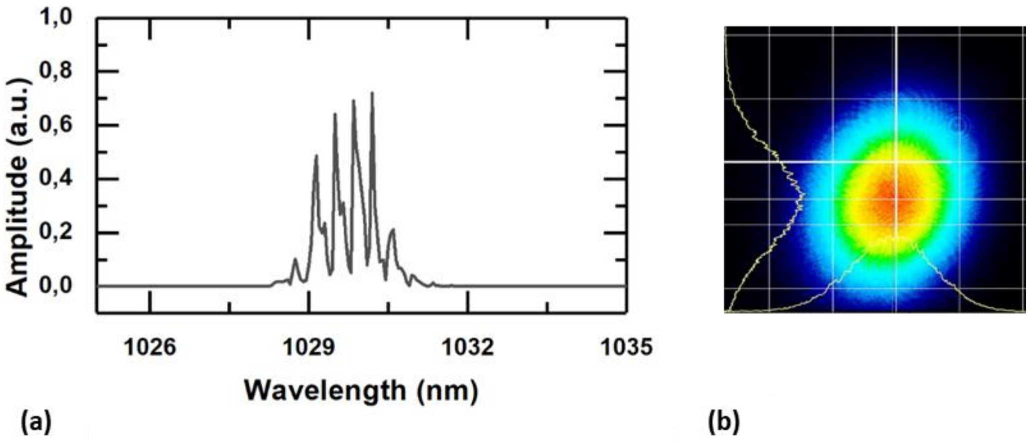

Figure 5-8: (a) Spectrum of the pulsed laser output measured using an OSA. (b) Transverse mode profile of the pulsed laser output measured using a CCD camera.

5.2.1. Initial laser output

The laser was first characterized in its initial condition with a signal amplitude of 10 V at a frequency of 2.06 kHz applied to actuator A4 of the ET mirror. The mirror was therefore scanning resonantly with a TOSA of 6.3° on the y-axis. The laser threshold was reached at an absorbed pump power of 8.7 W and an average laser output power of 5 mW was measured at an absorbed pump power of 9.0 W. A sample of the laser output (pulse train) measured using the oscilloscope had a pulse repetition rate of 2.06 kHz and is shown in Figure 5-7a. This corresponded to one pulse per movement cycle of the ET mirror, indicating that only one side of the elliptical scan profile resulted in laser alignment and pulse emission.

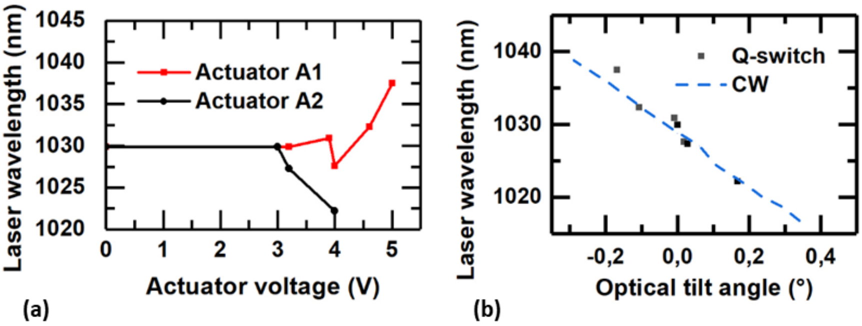

Figure 5-9: (a) Plot of the pulsed laser output wavelength against voltage applied to actuators A1 and A2. (b) Plot of the laser output wavelength against the optical tilt angle of the ET mirror on the x-axis.

The measured pulses yielded a Gaussian profile and had a FWHM pulse duration of 731 ± 6 ns. A zoomed plot of a sample pulse is shown in Figure 5-7b. The average amplitude jitter was measured to be 6.6% and the average timing jitter was measured to be 4 ns.

The spectral properties of the pulsed laser output beam were measured using the OSA and are shown in Figure 5-8a. The peak laser wavelength was measured to be $\lambda_0 = 1029.9$ nm and the FWHM linewidth was measured to be 1.4 nm. Several peaks were observed in the laser output spectrum. The root cause for this phenomenon is unknown, but a potential cause is convolution between the laser pulses and the sampling rate of the OSA. The transverse mode profile of the pulsed laser output was measured using the CCD camera and is shown in Figure 5-8b to resemble a TEM_{00} beam. The M^2 was measured to be 1.1 on the x-axis and 1.0 on the y-axis.

5.2.2. Tunable laser wavelength

While investigating tunable laser wavelength, the 10 V, 2.06 kHz square-wave voltage signal to actuator A4 was maintained. The ET mirror was therefore scanning resonantly at a TOSA of 6.3° throughout. To tune the wavelength of the pulsed laser output, the ET mirror was tilted to a fixed angle on the dispersive axis of the prism using actuators A1 and A2. The pump power was adjusted for each measurement to maintain an average laser output power of 5 mW and protect the ET mirror surface from being damaged.

A plot of the peak laser wavelength against the voltage applied to actuators A1 and A2 is shown in Figure 5-9a. When actuating A1, no measurable change in laser wavelength was

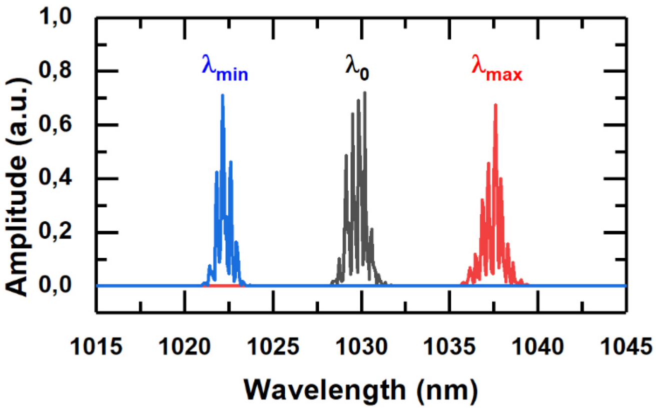

Figure 5-10: Plot showing the output spectrum of the Q-switched laser at λ_0 = 1029.9 nm, λ_{min} = 1022.2 nm and λ_{max} = 1037.5 nm.

observed until an actuator voltage of 3.2 V. The laser wavelength was then tunable from λ_0 = 1029.9 nm at 3.2 V to λ_{min} = 1022.2 nm at 4.0 V. When actuating A2, no measurable change in laser wavelength was observed until an actuator voltage of 3.0 V. For an increase in actuator voltage from 3.0 V to 3.9 V, the laser wavelength was tuned from 1029.9 nm to 1030.9 nm. For a further increase in actuator voltage to 4.0 V, the laser wavelength jumped abruptly from 1030.9 nm to 1027.6 nm. The laser wavelength then increased towards λ_{max} = 1037.5 nm as the voltage was increased from 4.0 V to 5.0 V.

The before-mentioned jump in laser wavelength when using actuator A2 was a result of the elliptical scanning movement of the ET mirror. The laser was initially aligned for point P1 on the left side of the ellipse in Figure 5-4a. Tilting the mirror using actuator A2 then resulted in point P2 on the right side of the ellipse moving towards laser alignment. At an actuator voltage of 4.0 V, it is assumed that point P2 resulted in less resonator losses than point P1. This nonlinearity and methods to eliminate it are further discussed in Section 5.3.

From the above-described results, the peak laser wavelength was tunable between λ_{min} = 1022.2 nm and λ_{max} = 1037.5 nm, giving a total range of 15.3 nm. A comparative plot of the measured laser output spectrum is shown in Figure 5-10 for λ_0, λ_{min} and λ_{max}. The power (amplitude) in this comparative plot is relative to the coupling efficiency, which may have changed between measurements. The FWHM linewidth was measured to be 0.9 nm at λ_{min} and 1.2 nm at λ_{max}. The optical tilt angle of the ET mirror at λ_{min} and λ_{max} was calculated to be -0.168° and 0.168° respectively. A plot of the peak laser wavelength against the optical tilt angle of the ET mirror is shown in Figure 5-9b, where the results of the Q-switched laser are compared to the CW laser reported in Chapter 4. For a similar shift in the CW laser wavelength, the required mirror tilt angles were -0.185° and 0.185° respectively. This

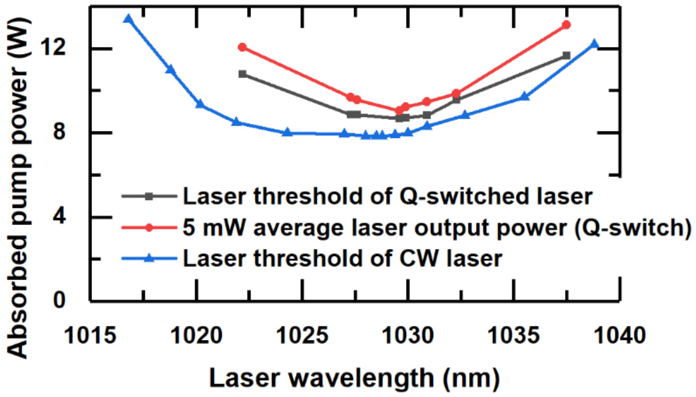

Figure 5-11: Plot showing the absorbed pump power required to reach laser threshold and 5 mW of average laser output power for the Q-switched laser and the absorbed pump power required to reach laser threshold for the CW laser in Chapter 4.

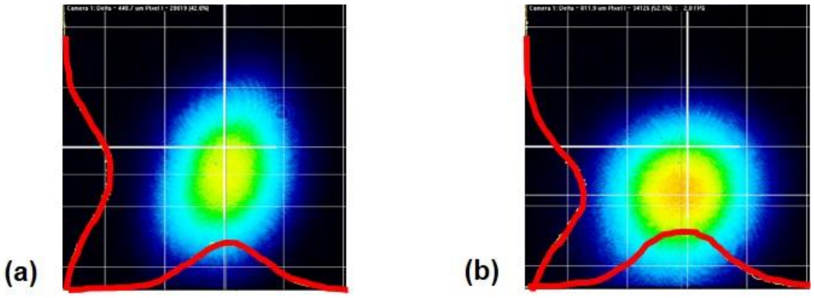

Figure 5-12: Transverse mode profiles of the pulsed laser output at wavelengths (a) 1022.2 nm and (b) 1037.5 nm.

showed that the Q-switched laser wavelength followed a similar trend to that of the same laser in CW mode.

As the laser wavelength was tuned, the absorbed pump power required to reach laser threshold and an average laser output power of 5 mW changed. Alike the work in Chapter 4, this was caused by the non-uniform gain cross-section of Yb: KGW. A plot showing the absorbed pump power against laser wavelength is shown in Figure 5-11. The absorbed pump power required to reach laser threshold for the Q-switched laser was 10.8 W at λ_{min} = 1022.2 nm and 11.6 W at λ_{max} = 1037.5 nm. An absorbed pump power of 12.1 W at λ_{min} = 1022.2 nm and 13.1 W at λ_{max} = 1037.5 nm was then required to reach an average laser output power of 5 mW. Beyond these laser wavelengths, an output power of 5 mW could not be achieved with a pump power of less than 13.2 W.

The transverse mode profile of the pulsed laser output at λ_{min} and λ_{max} was measured using the CCD camera. The resulting images are shown in Figure 5-12a and Figure 5-12b

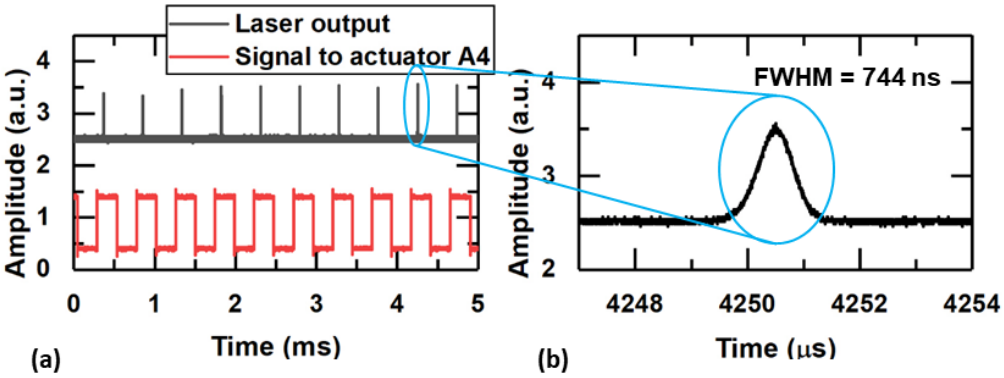

Figure 5-13: Temporal plots of the Q-switched laser output at λ_{max}: (a) temporal comparison of the laser output with the 10 V, 2.06 kHz square-wave voltage signal applied to actuator A4, (b) zoomed plot showing a single pulse.

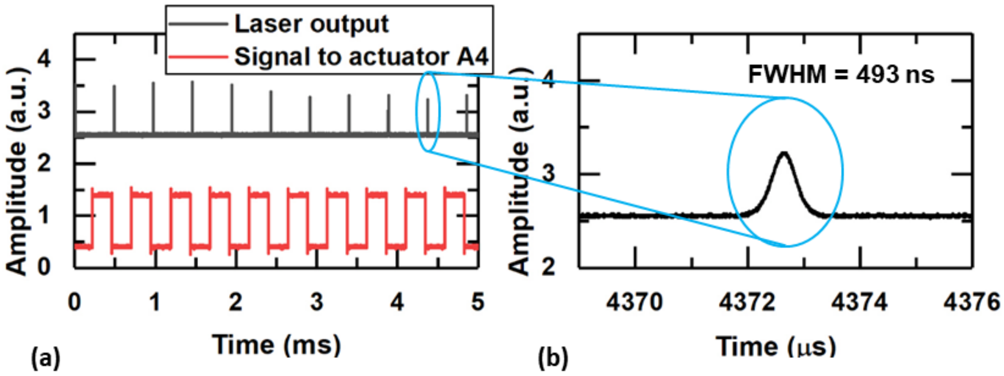

Figure 5-14: Temporal plots of the Q-switched laser output at λ_{min}: (a) temporal comparison of the laser output with the 10 V, 2.06 kHz square-wave voltage signal applied to actuator A4, (b) zoomed plot showing a single pulse.

respectively. A TEM_{00} mode profile was measured and the M^2 beam divergence rate was measured to be less than 1.1 on x-axis and the y-axis in both cases.

The temporal characteristics of the pulsed laser output beam were monitored using the oscilloscope as the laser wavelength was tuned. Plots of the pulse trains and zoomed pulses at λ_{max} and λ_{min} are shown in Figure 5-13 and Figure 5-14 respectively. In the case of λ_{max}, the FWHM pulse duration was measured to be 744 ± 5 ns with an average amplitude jitter of 5% and an average timing jitter of 7 ns. In the case of λ_{min}, the FWHM pulse duration was measured to be 493 ± 19 ns, with an average amplitude jitter of 13% and an average timing jitter of 15 ns. The pulse duration therefore varied as the laser wavelength was tuned, despite the TOSA of the ET mirror being maintained at 6.3°. This was assumed to be caused by multiple changes to the laser dynamics as the wavelength was tuned, including (but not

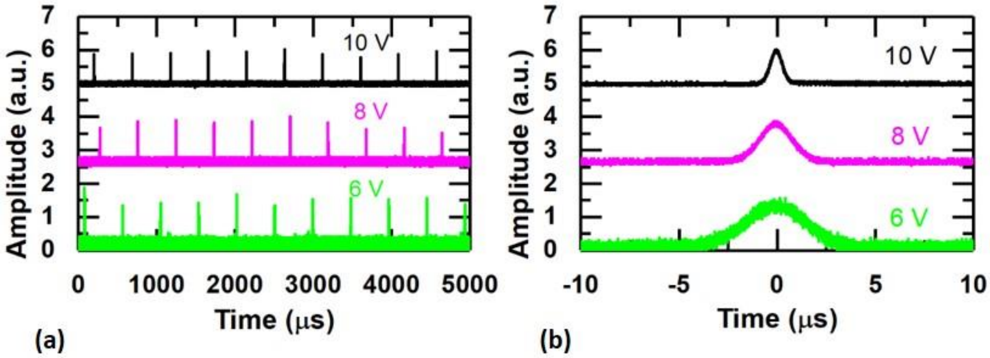

Figure 5-15: Temporal plots of the Q-switched laser output for signal amplitudes of 10 V, 8 V and 6 V applied to actuator A4 at a frequency of 2.06 kHz: (a) sample pulse train of the laser output, (b) zoomed plot of individual normalized pulses.

limited to) wavelength dependent gain, pump intensity and the speed of the Q-switch. This is discussed further in Section 5.3.

5.2.3. Tunable pulse duration

The FWHM pulse duration of the laser output at each laser wavelength was tuned by changing the amplitude of the square-wave voltage signal applied to actuator A4, causing the TOSA of the ET mirror on the y-axis to change. As the signal amplitude was decreased from 10 V to 6 V, the mirror TOSA decreased from 6.3° to 0.6°. This change therefore resulted in a reduced rotational speed of the mirror and a longer pulse emission gate. The signal frequency was maintained at 2.06 kHz throughout this investigation to maintain a constant Q-switch rate.

The tunable pulse duration was first investigated at the centre wavelength of the laser (λ_0), i.e. no voltage applied to actuators A1 or A2. The signal amplitude to actuator A4 was reduced from 10 V to 6 V in steps of 1 V and the temporal characteristics of the pulsed laser output were measured using the oscilloscope. A plot of the resulting pulse trains at 10 V, 8 V and 6 V are shown in Figure 5-15a and a comparative plot of individual pulses are shown in Figure 5-15b. The pulse profiles were observed to be Gaussian for all measurements. At 10 V, the measured pulses had a FWHM duration of 731 ± 6 ns, an average amplitude jitter of 6.6% and an average timing jitter of 4 ns. At 8 V, the measured pulses had a FWHM duration of 1972 ± 41 ns, an average amplitude jitter of 12.1% and an average timing jitter of 96 ns. At 6 V, the measured pulses had a FWHM duration of 3742 ± 142 ns, an average

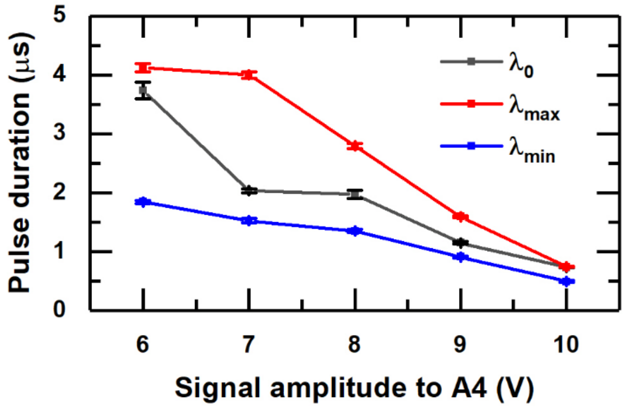

Figure 5-16: Plot showing the FWHM pulse duration of the Q-switched laser output against the signal amplitude applied to actuator A4 for centre, maximum and minimum laser wavelengths (see Figure 5-17).

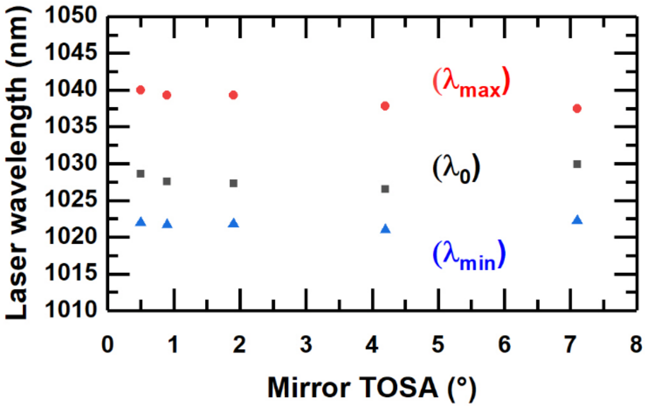

Figure 5-17: Plot showing the centre, maximum and minimum laser wavelengths against the TOSA of the ET mirror.

amplitude jitter of 11.1% and an average timing jitter of 268 ns. A total tuning range of 3011 ns was therefore achieved. At signal amplitudes of less than 6 V applied to actuator A4, the rotational speed of the ET mirror became too slow and resulted in multiple pulse emission.

The FWHM pulse duration at each signal amplitude to A4 was also measured as the laser wavelength was tuned. As described in Section 5.2.2, wavelength tuning was enabled by actuators A1 and A2, which tilted the ET mirror on the x-axis while it was scanning resonantly on the y-axis. The centre wavelength (λ_0), the maximum wavelength (λ_{max}) and the minimum wavelength (λ_{min}) of the pulsed laser output were measured using the OSA. A plot of the FWHM pulse duration against the signal amplitude to A4 is shown in Figure 5-16 for λ_0, λ_{max} and λ_{min}. A corresponding plot showing the values of λ_0, λ_{max} and λ_{min} against the TOSA of the ET mirror is shown in Figure 5-17.

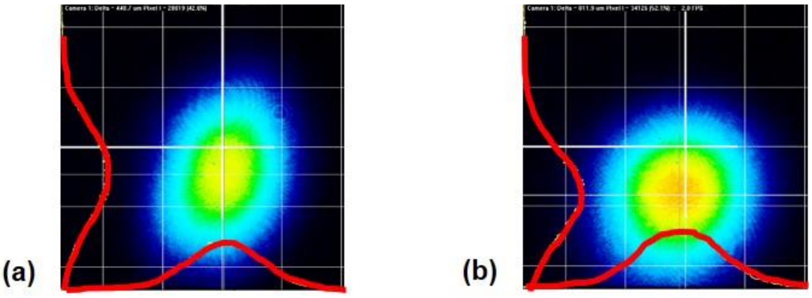

Figure 5-18: Transverse mode profiles of the pulsed laser output at λ_0 for a signal amplitude of (a) 8 V to A4 and (b) 6 V to A4.

At λ_{max}, the pulse duration was tunable from 744 ± 7 ns to 4123 ± 67 ns for a respective change in signal amplitude to A4 from 10 V to 6 V, giving a range of 3379 ns. Respectively at λ_{min}, the pulse duration was tunable from 493 ± 17 ns to 1845 ± 29 ns, giving a range of 1352 ns. The value of λ_{max} was measured to be 1037.5 nm at a signal amplitude of 10 V, 1039.5 nm at 8 V and 1040.4 nm at 6 V, with respective FWHM linewidths of 1.2 nm, 0.2 nm and 0.8 nm. The value of λ_{min} was measured to be 1022.2 nm at 10 V, 1021.7 nm at 8 V and 1022.2 nm at 6 V, with respective FWHM linewidths of 0.9 nm, 0.2 nm and 0.4 nm. The tunable wavelength range was therefore 15.3 nm at a signal amplitude of 10 V to A4, 17.8 nm at 8 V and 18.2 nm at 6 V.

In all cases, the pulse duration was observed to increase as the scan angle of the ET mirror was decreased. This was consistent with a longer pulse emission gate. Alongside the tunable pulse duration, the values of λ_0, λ_{max} and λ_{min} also varied by ± 1.5 nm as the scan angle of the ET mirror was changed. This was caused by the nonlinear response of the ET mirror. FWHM linewidths varying from 0.2 nm up to 1.4 nm were measured with no clear correlation. It is expected that operating the laser so close to the laser threshold and convolution between the laser pulses and the sampling rate of the OSA had an impact on these measurements.

The transverse mode profile and the M^2 beam divergence rate of the pulsed laser output beam were measured at λ_0 for signal amplitudes of 8 V and 6 V using the CCD camera. Images of the measured mode profiles are shown in Figure 5-18 to have a TEM_{00} profile. The M^2 was measured to be less than 1.1 for all measurements on the x-axis and the y-axis.

5.3. Discussion

A Q-switched solid-state laser with simultaneously tunable output wavelength and pulse duration has been reported with a limited average output power of 5 mW. The tunable properties were enabled by dual-axis actuation of a single electrothermally actuated MEMS mirror. The laser wavelength was tunable between ~ 1022 nm and ~ 1040 nm, limited by the gain bandwidth of the Yb: KGW crystal and the pump intensity. FWHM pulse durations between 493 ns and 4123 ns were achieved, with longer pulses hindered by the emission of multiple pulses.

As was the case with the lasers described previously in Chapters 3 and 4, the laser output power was limited to avoid damaging the surface of the MEMS mirror. To power scale the laser output, a method for depositing a high-reflectance coating must be developed, with the ideal result being a reflectance of more than 99 % and a flat mirror surface. This would then enable power scaling of the laser output and a lower laser threshold which would enable a larger wavelength tuning range. It would also enable a simpler resonator design and a simpler theoretical model of the laser, since a flat mirror can be placed at any distance from the prism without affecting the wavelength tuning performance.

The results reported in this chapter were significantly affected by the nonlinear response of the ET mirror. Firstly, the laser alignment was complicated because the elliptical scan movement did not coincide with the mirror resting position. Secondly, the elliptical movement profile when scanning at its mechanical resonance resulted in a jump in the laser wavelength as the laser wavelength transferred from one side of the ellipse to the other while the mirror was tilted. Thirdly, the laser wavelength varied as the pulse duration was tuned. These effects can be eliminated by the design of a MEMS mirror with a scanning movement that does not yield significant coupling between the resonant axes.

6. Conclusions

The work presented in this thesis investigated the use of MEMS mirrors as intracavity tuning elements in solid-state lasers. Two types of MEMS mirror were introduced and characterized: a mirror with four radially positioned electrothermal (ET) actuators and an array of mirrors each with a single-sided electrostatic (ES) comb-drive actuator. Both mirrors could be driven at their respective mechanical resonance, resulting in resonant scanning. The ET mirror could also be tilted to a fixed angle by applying a DC signal to an actuator. Three novel laser concepts were investigated with the MEMS mirrors used as intracavity tuning devices. The first concept was a Q-switched Nd: YAG laser with tunable temporal characteristics enabled by two intracavity MEMS mirrors (one ET mirror and one ES mirror). The second concept was an Yb: KGW laser with continuously tunable output wavelength enabled by the combination of a prism and an ET mirror in the Littman configuration. The third concept was a Q-switched Yb: KGW laser with tunable output wavelength and pulse duration enabled by the combination of a prism and an ET mirror in the Littman configuration.

The Nd: YAG laser could be Q-switched at a rate of 2.06 kHz or 20.09 kHz, enabled by the mechanical resonances of the MEMS mirrors. At 20.09 kHz, the Q-switch pulse duration was tunable between 477 ns and 3100 ns by controlling the scan angle of the scanning MEMS mirror. Short bursts of pulses were also enabled by simultaneous actuation of both MEMS mirrors. A wavelength tunable Yb: KGW laser was reported where the tuning mechanism was a MEMS mirror combined with a prism in the Littman configuration. A variety of laser configurations were investigated, with continuous tuning from 1016.8 nm to 1038.8 nm achieved for the optimized design. The theoretical analysis of the laser was found to match the experimental results. The wavelength range was limited by the gain bandwidth of the Yb: KGW crystal and the intensity of optical pumping. The same Yb: KGW laser platform was also reported to be Q-switched by activating the second axis of the MEMS mirror. The output wavelength of the Q-switched laser was tunable between 1022 nm and 1040 nm, with independently tunable Q-switch pulse duration between 500 ns and 4100 ns.

All the above-described lasers yielded excellent beam quality but were limited by the damage threshold of the MEMS mirror surfaces. Laser output powers of less than 50 mW may be suitable in some biomedical applications, but power-scaling is required to be compatible with other applications such as defence, industrial, gas sensing and automotive.

The development of a reliable process to deposit an HR optical coating on the surface of the MEMS mirrors would enable power-scaling of the laser output to be realized. The demonstrated techniques are applicable to any region of the optical spectrum, meaning many applications could potentially benefit from adopting them. The laser concepts were the first of their kind to be reported and demonstrated the synergy between MEMS and solid-state laser technologies. The use of MEMS to replace multiple bulk optical components paves the way towards a miniaturised solid-state laser with digitally tunable output properties.

Table 6-1: Summary of the MEMS lasers investigated in this thesis and their tunable characteristics.

Laser type	Capability	Results
Q-switched Nd: YAG laser	Tunable pulse duration	ES mirror: 477 ns to 3100 ns at 20 kHz
	Different Q-switch rates	ES mirror: 20 kHz (Pulse duration 477 ns to 3100 ns)
		ET mirror: 2 kHz (Pulse duration 1450 ns)
	Pulse burst mode	ES mirror: Q-switch at 20 kHz ET mirror: on/off switch at 10 Hz
CW Yb: KGW laser	Tunable wavelength	ET mirror: - 1022.2 nm to 1038.8 nm - FWHM linewidth < 0.25 nm
Q-switched Yb: KGW laser	Tunable pulse duration	ET mirror: - Q-switch at 2 kHz - Pulse duration 493 ns to 4123 ns - Wavelength 1022 nm to 1040 nm
	Tunable wavelength	

7. Recommended future work

The next step for the research of MEMS mirrors as intracavity components in solid-state lasers is to demonstrate them in real-world applications. Q-switched lasers and wavelength tunable lasers are used in a myriad of diverse application areas, all of which may benefit from miniaturization, reduced power demand and enhanced tunability. The lasers reported in this thesis are by no means optimized but demonstrate clear potential for the synergy between solid-state lasers and MEMS.

Optimization of the lasers can be achieved by several means. The first and foremost is the development of a reliable method to deposit a HR coating on the surface of the MEMS mirrors. The HR coating would ideally have a reflectance of more than 99 % at the laser wavelength, a flat mirror surface and would not hinder the performance of the MEMS actuators. This would then enable the lasers to be power scaled to achieve the best overall performance for the specific application. It would also enable the resonator design to be simplified with a reduced spatial footprint, since the curvature of the MEMS mirror surface and its dependence on device temperature would not have such a strong impact on the laser dynamics.

With respect to the MEMS devices themselves, further optimization of the actuator design would result in more predictable laser performance. For example, the elliptical scanning movement of the ET mirror was caused by coupling between the resonant axes of the device. This nonlinearity had a significant impact on the tuning performance of the Q-switched lasers. Eliminating such nonlinearities would result in more predictable tuning of the laser properties and thus more reliable systems. Further work should be done to improve the performance characteristics of the MEMS mirrors and tailor them towards use in an application specific solid-state laser. The development of a hybrid MEMS mirror could also enable optimized tuning of multiple laser output characteristics by actuation of a single MEMS mirror.

References

[1] Yole development, "Status of the MEMS industry report," Online: http://www.yole.fr/PRESS.aspx, 2016.

[2] K. E. Petersen, "Silicon torsional scanning mirror," IBM Journal of Research and Development, vol. 24, no. 5, pp. 631-637, 1980.

[3] L. J. Hornbeck, "Deformable mirror spatial light modulators," Spatial Light Modulators and Applications III, Proceedings Paper vol. 1150, pp. 86-102, 1990.

[4] O. Solgaard, F. S. A. Sandejas, and D. M. Bloom, "Deformable grating optical modulator," Optics Letters, vol. 17, no. 9, pp. 688-690, May 1992.

[5] A. Werber and H. Zappe, "Tunable microfluidic microlenses," Applied Optics, vol. 44, no. 16, pp. 3238-3245, Jun 2005.

[6] D. L. Dickensheets and G. S. Kino, "Silicon-micromachined scanning confocal optical microscope," Journal of Microelectromechanical Systems, vol. 7, no. 1, pp. 38-47, Mar 1998.

[7] Innoluce, "Innovative MEMS mirror technology," Online: https://innoluce.com, 2010.

[8] S. Schilt et al., "Spectral and modulation properties of a largely tunable MEMS-VCSEL in view of gas phase spectroscopy applications," Applied Physics B-Lasers and Optics, Proceedings Paper vol. 100, no. 2, pp. 321-329, Aug 2010.

[9] Y. Watanabe et al., "Electromagnetically dual-axis driven MEMS grating and its application to 3D profiling with near-infrared low-coherence interferometry," Electronics and Communications in Japan, vol. 96, no. 2, pp. 9-15, Feb 2013.

[10] S. T. S. Holmstrom, U. Baran, and H. Urey, "MEMS Laser Scanners: A Review," Journal of Microelectromechanical Systems, vol. 23, no. 2, pp. 259-275, Apr 2014.

[11] Mirrorcle Technologies. "MEMS mirror modules - Applications." Online: http://mirrorcletech.com/applications.html.

[12] C. J. Chang-Hasnain, "Tunable VCSEL," IEEE Journal of Selected Topics in Quantum Electronics, vol. 6, no. 6, pp. 978-987, Nov-Dec 2000.

[13] A. Q. Liu and X. M. Zhang, "A review of MEMS external-cavity tunable lasers," Journal of Micromechanics and Microengineering, vol. 17, no. 1, pp. R1-R13, Jan 2007.

[14] Y. A. Peter et al., "Q-switched fiber laser using a torsional micro-mirror," IEEE/LEOS 1996 Summer Topical Meetings - Advanced Applications of Lasers in Materials and Processing, Digest, Keystone, USA, 1996, pp. C67-C68.

[15] M. Fabert, A. Desfarges-Berthelemot, V. Kermene, A. Crunteanu, D. Bouyge, and P. Blondy, "Ytterbium-doped fibre laser Q-switched by a cantilever-type micro-mirror," Optics Express, vol. 16, no. 26, pp. 22064-22071, Dec 2008.

[16] M. Fabert, V. Kermene, A. Desfarges-Berthelemot, P. Blondy, and A. Crunteanu, "Actively mode-locked fiber laser using a deformable micromirror," Optics Letters, vol. 36, no. 12, pp. 2191-2193, Jun 2011.

[17] W. Lubeigt et al., "Control of solid-state lasers using an intra-cavity MEMS micromirror," Optics Express, vol. 19, no. 3, pp. 2456-2465, Jan 2011.

[18] R. Bauer, A. Paterson, C. Clark, D. Uttamchandani, and W. Lubeigt, "Output Characteristics of Q-switched Solid-State Lasers Using Intracavity MEMS Micromirrors," IEEE Journal of Selected Topics in Quantum Electronics, vol. 21, no. 1, p. 356-363, Jan-Feb 2015.

[19] R. Li, M. Griffith, L. Laycock, and W. Lubeigt, "Controllable continuous-wave Nd:YVO4 self-Raman lasers using intracavity adaptive optics," Optics Letters, vol. 39, no. 16, pp. 4762-4765, Aug 2014.

[20] W. Koechner, "Solid-state laser engineering," 6th edition, Springer, 2006.

[21] O. Svelto, "Principles of Lasers," 5th edition, Springer, 2010.

[22] H. Kogelnik and T. Li, "Laser beams and resonators," Applied Optics, vol. 5, no. 10, pp. 1550-1567, 1966.

[23] M. G. Littman and H. J. Metcalf, "Spectrally narrow pulsed dye laser without beam expander," Applied Optics, vol. 17, no. 14, pp. 2224-2227, 1978.

[24] M. G. Littman, "Single-mode operation of grazing incidence pulsed dye laser," Optics Letters, vol. 3, no. 4, pp. 138-140, 1978.

[25] K. Liu and M. G. Littman, "Novel geometry for single-mode scanning of tunable lasers," Optics Letters, vol. 6, no. 3, pp. 117-118, 1981.

[26] B. Clesca, S. Gauchard, E. Lantoine, V. Rodrigues, F. Giraud, and D. Lesterlin, "3.2nm wavelength tuning via temperature control for integrated electroabsorption modulator DFB laser with high tolerance to chromatic dispersion," Electronics Letters, vol. 32, no. 10, pp. 927-929, May 1996.

[27] M. Lara-Castro et al., "Design and Modeling of Polysilicon Electrothermal Actuators for a MEMS Mirror with Low Power Consumption," Micromachines, vol. 8, no. 7, p. 19, Jul 2017.

[28] P. A. Himmer, D. L. Dickensheets, and R. A. Friholm, "Micromachined silicon nitride deformable mirrors for focus control," Optics Letters, vol. 26, no. 16, pp. 1280-1282, Aug 2001.

[29] Flexible Optical B.V., "Micromachined membrane deformable mirrors." Online: http://www.okotech.com/mmdm/.

[30] S. J. Lukes and D. L. Dickensheets, "SU-8 2002 Surface Micromachined Deformable Membrane Mirrors," Journal of Microelectromechanical Systems, vol. 22, no. 1, pp. 94-106, Feb 2013.

[31] S. Kim, C. Lee, J. Y. Kim, J. Kim, G. Lim, and C. Kim, "Two-axis polydimethylsiloxane-based electromagnetic microelectromechanical system

scanning mirror for optical coherence tomography," Journal of Biomedical Optics, vol. 21, no. 10, p. 6, Oct 2016.

[32] U. Baran et al., "Resonant PZT MEMS Scanner for High-Resolution Displays," Journal of Microelectromechanical Systems, vol. 21, no. 6, pp. 1303-1310, Dec 2012.

[33] T. B. Liu, D. L. Dickensheets, "MEMS deformable mirror with integrated black silicon aperture," IEEE International Conference on Optical MEMS and Nanophotonics (OMN), Glasgow, UK, Aug 17-21 2014, pp. 215-216.

[34] D. Torres et al., "VO2-Based MEMS Mirrors," Journal of Microelectromechanical Systems, vol. 25, no. 4, pp. 780-787, Aug 2016.

[35] M. A. Hopcroft, W. D. Nix, and T. W. Kenny, "What is the Young's Modulus of Silicon?," Journal of Microelectromechanical Systems, vol. 19, no. 2, pp. 229-238, Apr 2010.

[36] E. J. Boyd and D. Uttamchandani, "Measurement of the Anisotropy of Young's Modulus in Single-Crystal Silicon," Journal of Microelectromechanical Systems, vol. 21, no. 1, pp. 243-249, Feb 2012.

[37] K. E. Petersen, "Silicon as a mechanical material," IEEE proceedings, vol. 70, no. 5, pp. 420-457, 1982.

[38] Fraunhofer IPMS. "MEMS scanners." Online: https://www.ipms.fraunhofer.de/en/research-development/mems-scanners.html.

[39] D. C. Miller, B. L. Boyce, M. T. Dugger, T. E. Buchheit, and K. Gall, "Characteristics of a commercially available silicon-on-insulator MEMS material," Sensors and Actuators a-Physical, vol. 138, no. 1, pp. 130-144, Jul 2007.

[40] Memscap Inc. "SOIMUMPs design handbook," Online: http://www.memscap.com/products/mumps/soimumps.

[41] A. Crunteanu et al., "Deformable micro-electro-mechanical mirror integration in a fibre laser Q-switch system," Journal of Optics a-Pure and Applied Optics, Proceedings Paper vol. 8, no. 7, pp. S347-S351, Jul 2006.

[42] Texas Instruments, "Introduction to ±12° Orthogonal Digital Micromirror Devices (DMD's)," Online: http://www.ti.com/lit/an/dlpa008b/dlpa008b.pdf.

[43] R. Bauer, L. Li, and D. Uttamchandani, "Dynamic Properties of Angular Vertical Comb-Drive Scanning Micromirrors With Electrothermally Controlled Variable Offset," Journal of Microelectromechanical Systems, vol. 23, no. 4, pp. 999-1008, Aug 2014.

[44] S. Hsu, T. Klose, C. Drabe, and H. Schenk, "Fabrication and characterization of a dynamically flat high resolution micro-scanner," Journal of Optics a-Pure and Applied Optics, Proceedings Paper vol. 10, no. 4, p. 8, Apr 2008.

[45] E. Gallagher, W. Moussa, and M. McDermott, "A review of fabrication processes for vertical comb drives," Microsystem Technologies-Micro-and Nanosystems-Information Storage and Processing Systems, vol. 18, no. 4, pp. 381-397, Apr 2012.

[46] Hamamatsu, "MEMS mirror." Online: http://www.hamamatsu.com/jp/en/4017.html.

[47] B. Wagner, M. Kreutzer, and W. Benecke, "Electromagnetic microactuators with multiple degrees of freedom," 1991 International Conference on Solid-State Sensors and Actuators, San Francisco, USA, 1991.

[48] W. C. Tang, T. C. H. Nguyen, and R. T. Howe, "Laterally driven polysilicon resonant microstructures," Sensors and Actuators, vol. 20, no. 1-2, pp. 25-32, Nov 1989.

[49] L. Li, M. Begbie, G. Brown, and D. Uttamchandani, "Design, simulation and characterization of a MEMS optical scanner," Journal of Micromechanics and Microengineering, vol. 17, no. 9, pp. 1781-1787, Sep 2007.

[50] Q. A. Huang and N. K. S. Lee, "Analytical modeling and optimization for a laterally-driven polysilicon thermal actuator," Microsystem Technologies, vol. 5, no. 3, pp. 133-137, Feb 1999.

[51] A. Jain, A. Kopa, Y. T. Pan, G. K. Fedder, and H. K. Xie, "A two-axis electrothermal micromirror for endoscopic optical coherence tomography," IEEE Journal of Selected Topics in Quantum Electronics, vol. 10, no. 3, pp. 636-642, May-Jun 2004.

[52] L. Li, V. Stankovic, L. Stankovic, L. J. Li, S. Cheng, and D. Uttamchandani, "Single pixel optical imaging using a scanning MEMS mirror," Journal of Micromechanics and Microengineering, vol. 21, no. 2, p. 9, Feb 2011.

[53] J. J. Sun et al., "3D In Vivo optical coherence tomography based on a low-voltage, large-scan-range 2D MEMS mirror," Optics Express, vol. 18, no. 12, pp. 12065-12075, Jun 2010.

[54] L. Wu and H. K. Xie, "124° rotation angle electrothermal micromirror with integrated platinum heater," IEEE Journal of Selected Topics in Quantum Electronics, vol. 13, no. 2, pp. 316-321, Mar-Apr 2007.

[55] L. Li, R. Li, W. Lubeigt, and D. Uttamchandani, "Design, Simulation, and Characterization of a Bimorph Varifocal Micromirror and Its Application in an Optical Imaging System," Journal of Microelectromechanical Systems, vol. 22, no. 2, pp. 285-294, Apr 2013.

[56] Y. Hishinuma, Y. Li, J. Birkmeyer, T. Fujii, T. Naono, and T. Arakawa, "High Performance Sputtered PZT Film for MEMS Applications," Nanotechnology 2012, Vol 2: Electronics, Devices, Fabrication, Mems, Fluidics and Computational, Proceedings Paper pp. 137-140, 2012.

[57] P. Muralt, "Piezoelectric thin films for MEMS," Integrated Ferroelectrics, Proceedings Paper vol. 17, no. 1-4, pp. 297-307, 1997.

[58] M. Tani, M. Akamatsu, Y. Yasuda, H. Fujita, and H. Toshiyoshi, "A Combination of Fast Resonant Mode and Slow Static Deflection of SOI-PZT

Actuators for MEMS Image Projection Display," IEEE/LEOS International Conference on Optical MEMS and Their Applications Conference, Big Sky, USA, 2006.

[59] Y. A. Peter, H. P. Herzig, E. Rochat, R. Dandliker, C. Marxer, and N. F. de Rooij, "Pulsed fiber laser using micro-electro-mechanical mirrors," Optical Engineering, vol. 38, no. 4, pp. 636-640, Apr 1999.

[60] D. Bouyge, A. Crunteanu, V. Couderc, D. Sabourdy, and P. Blondy, "Synchronized tunable Q-switched fiber lasers using deformable achromatic microelectromechanical mirror," IEEE Photonics Technology Letters, vol. 20, no. 9-12, pp. 991-993, May-Jun 2008.

[61] W. Shin et al., "Tunable Q-switched erbium-doped fiber laser based on digital micro-mirror array," Optics Express, vol. 14, no. 12, pp. 5356-5364, Jun 2006.

[62] M. Fabert et al., "8 ns pulses from a compact fibre laser Q-switched by MOEMS," Conference on Lasers and Electro-Optics and Conference on Quantum Electronics and Laser Science, Baltimore, USA, 2009, pp. 25-26.

[63] M. Fabert, A. Desfarges-Berthelemot, V. Kermene, and A. Crunteanu, "Temporal synchronization and spectral combining of pulses from fiber lasers Q-switched by independent MEMS micro-mirrors," Optics Express, vol. 20, no. 20, pp. 22895-22901, Sep 2012.

[64] V. Couderc et al., "Picosecond pulse generation in a hybrid Q-switched laser source by using a microelectromechanical mirror," Optics Express, vol. 20, no. 5, pp. 5524-5529, Feb 2012.

[65] R. Bauer, "Applications of Programmable MEMS Micromirrors in Laser Systems," PhD, Centre for Microsystems and Photonics, University of Strathclyde, 2013.

[66] R. Bauer, W. Lubeigt, and D. Uttamchandani, "Dual Q-switched laser outputs from a single lasing medium using an intracavity MEMS micromirror array," Optics Letters, vol. 37, no. 17, pp. 3567-3569, Sep 2012.

[67] V. Milanovic et al., "Compact MEMS Mirror Based Q-Switch Module for Pulse-on-demand Laser Range Finders," SPIE Conference on MOEMS and Miniaturized Systems XIV, vol. 9375, San Francisco, USA, 2015.

[68] E. C. Vail, G. S. Li, W. P. Yuen, and C. J. ChangHasnain, "High performance and novel effects of micromechanical tunable vertical-cavity lasers," IEEE Journal of Selected Topics in Quantum Electronics, Proceedings Paper vol. 3, no. 2, pp. 691-697, Apr 1997.

[69] M. Y. Li, W. Yuen, G. S. Li, and C. J. Chang-Hasnain, "Top-emitting micromechanical VCSEL with a 31.6-nm tuning range," IEEE Photonics Technology Letters, vol. 10, no. 1, pp. 18-20, Jan 1998.

[70] F. Sugihwo, M. C. Larson, and J. S. Harris, "Micromachined widely tunable vertical cavity laser diodes," Journal of Microelectromechanical Systems, vol. 7, no. 1, pp. 48-55, Mar 1998.

[71] V. Jayaraman, G. D. Cole, M. Robertson, A. Uddin, and A. Cable, "High-sweep-rate 1310 nm MEMS-VCSEL with 150 nm continuous tuning range," Electronics Letters, vol. 48, no. 14, pp. 867-868, Jul 2012.

[72] T. Ansbaek, I. S. Chung, E. S. Semenova, O. Hansen, and K. Yvind, "Resonant MEMS Tunable VCSEL," IEEE Journal of Selected Topics in Quantum Electronics, vol. 19, no. 4, p. 6, Jul-Aug 2013.

[73] D. Vakhshoori et al., "2mW CW singlemode operation of a tunable 1550 nm vertical cavity surface emitting laser with 50 nm tuning range," Electronics Letters, vol. 35, no. 11, pp. 900-901, May 1999.

[74] M. Nakahama, H. Sano, N. Nakata, A. Matsutani, and F. Koyama, "Electro-thermal tuning of MEMS VCSEL with giant wavelength-temperature dependence," IEICE Electronics Express, vol. 9, no. 5, pp. 416-421, Mar 2012.

[75] M. C. Y. Huang, Y. Zhou, and C. J. Chang-Hasnain, "A nanoelectromechanical tunable laser," Nature Photonics, vol. 2, no. 3, pp. 180-184, Mar 2008.

[76] Y. Uenishi, M. Tsugai, and M. Mehregany, "Hybrid-integrated laser-diode micro-external mirror fabricated by (110) silicon micromachining," Electronics Letters, vol. 31, no. 12, pp. 965-966, Jun 1995.

[77] Y. Uenishi, K. Honma, and S. Nagaoka, "Tunable laser diode using a nickel micromachined external mirror," Electronics Letters, vol. 32, no. 13, pp. 1207-1208, Jun 1996.

[78] A. Q. Liu, X. M. Zhang, V. M. Murukeshan, and Y. L. Lam, "A novel integrated micromachined tunable laser using polysilicon 3-D mirror," IEEE Photonics Technology Letters, vol. 13, no. 5, pp. 427-429, May 2001.

[79] X. M. Zhang, H. Cai, C. Lu, C. K. Chen, A. Q. Liu, "Design and experiment of 3-dimensional micro-optical system for MEMS tunable lasers," 19th IEEE International Conference on Micro Electro Mechanical Systems (MEMS 2006), Istanbul, Turkey, 2006, pp. 830-833.

[80] J. Aikio and P. Karioja, "Wavelength tuning of a laser diode by using a micromechanical Fabry-Perot interferometer," IEEE Photonics Technology Letters, vol. 11, no. 10, pp. 1220-1222, Oct 1999.

[81] V. Heikkinen et al., "Single-mode tuning of a 1540-nm diode laser using a Fabry-Perot interferometer," IEEE Photonics Technology Letters, vol. 16, no. 4, pp. 1164-1166, Apr 2004.

[82] A. Lohmann and R. R. A. Syms, "External cavity laser with a vertically etched silicon blazed grating," IEEE Photonics Technology Letters, vol. 15, no. 1, pp. 120-122, Jan 2003.

[83] R. R. A. Syms and A. Lohmann, "MOEMS tuning element for a Littrow external cavity laser," Journal of Microelectromechanical Systems, Proceedings Paper vol. 12, no. 6, pp. 921-928, Dec 2003.

[84] W. Huang, R. R. A. Syms, J. Stagg, and A. Lohmann, "Precision MEMS flexure mount for a Littman tunable external cavity laser," IEEE Proceedings-Science Measurement and Technology, vol. 151, no. 2, pp. 67-75, Mar 2004.

[85] R. R. Asyms, A. Lohmann, and W. Huang, "Extended range tuning elements for a microelectromechanical systems external cavity laser," Journal of Optics a-Pure and Applied Optics, Proceedings Paper vol. 8, no. 7, pp. S299-S304, Jul 2006.

[86] X. M. Zhang et al., "MEMS Littman tunable laser using curve-shaped blazed grating," Transducers '05, Digest of Technical Papers, Vols 1 and 2, Proceedings Paper pp. 804-807, 2005.

[87] B. Pezeshki et al., "20-mW widely tunable laser module using DFB array and MEMS selection," IEEE Photonics Technology Letters, vol. 14, no. 10, pp. 1457-1459, Oct 2002.

[88] J. Masson, R. St-Gelais, A. Poulin, and Y. A. Peter, "Tunable Fiber Laser Using a MEMS-Based in Plane Fabry-Perot Filter," IEEE Journal of Quantum Electronics, vol. 46, no. 9, pp. 1313-1319, Sep 2010.

[89] M. T. Haidar et al., "SOA-Based Tunable Fiber Ring Laser With Intracavity MEMS-Tunable Fabry-Perot Filter," Conference on Lasers and Electro-Optics, San Jose, USA, Jun 2016.

[90] D. Michel, F. Xiao, and K. Alameh, "MEMS-Based Tunable Linear-Cavity Fiber Laser," IEEE Photonics Journal, vol. 4, no. 3, pp. 895-902, Jun 2012.

[91] W. Lubeigt, G. Valentine, J. Girkin, E. Bente, and D. Burns, "Active transverse mode control and optimisation of an all-solid-state laser using an intracavity adaptive-optic mirror," Optics Express, vol. 10, no. 13, pp. 550-555, Jul 2002.

[92] W. Lubeigt, G. Valentine, and D. Burns, "Enhancement of laser performance using an intracavity deformable membrane mirror," Optics Express, vol. 16, no. 15, pp. 10943-10955, Jul 2008.

[93] A. Paterson, R. Bauer, C. Clark, D. Uttamchandani, W. Lubeigt, "Intracavity control of solid-state lasers using MEMS micromirrors," International Conference on Optical MEMS and Nanophotonics (OMN), Glasgow, UK, Aug 2014, pp. 219-220.

[94] P. W. Chapman, O. N. Tufte, J. D. Zook, and D. Long, "Electrical properties of heavily doped silicon," Journal of Applied Physics, vol. 34, no. 11, pp. 3291-3295, 1963.

[95] L. J. Li and D. Uttamchandani, "Dynamic response modelling and characterization of a vertical electrothermal actuator," Journal of Micromechanics and Microengineering, Proceedings Paper vol. 19, no. 7, p. 9, Jul 2009.

[96] P. J. Timans, "Emissivity of silicon at elevated temperatures," Journal of Applied Physics, vol. 74, no. 10, pp. 6353-6364, Nov 1993.

[97] Y. Okada and Y. Tokumaru, "Precise determination of lattice-parameter and thermal expansion coefficient of silicon between 300K and 1500K," Journal of Applied Physics, vol. 56, no. 2, pp. 314-320, 1984.

[98] G. G. Stoney, "The tension of metallic films deposited by electrolysis," Proceedings of the Royal Society of London Series a-Containing Papers of a Mathematical and Physical Character, vol. 82, no. 553, pp. 172-175, May 1909.

[99] Schott. "Optical glass data sheets." Online: https://refractiveindex.info/?shelf=glass&book=SF11&page=SCHOTT.

[100] A. A. Lagatsky, N. V. Kuleshov, and V. P. Mikhailov, "Diode-pumped CW lasing of Yb : KYW and Yb : KGW," Optics Communications, vol. 165, no. 1-3, pp. 71-75, Jul 1999.

[101] A. Saha, A. Ray, S. Mukhopadhyay, P. K. Datta, P. K. Dutta, and S. M. Saltiel, "Littrow-type discretely tunable, Q-switched Nd : YAG laser around 1.3 μm," Applied Physics B-Lasers and Optics, vol. 87, no. 3, pp. 431-436, May 2007.

[102] O. Panahi, M. Nazeri, and S. H. Tavassoli, "Design and construction of a tunable pulsed Ti:sapphire laser," Journal of Theoretical and Applied Physics, vol. 9, no. 2, pp. 99-103, Jun 2015.

Appendix A

The following images were taken using a thermal imaging camera and include the ET mirror as it was actuated at different DC voltages. The colour scales are in degrees Celsius.

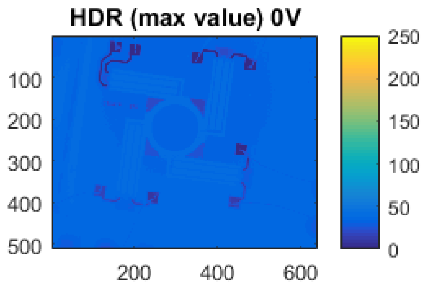

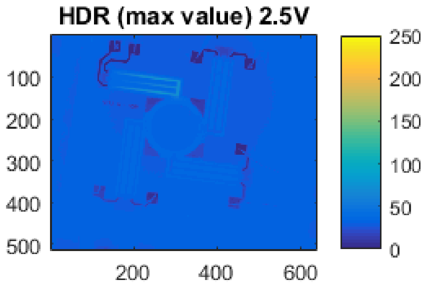

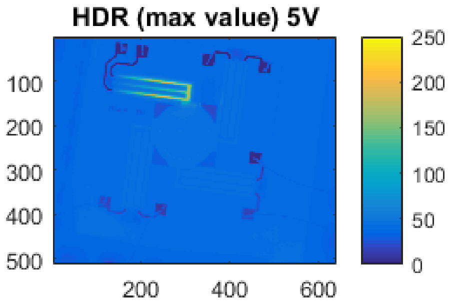

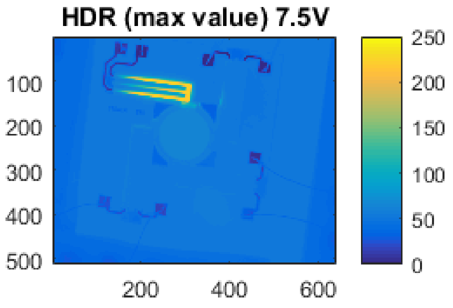

Appendix B

The following code was used for the geometrical optics model reported in Chapter 4. The input parameters can be modified to achieve the results for a specific laser configuration.

```
function [  ] = Model_with_curved_mirror_CoT_change(  )
% --- Geometrical optics model --- %
% Model predicts the output wavelength of the Yb: KGW laser %

lambda0 = 1.0288;    % centre wavelength in um
lambdaU = 1.0388;    % upper wavelength boundary in um
lambdaL = 1.0168;    % lower wavelength boundary in um
lambdaI = 0.001;    % wavelength index step
Lp = 20;            % prism length in mm
Ap = 60;            % prism apex in degrees
Dmems = 180;        % distance between prism and mirror in mm
ROC = 40;           % ROC of mirror
Diameter = 1.4;     % Diameter of mirror

% --- Step 1: find the minimum angle of deviation at lambda0 --- %

A = 1.73759695./(1-0.013188707./lambda0.^2);
B = 0.313747346./(1-0.0623068142./lambda0.^2);
C = 1.89878101./(1-155.23629./lambda0.^2);
n=sqrt(1+A+B+C);    % Sellmeier equation for SF11

Start = 0;     % Starting angle of incidence
End = 70;      % End angle of incidence
Step = 0.0001;  % Step index
D = 360;       % Initialize variable D
i=0;           % Initialize variable i
Counter=1;     % Initialize counter
Critical = asind(1/n);  % Calculate the critical angle


for i1=Start:Step:End

    r1 = asind(1/n*sind(i1));   % angle of refraction at prism entry
    i2 = Ap - r1;               % angle of incidence at prism exit
    r2 = asind(n*sind(i2));     % angle of refraction at prism exit
    Dnew = r2 + i1 - Ap;        % angle of deviation
    if (Dnew < D) && (i1 >= Critical)
        D = Dnew;               % store minimum angle of deviation
        i = i1;                 % store corresponding angle of incidence
    end
    Counter = Counter + 1;      % increment counter
```

```
end

% --- Step 2: Calculate the beam angles through the prism --- %

r1 = asind(1/n*sind(i));       % angle of refraction at prism entry
i2 = Ap - r1;                  % angle of incidence at prism exit
r2 = asind(n*sind(i2));        % angle of refraction at prism exit

% --- Step 3: Map the prism boundaries --- %

Ax = 0 - Lp/2*cosd(90-i);   % x-coordinate of corner A
Ay = Lp/2*sind(90-i);       % y-coordinate of corner A
Bx = Lp/2*cosd(90-i);       % x-coordinate of corner B
By = 0 - Lp/2*sind(90-i);   % y-coordinate of corner B
Cx = Bx+Lp*cosd(90+i-Ap);   % x-coordinate of corner C
Cy = By+Lp*sind(90+i-Ap);   % y-coordinate of corner C

BoundaryABx = [Ax Bx];      % Face AB x-vector
BoundaryABy = [Ay By];      % Face AB y-vector
BoundaryBCx = [Bx Cx];      % Face BC x-vector
BoundaryBCy = [By Cy];      % Face BC y-vector

BoundaryAB = polyfit(BoundaryABx,BoundaryABy,1);    % y=mx+c
BoundaryBC = polyfit(BoundaryBCx,BoundaryBCy,1);    % y=mx+c

% --- Step 4: Map the beam through the prism --- %

Ax = 0 - 100;          % x-coordinate of beam start
Ay = 0;                % y-coordinate of beam start
Bx = 0;                % x-coordinate of prism entry
By = 0;                % y-coordinate of prism entry
BeamABx = [Ax Bx];     % beam entry x-vector
BeamABy = [Ay By];     % beam entry y-vector

trajx = [Bx (Bx + 100*cosd(i-r1))];     % x-trajectory through prism
trajy = [By (By + 100*sind(i-r1))];     % y-trajectory through prism
beam = polyfit(trajx,trajy,1);          % y=mx+c of trajectory

Cx = fzero(@(x) polyval(beam-BoundaryBC,x),3);  % x-intersection
Cy = polyval(beam,Cx);                          % y-intersection
BeamBCx = [Bx Cx];                              % x-vector beam in prism
BeamBCy = [By Cy];                              % y-vector beam in prism

Dx = Cx + Dmems*cosd(D);    % x-coordinate where beam strikes mirror
Dy = Cy + Dmems*sind(D);    % y-coordinate where beam strikes mirror
BeamCDx = [Cx Dx];          % x-vector beam towards mirror
BeamCDy = [Cy Dy];          % y-vector beam towards mirror
beam = polyfit(BeamCDx,BeamCDy,1);

x0 = Dx;                    % Centre of mirror at 0 tilt
```

```
y0 = Dy;                          % Centre of mirror at 0 tilt
omega = 2*asind(Diameter/2/ROC);    % Circle segment of ET mirror
circx = x0 - ROC*cosd(D);
circy = y0 - ROC*sind(D);
A1x = circx + ROC*cosd(D+omega/2);    % Centre of tilt for A2
A1y = circy + ROC*sind(D+omega/2);    % Centre of tilt for A2
A2x = circx + ROC*cosd(D-omega/2);    % Centre of tilt for A1
A2y = circy + ROC*sind(D-omega/2);    % Centre of tilt for A1

Counter = 1;
Table = zeros(round((lambdaU-lambdaL)/lambdaI+1),2);

for wavelength = lambdaL:lambdaI:lambdaU

   A = 1.73759695./(1-0.013188707./wavelength.^2);
   B = 0.313747346./(1-0.0623068142./wavelength.^2);
   C = 1.89878101./(1-155.23629./wavelength.^2);
   n=sqrt(1+A+B+C);              % Sellmeier equation for SF11

   r1 = asind(1/n*sind(i));        % angle of refraction at prism entry
   i2 = Ap - r1;                 % angle of incidence at prism exit
   r2 = asind(n*sind(i2));         % angle of refraction at prism exit
   Dnew = r2 + i - Ap;

   Ax = 0 - 100;          % x-coordinate of beam start
   Ay = 0;                % y-coordinate of beam start
   Bx = 0;                % x-coordinate of prism entry
   By = 0;                % y-coordinate of prism entry
   BeamABx = [Ax Bx];      % beam entry x-vector
   BeamABy = [Ay By];      % beam entry y-vector

   trajx = [Bx (Bx + 100*cosd(i-r1))];     % x-trajectory through prism
   trajy = [By (By + 100*sind(i-r1))];     % y-trajectory through prism
   beam = polyfit(trajx,trajy,1);          % y=mx+c of trajectory

   Cx = fzero(@(x) polyval(beam-BoundaryBC,x),3);  % x-intersection
   Cy = polyval(beam,Cx);                          % y-intersection
   BeamBCx = [Bx Cx];                              % x-vector beam in prism
   BeamBCy = [By Cy];                              % y-vector beam in prism

   trajx = [Cx (Cx + 300*cosd(Dnew))];
   trajy = [Cy (Cy + 300*sind(Dnew))];
   beam = polyfit(trajx,trajy,1);

   Start = -0.5;                  % Start tilt
   End = 0.5;                     % End tilt
   Interval = 0.001;                % Tilt interval
   anglechange = 360;                % Initalize angle change
   Table(Counter,1) = wavelength;     % Declare table

   for tilt = Start:Interval:End
```

```
        % --- Step 5: Map the mirror surface --- %
        % --- positive tilt = clockwise (A2) --- %
        % --- negative tilt = anticlockwise (A1) --- %

        if(tilt<=0)
            circx = A2x - ROC*cosd(D-omega/2+abs(tilt));
            circy = A2y - ROC*sind(D-omega/2+abs(tilt));
        end
        if(tilt>0)
            circx = A1x - ROC*cosd(D+omega/2-abs(tilt));
            circy = A1y - ROC*sind(D+omega/2-abs(tilt));
        end

        y_intersect = beam(2);              % y-intersect of beam
        gradient = tand(Dnew);                  % gradient of beam

        [xm ym] = linecirc(gradient,y_intersect,circx,circy,ROC);
        thetaN = atand((ym(1)-circy)/(xm(1)-circx));
        thetaR = 2*thetaN - Dnew;
        anglechangenew = Dnew - thetaR;

        if (abs(anglechangenew) < abs(anglechange))

            result = tilt;                  % store result
            anglechange = anglechangenew;   % store angle change

        end

    end

    Table(Counter,2) = result;          % update the result table
    Counter = Counter + 1;              % increment counter

end

Table

end
```